UNIVERSITAT DE BARCELONA

Domain walls, primordial black holes and inflation

Albert Sanglás Martín

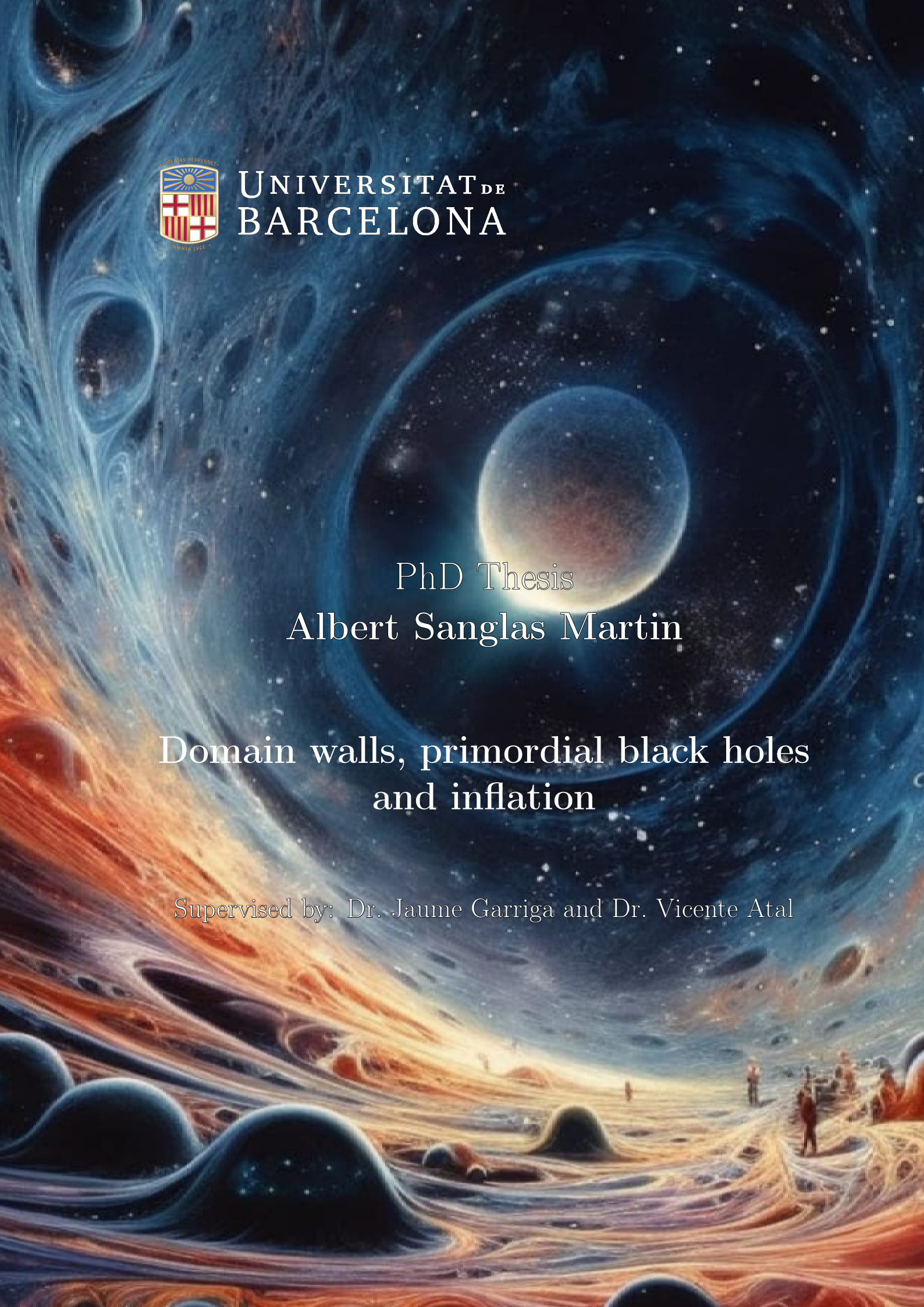

UNIVERSITAT DE BARCELONA

PhD Thesis

Albert Sanglas Martin

Domain walls, primordial black holes and inflation

Supervised by: Dr. Jaume Garriga and Dr. Vicente Atal

UNIVERSITAT DE BARCELONA

Programa de doctorat en Física

Tesi de doctorat

Albert Sanglas Martin

Domain walls, primordial black holes and inflation

Supervisat per: Dr. Jaume Garriga i Dr. Vicente Atal

Tutor: Dr. Joan Soto Riera

Dedicat a la iaia...

Abstract

This thesis investigates primordial black holes and their observational consequences. First, we examine the behavior of domain walls produced during inflation, and their subsequent collapse, leading to the formation of PBHs. The repulsive gravitational field of large spherical domain walls drives gravitational collapse with an unusual spacetime structure, which leads to the formation of a baby universe connected to the parent universe by a wormhole. In this cosmological setup we study the energy-momentum tensor of a quantum field to elucidate the behaviour of Hawking radiation in this peculiar geometry. We find that the energy density, pressure and fluxes proceed smoothly and without pathologies thoughout the entire evolution. In the second part of the thesis, we examine the observational consequences of primordial black holes produced by generic mechanisms, such as large curvature perturbations. More precisely, we investigate the merger rate of binaries and its impact on the stochastic gravitational wave background. Using a phenomenological model, we constrain the merger rate to redshifts around $z \sim 4$ based on data from the LIGO/Virgo-O3 run. We discover distinctive features in the gravitational wave signal at intermediate frequencies for steep merger rates. Our findings have implications for future experiments such as the Einstein Telescope, LISA, and PTA, covering a wide frequency range. Additionally, we highlight the importance of direct observations of the merger rate to break degeneracies in the stochastic background, and provide constraints on the abundance of primordial black holes.

Resum

En aquesta tesi investigem els forats negres primordials les seves conseqüències observacionals. Primerament, examinem el comportament de parets de domini produides durant inflació i el seu subseqüent col·lapse, que condueix a la formació de forats negres primordials. El camp gravitatori repulsiu de parets de domini esfèriques grans, porta a una forma de col·lapse gravitatori amb una estructura d'espai-temps inusual, que condueix a la formació d'un univers nadó connectat a l'univers matern mitjançant un forat de cuc. En aquest escenari cosmològic, estudiem el tensor d'energia-moment d'un camp quàntic per aclarir el comportament de la radiació de Hawking en aquesta geometria peculiar. Trobem que la densitat d'energia, pressió i fluxos es comporten de manera suau i sense patologies durant tota l'evolució. En la segona part de la tesi, estudiem les conseqüències observacionals de forats negres primoridals produits per mecanismes genèrics, com perturbations de curvatura. En concret, investiguem el ritme de fusió de binàries i el seu impacte en el fons estocàstic d'ones gravitacionals. Utilitzant un model fenomenològic, restringim l'exponent en el ritme de fusió fins a redshifts d'aproximadament $z \sim 4$ basant-nos en dades de l'observació LIGO/Virgo-O3. Descobrim característiques distintives en el senyal d'ones gravitacionals a freqüències intermèdies per a ritmes de fusió amb elevat pendent en funció del redshit. Els resultats obtinguts tenen implicacions per a futurs experiments com el Einstein Telescope, LISA i PTA, que cobreixen un ampli rang de freqüències. A més, destaquem la importància de les observacions directes del ritme de fusió per a trencar degeneracions en el fons estocàstic i proporcionar restriccions sobre l'abundància de forats negres primordials.

Acknowledgments

There are not enough words to thank all people who has supported me to finally get to write this page. But I will try.

Firstly, I am deeply grateful to my supervisors, Jaume Garriga and Vicente Atal. It has been an absolute pleasure working with them throughout these years. They have not only imparted their extensive knowledge and provided invaluable guidance for the development of this thesis, but they have also played a significant role in shaping my growth as a physicist. This thesis would not have been possible without Nikos, with whom I shared this path and grew up together in this academic world.

I would also like to express my gratitude to Jose Juan Blanco Pillado and Tomás Andrade for their valuable collaborations and insightful discussions. A special thanks goes to Federico Mescia for imparting upon me the art of teaching. I cannot forget either about the people within the research. The interactions with my fellow PhD students and postdoctoral researchers have proven to be invaluable. I am immensely grateful to Alan for his friendship and support, which remained steadfast until the very last moment. Also, I would like to express my gratitude to rest of the members in office 4.10, Javi and Jairo, for making the days more bearable and enjoyable.

These years wouldn't have been the same without the friendship of Axel, President, and Fali, who even from a distance, has been always here. This acknowledgments page would not be completed without mention my dear friend Samantha (who by the way, "crafted" the amazing cover image for this manuscript). I wouldn't have made it this far without the moments of disconnection that music has provided me, together with Alba, Juani, Padilla, Joan, Arnau, David, Albert i Nito. Last but certainly not least, I want to acknowledge the incredible people from the BrainLab. Their simple presence in the final months have been invaluable, making this journey all the more meaningful.

Lastly, I would like to thank my family. Without them I would not be the person I am now. To 'la mama', who has always patiently listened to me talking about black holes, multiverses, and domain walls, even without understanding a word. To "el papa," who has consistently motivated me to persevere, even in moments of doubt and confusion. To Abril and Max, just for simply being by my side and making life full of happiness. To Mireia, without whose advice I would not have ventured into this journey. And finally, to "l'àvia", to whom now I can say "I finally did it".

Preface

This thesis compiles the main results during my PhD studies conducted between 2018 and 2023 at the Gravity and Strings group of the Universitat de Barcelona, under the supervision of Dr. Jaume Garriga and Dr. Vicente Atal, and supported by an APIF grant from Universitat de Barcelona. This thesis is based on the following papers:

- **"Constraining changes in the merger history of (P)BH binaries with the stochastic gravitational wave background"** [1]
- **"NANOGrav signal as mergers of Stupendously Large Primordial Black Holes"** [2]
- **"LIGO/Virgo black holes and dark matter: The effect of spatial clustering"** [3]
- **"Evaporation of a supercritical primordial black hole"** [4]

Contents

Introduction

The mysterious nature of dark matter, the origins of supermassive black holes, and the occurrence of black hole merger events have recently captivated the attention of the scientific community. Primordial black holes (PBHs) have emerged as compelling candidates that could potentially address these enigmatic phenomena. They have been proposed as a fraction or even the entirety of dark matter [5–9], as potential seeds for the supermassive black holes at the centers of galaxies, or as contributors to observed black hole merger events [10–12]. The formation of PBHs can occur through various mechanisms, either as a consequence of significant irregularities following phase transitions or as a result of primordial seeds generated during inflation. This thesis primarily focuses on investigating the production of such primordial black holes and studying their observational consequences.

The thesis is divided into two parts. In part one, we study the possibility of PBH production by active relics such as false vacuum bubbles or domain walls, which persisted from an earlier inflationary epoch [13–15]. In particular, we concentrate on closed and large domain walls as potential seeds of PBHs. Walls may be produced by quantum tunneling with an initial size of the order of the Hubble radius and are subsequently stretched to very large sizes by the inflationary expansion. Such scenarios and their observational consequences have been discussed in Refs. [16–23].

Shortly after inflation, the universe is described by a homogeneous Friedmann-Lemaître-Robertson-Walker (FLRW) background spacetime with small perturbations. Domain walls are characterized by a tension σ generating a repulsive gravitational field that makes them naturally expand at a rate proportional to σ. At early times, $t \ll (G\sigma)^{-1}$, the gravitational influence of the domain wall tension is negligible compared to the surrounding matter. Domain walls that fall within the cosmological horizon during this period experience contraction due to their internal tension, and may either dissipate their energy by producing bosons or persist as metastable remnants if the pressure exerted by matter within their interior can counterbalance the surface tension. The fate of these remnants is inherently model-dependent. Here, we are interested in the fate of *large supercritical* domain walls which are still outside the horizon at $t \sim (G\sigma)^{-1}$. For such walls, the repulsive gravitational field they generate becomes dominant before falling within the horizon. This leads to a peculiar form of gravitational collapse,

where instead of shrinking under its tension, the wall starts inflating within a region that eventually separates from the *parent* universe, thereby giving rise to a *baby* universe. The global spacetime structure associated with the supercritical collapse exhibits a more intricate configuration than in ordinary scenarios. The black hole spacetime incorporates two future event horizons: one facing the parent universe and the other facing the baby universe. This unconventional structure motivates us to assess the semiclassical stability by studying the propagation of a quantum field in this background and computing the expectation value of its energy-momentum tensor.

The structure of part one goes as follows. In Chapter 1 we review some basics of de Sitter spacetime which models the inflationary epoch and the nucleation of domain walls by quantum tunneling. Moreover we discuss the dynamics of such domain walls in de Sitter and Schwarzschild backgrounds. The gravitational collapse of large supercritical domain walls and the construction of the resulting spacetime is explained in detail in Chapter 2. We dedicate Chapter 3 to calculate the stress-energy tensor for a massless scalar field in the resulting spacetime of the domain wall collapse. Finally, in Chapter 4 we describe the observations made by different geodesic observers moving in the spacetime.

The second part of the thesis deals with observational consequences of a population of PBHs produced by generic mechanisms. The direct detection of gravitational waves (GWs) by the LIGO/Virgo collaboration has opened up a new era of gravitational wave astronomy, revolutionizing our understanding of the dynamics and properties of black hole binary mergers. The GWTC-3 catalog of LIGO/Virgo [24, 25] represents a significant milestone in the field, reporting the direct detection of 63 binary black hole (BBH) mergers spanning a wide range of redshifts, from approximately $z \simeq 0.1$ up to $z \simeq 0.8$. These observations have also provided valuable information about the merger rate density of binaries as a function of redshift.

Usually it is assumed that the merger rate density $R(z)$ follows a power law $R(z) = R_0(1+z)^\alpha$, determined by the present merger rate R_0 and the exponent α. The analysis of the LIGO/Virgo data has allowed us to constrain the value of α, with a measurement of $2.7^{+1.8}_{-1.9}$, and estimate the present merger rate within the range of $9 - 35$ Gpc^{-3}yr^{-1} [24, 25]. However, these constraints are limited to the redshift range accessible to the current observations, with the so-called horizon distance defining the maximum redshift at which a certain binary merger could be detected. For BBHs with a typical mass of $\sim 30M_\odot$, the horizon distance is approximately $z_{\rm hor} \simeq 1$ for LIGO/Virgo. This raises an important question: can relevant information about BBH mergers at redshifts larger than $z_{\rm hor}$ be inferred from GW observations? The answer to this question is affirmative.

In addition to the direct detections of individual BBH mergers, GW detectors have the potential to detect a stochastic background of graviational waves (SBGW) generated

by the cumulative effect of past mergers that may not be individually distinguishable. This stochastic background is directly related to the integrated merger rate over cosmic time and could provide valuable insights into the evolution of the merger rate at redshifts beyond the reach of single detections. Despite extensive searches, the stochastic background has not been detected yet. However, this absence of detection has been utilized to constrain the abundance of BBHs and to investigate various models of binary merger rate evolution [26–36]. While previous works have investigated this direction [34, 35], we complemented and extended these results by taking a more phenomenological approach. The goal is to determine more precisely the maximum redshift at which the merger rate can be constrained based on the (non)observations of the stochastic background.

The merger rate history is very highly model dependent. For instance, histories of stellar black holes follow a power law up to some redshift and then they decay. For PBHs evolving from an initial Poissonian distribution, the exponent α of the merger rate, depends on the abundance of PBHs and the range of redshift considered. For small abundances and redshifts below $z < 1$, the exponent is found to be $\alpha = 1.1$, while for large redshifts, the value of α increases to $\alpha = 1.4$. The behaviour of the merger rate history becomes more complex for larger abundances and clustered distributions due to the effects of N-body dynamics and an enlarged set of parameters [3, 32, 37–39]. Given the significant uncertainty in the allowed merger histories, we adopt a phenomenological approach to investigate the consequences of changes in the merger rate slope at specific redshifts.

The goal here is to understand how the non-detection of the stochastic gravitational wave signal by the LIGO/Virgo collaboration can provide constraints on the changes in the merger rate. By analyzing the absence of the stochastic background, we can infer constraints on the changes in the merger rate slope beyond the horizon redshift $z_{\rm hor}$. Furthermore, we explore the potential of future experiments such as the Einstein Telescope (ET), operating in the same frequency band as LIGO/Virgo, as well as experiments at lower frequencies, including LISA and pulsar timing array (PTA) observatories such as NANOGrav and SKA [40–43].

The structure of part two is organized as follows. In Chapter 5, we review the dynamics of the formation of primordial black hole binaries as well as the calculation of their merger rate. We also review the basics on the detection of the SBGW. This serves as an introduction of the machinery used in Chapter 6, where the main result is presented.

Part I

Domain walls and primordial black holes

Chapter

1 Inflation and domain walls

In this chapter, we provide a self-contained review of de Sitter spacetime and domain walls which is needed for understanding the gravitational collapse of domain walls in a post-inflationary epoch. De Sitter spacetime plays a pivotal role in modeling the expanding universe during inflation. In particular, we emphasize the different coordinate systems that will be useful for our discussion in connection with the description of domain wall dynamics.

Next, we introduce domain walls as topological defects that can arise during phase transitions in the early universe. We investigate their nucleation process in de Sitter spacetime and examine their subsequent dynamics. Also, we extend our study to the dynamics of domain walls in a Schwarzschild spacetime since this will be needed later in Chapter 2.

1.1 de Sitter space

De Sitter space (dS) is a solution of Einstein's field equations with a positive cosmological constant. It serves as a valuable theoretical model for the early universe, characterized by a period of cosmic inflation marked by a constant expansion rate H. De Sitter space possesses distinctive geometric properties, including maximal symmetry.

A four-dimensional spacetime, dS can be mathematically described as a hyperboloid with constant curvature H^{-1} embedded in a five-dimensional Euclidean space:

$$X_0^2 + X_1^2 + X_2^2 + X_3^2 + X_4^2 = H^{-2}\,. \tag{1.1}$$

This highlights the inherent symmetry of dS, known as $O(4,1)$. However, alternative parameterizations exist, which we will review in the following subsections. These are essential for our subsequent analysis.

1.1.1 Global coordinates

The first parametrization of the de Sitter space metric can be found by performing the change of variables

$$\begin{aligned} X_0 &= H^{-1}\sinh(HT) \\ X_i &= H^{-1}\cosh(HT)\sin\chi\, n_i\,, \quad i=1,2,3 \\ X_4 &= H^{-1}\cosh(HT)\cos\chi \end{aligned} \tag{1.2}$$

where n_i are unit vectors describing a two-sphere S^2. [1]. Then the metric reads

$$ds^2 = -dT^2 + H^{-2}\cosh^2(HT)\left(d\chi^2 + \sin\chi d\Omega_3^2\right) \tag{1.3}$$

where T runs from $(-\infty,\infty)$ and χ from $(0,\pi)$. Such global coordinates cover the maximal extension of the de Sitter space as can be seen in Figure 1.1. From Eq. (1.3) we see that it can be viewed as a contracting and then expanding three dimensional sphere of radius $H^{-1}\cosh(HT)$. This parametrization allows us to draw a Carter-Penrose diagram for de Sitter space which is shown in the left diagram of Figure 1.1. To do so, we can rewrite Eq. (1.3) using the conformal time $\tilde{\eta}$ given by $\tan(\tilde{\eta}/2) = \tanh(HT/2)$, turning the metric into

$$ds^2 = \frac{H^{-2}}{\cos^2\tilde{\eta}}\left(-d\tilde{\eta}^2 + d\chi^2 + \sin\chi d\Omega_2^2\right) \tag{1.4}$$

where $\tilde{\eta}\in[-\pi/2,\pi/2]$.

1.1.2 Flat coordinates

In cosmology, it is quite common to slice de Sitter spacetime is by using cosmological coordinates. We can find it by performing the change of variables

$$\begin{aligned} X_0 &= H^{-1}\sinh(Ht) + \frac{1}{2}H|\vec{x}|^2 e^{Ht} \\ X_i &= x_i e^{Ht}\,, \quad i=1,2,3 \\ X_4 &= H^{-1}\cosh(Ht) - \frac{1}{2}H|\vec{x}|^2 e^{Ht} \end{aligned} \tag{1.5}$$

[1] The unit vectors on a $D-1$-dimenisonal sphere S^{D-1} are given By

$$\begin{aligned} n_1 &= \cos\theta_1 \\ n_2 &= \sin\theta_1\cos\theta_2 \\ \cdots n_D &= \sin\theta_1\ldots\sin\theta_{D-1} \end{aligned}$$

and the line element is

$$\mathrm{d}\Omega_{D-1}^2 = d\theta_1^2 + \sin^2\theta_1 d\theta_2^2 + \cdots + \sin^2\theta_1\cdots\sin^2\theta_{D-1}d\theta_{D-1}^2$$

which results in the metric

$$ds^2 = -dt^2 + e^{2Ht}\mathrm{d}\vec{x}^2 ds^2 == dt^2 + e^{2Ht}\left(dr^2 + r^2 d\Omega_2^2\right) \tag{1.6}$$

with $r = |\vec{x}|$. This chart includes only one half of the full de Sitter space, with $\tilde{\eta} \geq \chi - \pi/2$ in the global chart (see Figure 1.1).

1.1.3 Domain wall adapted coordinates

Let us now parametrize the hyperboloid coordinates as follows

$$\begin{aligned} X_0 &= H^{-1}\sin(H\rho)\sinh(H\hat{\tau}) \\ X_i &= H^{-1}\sin(H\rho)\cosh(H\hat{\tau})\ n_i\,, \quad i = 1,2,3 \\ X_4 &= H^{-1}\cos(H\rho) \end{aligned} \tag{1.7}$$

with n_i the normal vector components of a two-sphere, and the other coordinate ranges are $-\infty < \hat{\tau} < \infty$, $0 \leq H\rho \leq \pi$. By using these coordinates, the metric can be written as

$$ds^2 = d\rho^2 + \sin^2(H\rho)\left[-d\hat{\tau}^2 + H^{-2}\cosh^2(H\hat{\tau})\, d\Omega_2^2\right] \tag{1.8}$$

The part within the brackets is a three-dimensional de Sitter space in the global representation. This representation is usually called "dS-slicing". Note that by definition, $|X_4| \leq H^{-1}$, so this set of coordinates do not cover all de Sitter space but just a half, in particular the diamond shaped region $0 < \chi \pm \tilde{\eta} < \pi$ in the global chart (see Figure 1.1). It is useful to write it in terms of the spatial coordinate ξ given by $\sin(H\rho) = 1/\cosh(H\xi)$. Then the metric reads

$$ds^2 = \frac{1}{H^2\cosh(H\xi)}\left[d\xi^2 - d\hat{\tau}^2 + H^{-2}\cosh^2(H\hat{\tau})\, d\Omega_2^2\right] \tag{1.9}$$

where $-\infty < \xi < \infty$.

1.2 Domain walls

Domain walls are two-dimensional topological defects that may arise from the spontaneous breaking of a discrete symmetry [44]. Take for instance a scalar field ψ whose potential $\tilde{V}(\psi)$ has a Z_2 symmetry, with two degenerate minima which we shall denote as $+$ and $-$ respectively (see Figure 1.2). This will result in different regions with either a positive or negative vacuum for the field ψ. Moving from a region in the positive vacuum to one with the negative vacuum requires passing through the potential maximum, where a domain wall will be formed, separating both regions.

This field may be part of the inflaton sector, but for simplicity we shall consider the case where ψ and the inflaton field ϕ are completely decoupled from each other,

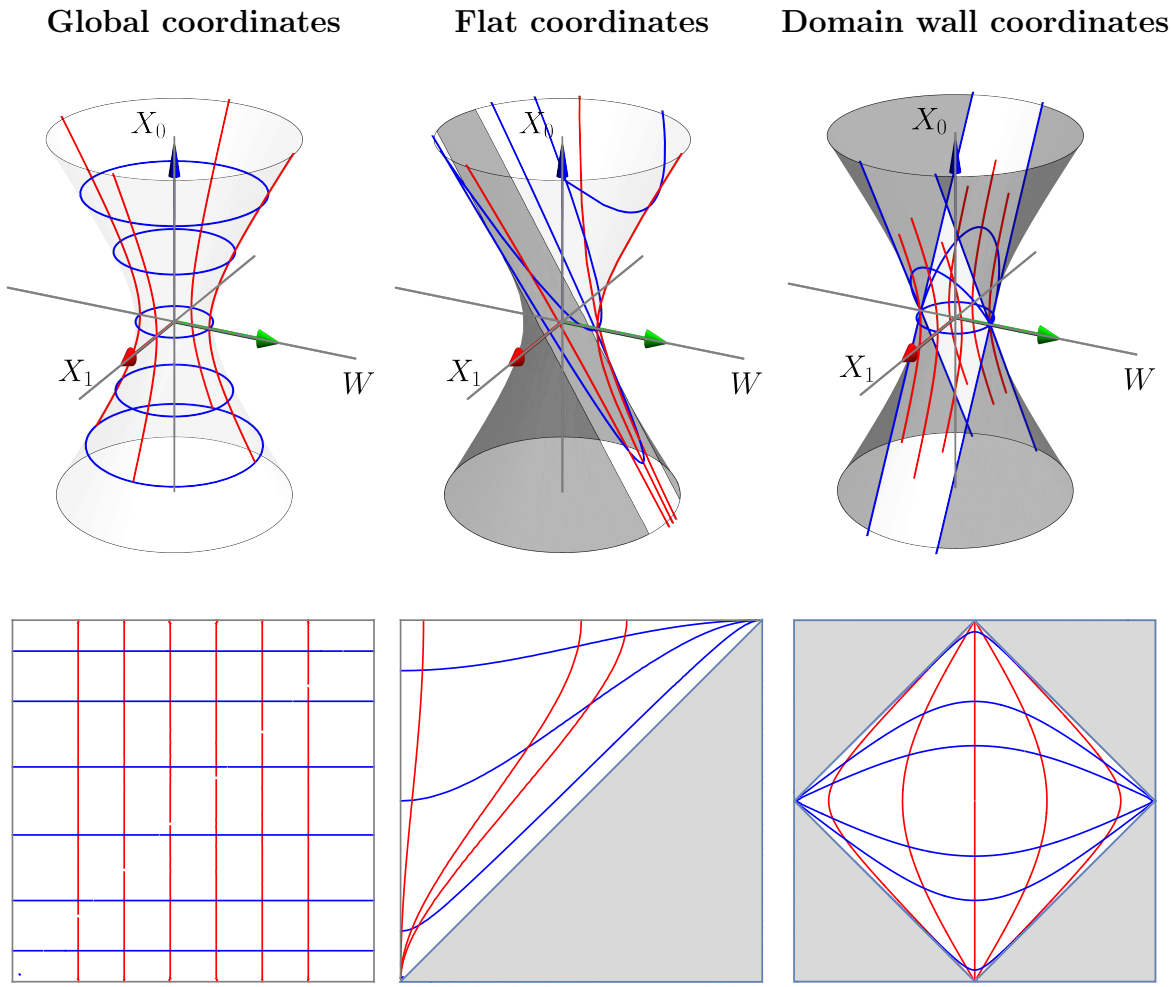

Figure 1.1: Embedding diagrams of de Sitter spacetime in Euclidean space and the corresponding Penrose diagrams. We also show how the global, flat and domain wall adapted coordinate cover the full or part of de Sitter space. Shaded in gray we show the regions that are not cover by the corresponding coordinates. **Left:** Red lines correspond to χ = constant surfaces and blue lines correspond to $\tilde{\eta}$ = constant surfaces for the metric Eq. (1.3). **Center:** Red lines correspond to $|\vec{x}|$ = constant surfaces and blue lines correspond to t = constant surfaces for the metric Eq. (1.6). **Right:** Red lines correspond to ρ = constant surfaces and blue lines correspond to T = constant surfaces for the metric Eq. (1.9).

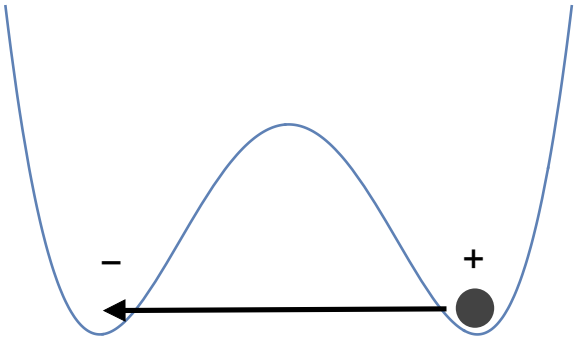

Figure 1.2: Scalar field potential $\tilde{V}(\psi)$ with a discrete symmetry. During inflation, assuming the field is initially in the + vacuum, a Hubble-sized region can transit to the − vacuum by a quantum fluctuation. The region in the − vacuum will be separated from the ambient space in the + vacuum by a domain wall, which is then conformally stretched by expansion.

interacting only gravitationally. As inflation proceeds, the field ψ in a Hubble patch may ocasionally transit from one of the symmetry breaking minima to the other. The transition between vacua can proceed either by quantum diffusion or by tunneling, depending on whether the curvature of the potential between the minima, $|\tilde{V}''|$, is small or large compared to the square of the Hubble rate H^2 [44–47]. Here we concentrate on the case of quantum tunneling, in the regime where this is suppressed by a large instanton action [13, 48]. In this case, the region in the new vacuum is approximately spherical and bounded by a domain wall separating the two phases. Walls are then conformally stretched by expansion.

Domain walls are characterized by a finite surface energy density σ and a tension (negative pressure) with equal magnitude. This negative pressure generates a repulsive gravitational field that makes domain walls naturally expand. When inflation ends, the walls that formed earlier on will be exponentially larger than the ones that formed near the end of inflation. Note that this does not require any specific features in the inflaton potential $V(\phi)$, which can be of the standard slow-roll type, with nearly scale invariant dynamics.

1.3 Domain wall nucleation in a de Sitter spacetime

In this subsection we shall describe the nucleation process of a domain wall in a dS and the resulting spacetime. For simplicity, we assume a situation where, during inflation, the slow roll parameters are so small that we can approximate the metric by that of dS spacetime. A conformal diagram is given in the left panel of Figure 1.3.

We are not in fact interested in the full de Sitter space, but only in an expanding segment of it covered by the flat chart Eq. (1.6). In practice, inflation only lasts from an initial time t_{initial} to a final time, which we will call t_*. Eq. (1.6) represents the spacetime metric before the wall nucleates. The nucleation process can be thought of as a quantum transition from this classical solution, where the field sits in the + valley, to another classical solution where the expanding universe contains a spherical domain wall, enclosing a region of the − vacuum [13]. The quantum transition is described by the so-called Coleman de Lucia (CdL) instanton [48], which is a solution to the Euclidean equations of motion with appropriate boundary conditions. This represents the classically forbidden underbarrier field evolution. Quantum mechanically, the probability of tunneling is proportional to e^{-S_E}, where S_E is the instanton action. This semiclassical approximation is valid for $S_E \gg 1$. The analytic continuation of the instanton to Lorentzian signature corresponds to the classical solution after tunneling. This is given by the right panel of Figure 1.3.

The CdL instanton is $O(4)$ symmetric, and its analytic continuation has the $O(3,1)$ symmetry. Geometrically, the domain wall breaks the homogeneity of de Sitter space. Nonetheless, the field configuration after tunneling still respects a group of rotations and Lorentz boosts that leave the worldsheet of the domain wall invariant. To construct the solution after tunneling, we may use coordinates adapted to the residual symmetry, and write the dS metric as in Eq. (1.9), This chart covers the diamond shaped region in Figure 1.3, with $0 < \chi \pm \tilde{\eta} < \pi$. The $\xi =$ const. hypersurfaces (two of which are represented by dashed lines in the figure) are the orbits of the residual $O(3,1)$ symmetry group, which is in fact the isometry group of the 2+1 dimensional de Sitter subspaces at fixed ξ, spanned by coordinates $(\hat{\tau}, \Omega)$.

Here, and for the rest of this thesis, we treat the domain wall as a distributional source with energy per unit surface equal to the wall tension σ. Away from the wall, the metric is given by Eq. (1.9). However, through Einstein's equations, the wall tension causes a discontinuity in the extrinsic curvature of the worldsheet as seen from both sides, leading to the well know Israel matching conditions, which are discussed in Appendix A. By $O(3,1)$ symmetry, the trajectory of the wall is on a $\xi = \xi_w^{\pm} =$ const. hypersurface, where the values of $\xi_w^{\pm}$ correspond to the position of the wall as seen from the outside or from the inside respectively. These are determined by Eq. (A.5) as

$$\tanh \xi_w^{\pm} = \pm \beta_0, \tag{1.10}$$

where

$$\beta_0 = (1 + H^2 t_\sigma^2)^{-1/2} . \tag{1.11}$$

and

$$t_\sigma \equiv (2\pi G \sigma)^{-1} . \tag{1.12}$$

The point $\tilde{\eta} = \chi = 0$ (corresponding to $\xi \to -\infty$ and finite $\hat{\tau}$) is a fixed point. We label it C in the diagram, and we shall refer to it as the "center of symmetry". [2]

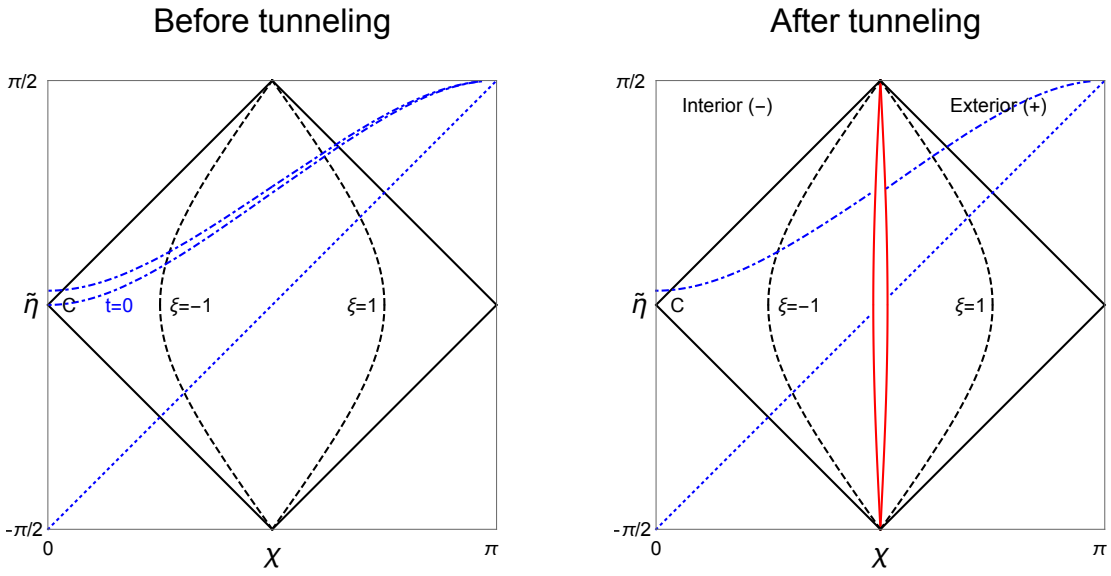

Figure 1.3: The left pannel shows a conformal diagram of de Sitter space in the global chart $(\tilde{\eta}, \chi)$, where the metric is given by Eq. (1.4). Angular coordinates are suppressed. The flat chart (1.6) covers only the region above the dotted blue diagonal, which corresponds to $t \to -\infty$. The dot dashed lines in blue represent two $t = const.$ hypersurfaces in the flat chart. The lower one corresponds to $t = 0$ and the upper one has $t > 0$. The chart Eq. (**??**) is adapted to $O(3,1)$ symmetry, and covers the diamond shaped region at the center of the diagram. Represented in black dashed lines are two hypersurfaces of constant ξ. The analytic continuation of the Euclidean instanton solution, describing the evolution after tunneling, is represented in the right panel. The red lines at $\xi = \pm \tanh^{-1} \beta_0$ represent the trajectory of the domain wall as seen from the exterior and the interior respectively. The two red lines are identified with each other, after excising the region between them. Note that in the (η, χ) diagram, the radius of the spere is $R = H^{-1} \sin\chi / \cos\tilde{\eta}$. The red lines are symmetric relative to $\chi = \pi/2$, and hence the size of the wall is the same when $\tilde{\eta}$ is the same. In other words, points on the two red lines are identified horizontally in the diagram. In particular, this means that the exterior $t = 0$ hypersurface matches with a $t = -H^{-1} \log(1 + 2\beta_0) > 0$ hypersurface in the interior, so that the metric is continuous on the worldsheet of the domain wall.

[2] There is another fixed point at the antipodal point, $\tilde{\eta} = 0, \chi = \pi$, but since this is not included in the flat chart, we will not need to refer to it in what follows .

1.4 Domain wall evolution during inflation in the flat chart

While the chart (1.9) is nicely adapted to the symmetry of wall nucleation, we also need to consider the description of the wall evolution in the flat chart (1.6). The reason is that in the next Chapter we will intend to match the inflationary evolution to a post-inflationary flat FLRW dust dominated universe. Besides, the flat chart description offers a new perspective. In the global chart, the spatial sections are a closed 3-sphere, and there is ambiguity in what we call the interior and the exterior of a domain wall in such compact space. On the other hand, flat spatial sections are infinite, and the notion of interior and exterior is clearly defined.

After the wall nucleates, the line element is still given by Eq. (1.6), although the time and radial coordinates $t^{\pm}$ and $r^{\pm}$ of a point on the worldsheet will be different on either side. For a domain wall spontaneously nucleating in de Sitter space, the evolution of thee physical area radius can be obtained by converting the condition (1.10) into the flat chart [13]

$$R(t) = e^{Ht} r = H^{-1}[e^{2Ht} + 1 \pm 2\beta_0 e^{Ht}]^{1/2}, \tag{1.13}$$

where β_0 was introduced in (1.11).

Although the wall can actually nucleate around any point, here we choose it to be centered at the origin of spatial coordinates $r = 0$. Likewise, (1.13) corresponds to the case when the center of symmetry C of the solution, which we can roughly think of as the nucleation event, is on the hypersurface $t = 0$. The replacement

$$t \to t - t_{nuc},$$

gives the solution with any arbitrary time of nucleation t_{nuc}. Continuity of the area radius accross the wall requires $R(t^+) = R(t^-)$, which leads to

$$e^{2Ht^+} + 2\beta_0 e^{Ht^+} = e^{2Ht^-} - 2\beta_0 e^{Ht^-}. \tag{1.14}$$

In particular, the exterior hypersurface $t^+ = 0$ matches continuously with the interior hypersurface

$$t^- = -H^{-1} \log(1 + 2\beta_0)\,.$$

Note also that, according to Eq. (1.14), the rate at which times t^+ and t^- advance on both sides of the worldsheet will be different. This is to be expected, because, as we discuss below, the speed at which the cosmological congruence moves relative to the wall is different on both sides, and so the associated clocks tick at different rate.

Note also that the physical area radius R increases monotonically from $R \sim H^{-1}$ at $t \sim H^{-1}$ to an exponentially much larger size, $R \sim H^{-1} e^N$, provided that the number

N of e-foldings of inflation after nucleation is large. Thus, R can be used to parametrize the time evolution on the worldsheet. Let us now determine the relative speed between the wall and co-moving observers in the flat chart, as a function of R. The 4-velocity of a comoving observer is given by $U^\mu = (1,0,0,0)$, while an observer at fixed angular coordinates on the wall has 4-velocity $W^\mu = (1, dr/dt, 0, 0)/\sqrt{1-a^2(dr/dt)^2}$. The mutual relativistic gamma factor is then given by $\gamma \equiv -g_{\mu\nu}U^\mu W^\nu = Hr(1-\beta_0^2)^{-1/2}$, and using $r = R\,(\sqrt{\beta_0^2 + H^2R^2 - 1} \pm \beta_0)^{-1}$ we have

$$\gamma = \frac{1}{1-(HR)^{-2}}\left[\mp(H^2 t_\sigma R)^{-1} + \sqrt{1-(HR)^{-2}+(Ht_\sigma)^{-2}}\right]. \tag{1.15}$$

For $R \gg t_\sigma \gg H^{-1}$ we have $\gamma \approx 1 + (1/2)(Ht_\sigma)^{-2}$, and the relative velocity is small $v \sim (Ht_\sigma)^{-1} \ll 1$. The sign of the wall velocity is given by

$$\mathrm{sign}(dr/dt) = \mathrm{sign}(-e^{-Ht} \mp \beta_0). \tag{1.16}$$

From the outside we always have $dr/dt < 0$, so the wall is shrinking away from co-moving observers. From the inside, the velocity changes from negative to positive at the time $t_c = -H^{-1}\log\beta_0$ when the physical radius of the wall has the value $R(t_c) = t_\sigma$.

1.5 Spherical domain walls in vacuum

In this section we will study the spacetime of a spherical domain wall evolving in vacuum, as it will be important in Chapter 2 on the discussion about the gravitational collapse of supercritical domain walls.

The spacetime is constructed as follows. Since the wall is spherical and it is propagating in vacuum, the solution at each side (which we denote by $+$ and $-$) of the wall must be given by the Schwarschild metric,

$$ds^2 = -\left(1-\frac{R}{2GM}\right)dT^2 + \left(1-\frac{R}{2GM}\right)^{-1}dR^2 + R^2 d\Omega_2^2\,, \tag{1.17}$$

with the same mass parameter M at both sides. The full solution is then constructed by gluing these two patches of Schwarzschild along the domain wall worldsheet, by imposing Israel's matching conditions. Continuity of the angular components of the metric, implies that the proper radius of the wall as a function of the proper time, $R(\tau)$, must be the same as seen from both sides. On the other hand, the wall tension causes a discontinuity in the extrinsic curvature of the worldsheet proportional to t_σ^{-1} (see Appendix B). This implies that the temporal coordinate at both sides must have the same value with opposite sign, $T_+(\tau) = -T_-(\tau)$.

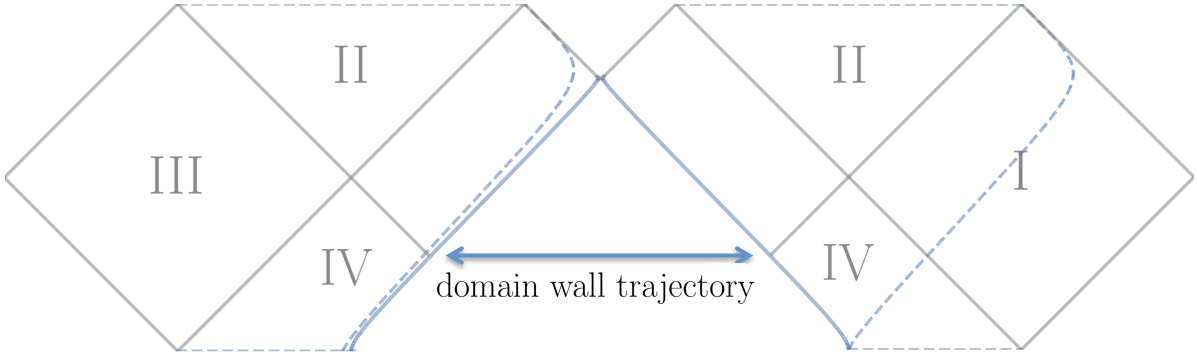

Figure 1.4: The casusal diagram of the spacetime of a spherical domain wall evolving in vacuum. It consists in two patches of Schwarzschild spacetime glued across the domain wall. The domain wall joints the two asymptotically flat regions I and III.

The discontinuity in the extrinsic curvature defines the equations of motion for the domain wall [49]

$$\dot{R}^2 = \frac{2GM}{R} + \left(\frac{R}{t_\sigma}\right)^2 - 1\,, \tag{1.18a}$$

$$\dot{T} = \pm\left(1 - \frac{2GM}{R}\right)^{-1}\frac{R}{t_\sigma} \tag{1.18b}$$

where the dot means derivative with respect to τ. A causal diagram of the resulting spacetime is shown in Figure 1.4. Note that since $T_+(\tau) = -T_-(\tau)$ and $R_+(\tau) = R_-(\tau)$, the motion of the wall as seen from the $+$ side is a mirror image of the motion as seen from the $-$ side. The $\pm$ in Eq. (1.18b) depends on wether the wall moves to the right or to the left of the diagram.

Note that Eq. (1.18a) is analogous to the equation of motion for a non-relativistic particle of zero energy in a static potential

$$W(R) = 1 - \frac{2GM}{R} - \left(\frac{R}{t_\sigma}\right)^2\,, \tag{1.19}$$

This potential has a single maximum at $R_{\max}^3 = GMt_\sigma^2$ and its value is $W(R_{\max}) = 1 - 3\,(GM/t_\sigma)^{2/3}$. This may lead to three possible fates for the domain wall depending on the value of its tension. In the case where $t_\sigma < \sqrt{27}GM$, then the potential will be always negative, thus the radius will expand without any bound towards infinite size. In Ref. [15] these were dubbed *supercritical* domain walls. On the other hand, *subcritical* domain walls are characterized by $t_\sigma > \sqrt{27}GM$. In this case, the maximum of the potential is positive, so at some radius $R < R_{\max}$ - the first real root of the potential -, it will bounce and recollapse at a black hole singularity. Finally,

the *critical* case corresponds to the specific value of $t_\sigma = \sqrt{27}GM$, then the radius of the domain wall gets frozen at a value of $R = 3GM$. In Figure 1.5 we depict the evolution of the radius of domain walls with different values of t_σ. For the rest of the thesis, we will focus only on supercritical domain walls.

We are interested in studying the evolution of the domain wall in all spacetime. Also, in Chapters 2 and 3 we will need to work with light rays, which are better characterized by the use of null coordinates. For this reason we will use Kruskal-Szekeres null coordinates to describe the motion of the wall, since they cover all Schwarzschild spacetime and are regular at the horizon. These are defined in terms of the Schwarzschild coordinates as[3]

$$\begin{aligned} U &\equiv \lambda_U \exp\left(\frac{R-T}{4GM}\right)\sqrt{\left|\frac{R}{2GM}-1\right|} \\ V &\equiv \lambda_V \exp\left(\frac{R+T}{4GM}\right)\sqrt{\left|\frac{R}{2GM}-1\right|} \end{aligned} \tag{1.22}$$

where the factors λ_U and λ_V are just signs that depend on which region of the Schwarzschild spacetime are defined. In Figure 1.4 we see that the maximal extension is divided in four regions: regions I and III correspond to asymptotically flat spaces, region II correspond to the black hole region and regions IV to the "white hole" region. The coordinate U is negative at regions I and IV, and positive at regions II and III, while V is negative at regions III and IV and positive at regions I and II.

For supercritical domain walls, one can combine Eqs. (1.18) into a single differential equation,

$$\frac{dU}{dV} = \frac{U}{V}\left(\frac{1 \mp \theta(R,t_\sigma)}{1 \pm \theta(R,t_\sigma)}\right) , \tag{1.23}$$

where we have defined the function

$$\theta(R,t_\sigma) = \left(\frac{R}{2GM}\right)^{3/2}\left(\left(\frac{R}{2GM}\right)^3 - \frac{Rt_\sigma^2}{(2GM)^3} + \left(\frac{t_\sigma}{2GM}\right)^2\right)^{-1/2} . \tag{1.24}$$

[3] We can invert the relations (1.22) as

$$\frac{R}{2GM} = 1 + W\left(-UV/e\right) , \quad \frac{T}{2GM} = -\log\left(\left|\frac{U}{V}\right|\right) \tag{1.20}$$

where $W(x)$ is the Principal Lambert W-function. With this coordinates the metric Eq. (1.17) reads

$$\mathrm{d}s^2 = -\frac{32(GM)^3 e^{-\frac{R}{2GM}}}{R}\mathrm{d}U\mathrm{d}V + R^2(U,V)\mathrm{d}\Omega_2^2 \tag{1.21}$$

Here R has to be seen as a function of U and V by Eqs. (1.20). The signs in Eq. (1.23) depend on whether the wall moves to the right/left on the causal diagram in Figure 1.4. Solving Eq. (1.23) with the apropriate intitial conditions will describe the trajectory of the domain wall in the $U-V$ plane [4] . The constants of integration of Eq. (1.23) can be fixed by imposing conditions on the product and ratio of U and V, which essentially define the initial value for the R coordinate and fix the origin of the T coordinate, which in order to have symmetrical solutions, will be set to zero. Note that from Eq. (1.23) we have that the left and right trajectories in Figure 1.4 are related by swapping the U and V coordinate. Eq. (1.23) will be used in the following chapters to describe the propagation of light rays across the spacetime.

Although in the following chapters we will solve Eq. (1.23) numerically, an approximate solution can be found as follows. The proper radius of the wall $R(\tau)$ as a function of the proper time τ is given by Eq. (1.18a). Finding a full solution is not possible by using only elementary solutions, and requires the use of elliptical functions. However, for the case of large supercritical domain walls, with $t_\sigma \ll 2GM$, good enough approximations can be found, at least for a specific range of R. Notice that if only consider soltutions $R \gg t_\sigma$, then the second term in Eq. (1.18a) is always larger than one. The first term is only comparable or smaller to one when $R \gtrsim 2GM$, but at this point the second term is already dominating the dynamics, so we can safely ommit the minus one term in Eq. (1.18a). Then the solution reads

$$R(\tau) = 2GM \left(\frac{t_\sigma}{2GM}\right)^{2/3} \sinh^{2/3}\left(\frac{3}{2}\frac{\tau}{t_\sigma} + C\right) \tag{1.26}$$

where the contant of integration C has to be fixed by imposing initial conditions.

1.5.1 Dust particle in Schwarschild spacetime

Here we briefly discuss the geodesic motion of a particle of dust in a Schwarzschild background. In Figure 1.4 we show with a dashed line the trajectory of a dust particle. For a particle with the escape velocity, like the ones which correspond to the flat FLRW congruence, the equations of motion are

$$\dot{R}^2 = \frac{2GM}{R}\,, \quad \dot{T} = \pm\left(1 - \frac{2GM}{R}\right)^{-1}\,. \tag{1.27}$$

[4] Alternatively, since for supercritical walls, the radius R is monotonically increaing, we can use it as parametrization of the trajectory of the wall. We can formally solve Eq. (1.18b) in terms of the radius R, leading to

$$T(R) = \pm 2GM \int_0^{\frac{R}{2GM}} \mathrm{d}z \frac{z^{5/2}}{(z-1)\sqrt{z^3 - z\left(\frac{t_\sigma}{2GM}\right)^2 + \left(\frac{t_\sigma}{2GM}\right)^2}} + \log w_i\,. \tag{1.25}$$

The integral is an elliptic integral and cannot be solved in terms of elementary functions. The $\pm$ sign in Eq. (1.25) depends on whether the wall moves to the right or the left of the causal diagram in Figure 1.4. The factors $w_i = (w_U, w_V)$ are just constants of integration that essentialy shift the origin of the T coordinate. The trajectory in the $U-V$ plane is therefore given by Eqs. (1.22) by replacing T by Eq. (1.25). The signs λ_U and λ_V in Eqs. (1.22) are fixed depending on the direction the wall moves: if the wall moves to the left, then $\lambda_U = \mathrm{sgn}(R-2GM)$ and $\lambda_V = -1$, whether if it moves to the right, then $\lambda_U = -1$ and $\lambda_V = \mathrm{sgn}(R-2GM)$.

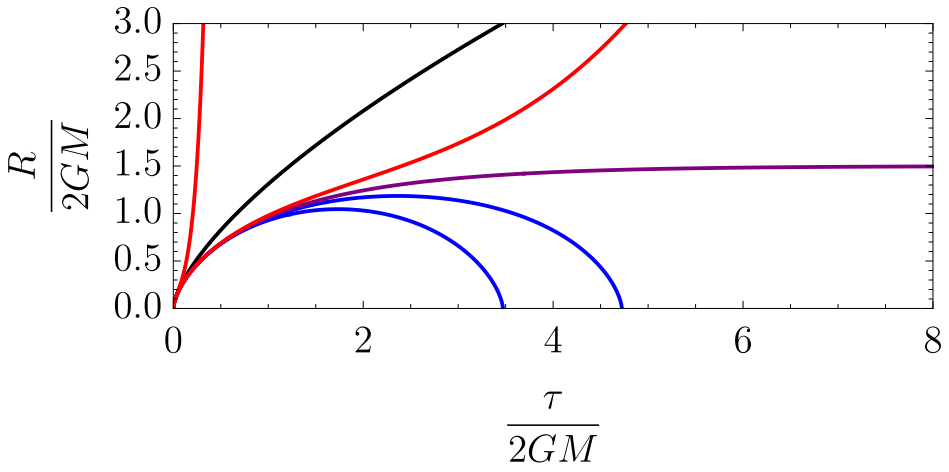

Figure 1.5: Here we show the evolution of the proper radius of the wall and dust particles as a function of the proper time, $R(\tau)$. The red solid lines correspond to supercritical values. From more to less steep, the values for t_σ are $t_\sigma = 0.01, 2.4$ in units of $2GM$. The blue solid lines correspond to subcritical domain walls, with $t_\sigma = 2.6$ and 3 in units of $2GM$. The purple solid line corresponds to the critical domain wall case, with $t_\sigma = \sqrt{27}GM$, in this case the domain wall radius is frozen at the value of $R = 3GM$.The solid black line corresponds to the radius evolution of a dust particle. Both dust particle and wall start from the white hole singularity at $R(0) = 0$.

where the $\pm$ refers to whether the dust particle moves to the right or to the left in the causal diagram. As in the case of the domain wall, we can combine Eqs. (1.27) to obtain the equation for the trajectory in the $U - V$ plane,

$$\frac{dU}{dV} = \frac{U}{V}\left(\frac{1 \mp \phi(R)}{1 \pm \phi(R)}\right) , \tag{1.28}$$

where $\phi(R) = \sqrt{R/2GM}$, and $R = R(U, V)$ by Eqs. (1.20). The signs in Eq. (1.28) depend on whether the dust particle moves to the right/left on the causal diagram in Figure 1.4. Solving Eq. (1.28) gives the trajectory of the dust particle in the $U - V$ plane[5] . As in the domain wall case, the constants of integration are determined by

[5]Similarly to the domain wall case, we can parametrize the motion of the dust particle by its physical radius R. In this case, the solution for $T(R)$ can be written as

$$T(R) = \pm 2GM\left[\frac{2}{3}\left(\frac{R}{2GM}\right)^{2/3} + 2\sqrt{\frac{R}{2GM}} - \log\left(\left|\frac{1+\sqrt{\frac{R}{2GM}}}{1-\sqrt{\frac{R}{2GM}}}\right|\right)\right] + \log d_i \tag{1.29}$$

where $d_i = (d_U, d_V)$ are just constants of integrations, and the $\pm$ depends on whether the particle moves to the right or left of the causal diagram in Figure 1.4. The trajectory in the $U - V$ plane is given by Eqs. (1.22) by replacing T with Eq. (1.29). The signs λ_U and λ_V depend on the regions that the particle covers. In the next Chapters, we will consider dust particles that only move to the right of the causal diagram, so the signs will be fixed to be $\lambda_U = -1$ and $\lambda_V = \mathrm{sgn}(R - 2GM)$.

fixing the product and the ratio of the U,V coordinates. Eq. (1.28) will be used in the following chapters.

Unlike in the domain case, here we can solve for the radius R in terms of the proper time τ in terms of elementary functions,

$$R(\tau) = 2GM \left(\frac{3}{2} \frac{\tau}{2GM} + C \right)^{2/3} \tag{1.30}$$

where the constant of integration C has to be fixed by imposing initial conditions. A plot for the time evolution can be seen in Figure 1.5, drawn in a black line.

1.5.2 Relative velocity between the wall and the particle

From Eqs. (1.18) and Eqs. (1.27) it is straightforward to compute the relative Lorentz factor between the domain wall and a dust particle at the edge of the matter dominated region.[6]

$$\gamma = \left(1 - \frac{R}{2GM} \right)^{-1} \left[\mp \frac{R}{2GM} \frac{R}{t_\sigma} + \sqrt{1 - \frac{R}{2GM} + \frac{R}{2GM} \left(\frac{R}{t_\sigma} \right)^2} \right] \tag{1.31}$$

where the $\mp$ refers to the inside or the outside.

Notice that the Lorentz factor in Eq. (1.31) coincides with the Lorentz factor given in Eq. (1.15), if we set R to be

$$R_*^3 = \frac{2GM}{H^2} \tag{1.32}$$

showing that the relative velocity between the domain wall and a co-moving observer does not change between a transition from de Sitter to Schwarzschild if this occurs when the radius of the wall is equal to R_*.

[6] This expression corrects some typos in Eq. (67) of Ref. [15].

Chapter

2 Gravitational collapse of large supercritical domain walls

In this chapter, we shall review the construction of the classical solution, describing the gravitational collapse triggered by a supercritical domain wall [15]. A conformal diagram of this spacetime is depicted in Figure 2.1, where the angular directions are suppressed. The lower part of the figure represents an inflationary phase (in blue), during which a domain wall forms by the quantum tunneling process described in Figure 1.2. The upper part corresponds to the post-inflationary evolution during which a primordial black hole forms, embedded in an otherwise homogeneous FLRW evolution. We now describe these two phases of evolution in detail.

2.1 Inflationary evolution of domain walls

After the nucleation of the domain wall, detailed in Section 1.3, its subsequent evolution is governed by Eq. (1.13). This phase is illustrated by the lower section of Figure 2.1, shaded in blue. It is important to note that the transition from the de Sitter solution depicted in the left panel of Figure 1.3 to the solution with a domain wall in the right panel is not a classical process, and thus cannot be accurately represented in a classical spacetime diagram. Rather, the left and right panels represent the initial and final semiclassical states, before and after the transition (the underbarrier evolution is described by the Coleman-de Lucia instanton [48]). In the limit of a thin wall, the metric remains continuous across the nucleation hypersurface labeled as $t = t_{nuc}$, indicated by a dashed line.[1]. The wall expands until inflation ends.

2.2 Post-inflationary evolution

So far we have concentrated on the evolution during inflation, corresponding to the blue shaded region in the lower part of the diagram in Figure 2.1. Let us now discuss

[1] While this fact holds true, its significance may be limited. Generally, the scalar field will be discontinuous if we attempt to match the solution before tunneling with the solution after tunneling.

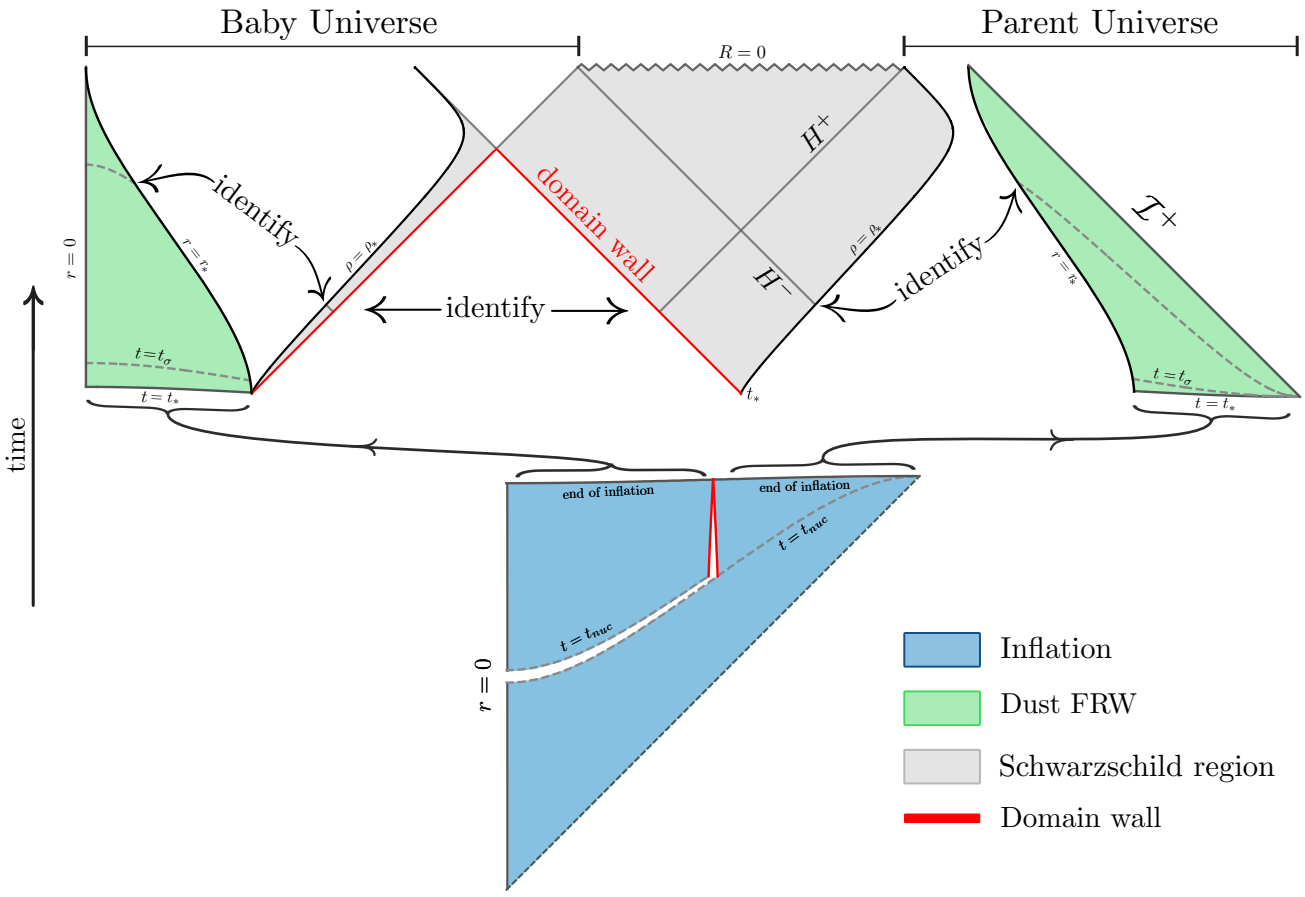

Figure 2.1: Causal diagram of the black hole spacetime produced by a large supercritical domain wall. The lower panel, shaded in blue, represents a de Sitter spacetime before and after the nucleation of a domain wall at time $t_{\rm nuc}$. The nucleation of the wall separates de Sitter in two regions which we call interior and exterior of the wall. The inflationary phase is matched with a dust FLRW universe at time t_*, shaded in green at the diagram. At that time, the large domain wall starts inflating and develops a transient wormhole connecting two regions, the baby universe (left of the diagram) and the parent universe (right of the diagram). After a time $\sim 2GM$, the wormhole pinches off, leaving behind a black hole with two horizons, one facing the parent universe, and the other facing a baby universe. The parent universe will consist of a FLRW expanding dust universe with a black hole inside it. The baby universe will consists of a vacuum region with an inflating domain wall with a ball of expanding dust inside it. In the upper panel we used the parameters $t_\sigma = 20H^{-1}$ and $R_* = 60H^{-1}$.

in some detail the post-inflationary evolution, which is represented in the upper panels of that diagram.

After inflation ends, at time $t = t_*$, walls with superhorizon size $R \gg H^{-1}$ will be moving with the Hubble flow (see Eq. (1.15)). Depending on their size at time t_σ, their evolution will be different.

Supercritical walls are larger than the cosmological horizon at the time t_σ,

$$R(t_\sigma) \gtrsim t_\sigma. \tag{2.1}$$

and their energy starts to be dominant relative to the surounding matter in a Hubble patch. At that time they start inflating, and in doing so, they create a transient wormhole connecting the parent universe with a baby universe. After a time of order $t_M \sim 2GM$, where M is the mass of matter inside the spherical domain wall, the wormhole pinches off, leaving behind a primordial black hole with two horizons, one facing the parent universe, and the other facing a baby universe, where the domain wall continues to inflate forever [15].

On the other hand, subcritical walls are smaller than the cosmological horizon at the time t_σ. In this case, they collapse under their own tension into a black hole.The collapse of a spherically symmetric subcritical domain wall in a dust dominated universe was studied in [14], taking into consideration the motion of matter that flows from the interior to the exterior as the domain wall shrinks under its tension. In this thesis, we are interested in the supercritical case Eq. (2.1), where large domain walls start inflating, instead of shrinking under their tension, before the black hole forms.

In a realistic cosmology, the end of inflation should be matched to a hot Big Bang, dominated by radiation. This process has been studied numerically in [16] for the case of supercritical walls. In general, this process is complicated by the fact that the radiation fluid moves accross the wall, which does not allow for a simple analytic description. Since we are interested in an analytical treatment, here we will assume that at the time inflation ends, the energy density ρ in the inflaton field is dumped into pressureles-matter. We also assume this process to be instantaneous, which is consistent with the conservation of the energy momentum tensor provided that the energy density is matched with continuity accross t_* (even if the pressure is discontinuous, jumping from $p = -\rho$ to $p = 0$).

Moreover, for simplicity and following [15], we will require a stronger condition on the size of the domain wall at the end of inflation,

$$R_* \equiv R(t_*) > t_\sigma \,. \tag{2.2}$$

The condition (2.2) greatly simplifies the dynamics, since it implies that at time t_* the *large* domain wall is already receding from matter[2]. This allows us to construct the resulting spacetime by gluing together different pieces of simpler solutions.

The spacetime is constructed as follows. At time t_*, the spacetime is divided in two regions, delimited by the worldsheet of the domain wall. The exterior consists of dust dominated flat FLRW universe. If Eq. (2.2) is satisfied, the wall repels the ambient matter and it gets surounded by vacuum in its immediate vicinity, with matter at a finite distance and moving away. Thus, as explained in Section 1.5, the metric in this layer consist in a segment of the extended Schwarzschild black hole solution. As time progresses, this segment becomes wider and turns out to contain the bifurcaton surface where two future event horizons meet. A spacelike surface containing the bifurcation surface has the geometry of a wormhole connecting two distinct regions with aereal radius $R > 2GM$. As for the interior region, it consists of an expanding ball of dust which is initially adjacent to the domain wall, at the time $t = t_*$. But, again, the wall recedes from matter, and a growing layer of vacuum with the Schwarzschild metric develops between the expanding ball of matter with a flat FLRW metric, and the domain wall. In the region surrounding the interior expanding ball of dust, the mass parameter is given by

$$M = \frac{4\pi}{3} R_*^3 \rho(t_*) \tag{2.3}$$

The parameter M is also the mass of the cavity which is carved out of the dust dominated parent FLRW universe. As argued in [15], consistency requires that the line element in the exterior empty layer is also given by (1.17) with (2.3). The resulting geometry is illustrated in Figure 2.2, showing show a time slice section which consist in a wormhole connecting the parent universe with the baby universe.

To illustrate the effect of the condition (2.1), we compare in Figure 2.3 the evolution of the proper radius of the domain wall and the radius of the empty cavity as seen from a co-moving observer. We show different scenarios depending on the choice of R_* and t_σ. In the case when the domain wall is not large, $R_* < t_\sigma$, we see that it enters the Hubble radius before t_σ and there is a shell crossing between the dust and the wall. On the contrary, if $R_* > t_\sigma$, just after t_*, the wall already expands faster than the edge of the empty cavity.

2.3 Propagation of light rays across the spacetime

In the preceding section, we described the collapse of a supercritical domain wall and the resulting spacetime. Here we will study how light rays are propagated across this

[2]Pressureles matter is co-moving. From Eq. (1.16), we see that if Eq. (2.2) the velocity of the wall will be negative as seen from the exterior of the wall, and negative as seen from the inside, so it always moves away from co-moving observers.

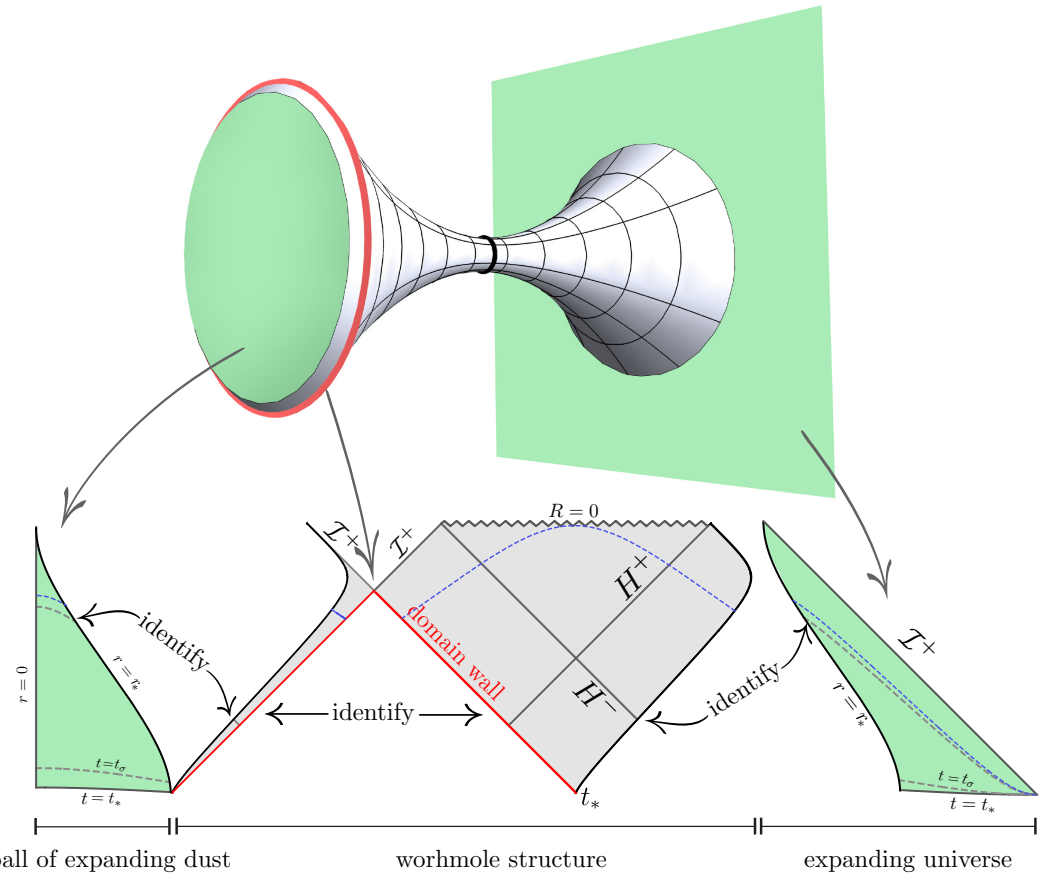

Figure 2.2: Spatial section of a spacetime representing gravitational collapse triggered by a sufficiently large spherical domain wall, depicted here as a red circle in the upper panel, where only the azimuthal and radial directions are represented. This slice corresponds to the blue dashed line on the causal diagram of the lower panel, restricted to the equatorial plane ($\theta = \pi/2$). For the Friedmann regions of the parent and baby universes (the green flat-looking pieces) we have chosen a constant cosmological time slice, while for the wormhole section we have chosen a slice of constant Kruskal time. The wormhole structure is transient, and the baby universe to the left eventually pinches off from the parent universe on the right. The domain wall drives the dynamics of the baby universe, which expands thereafter.

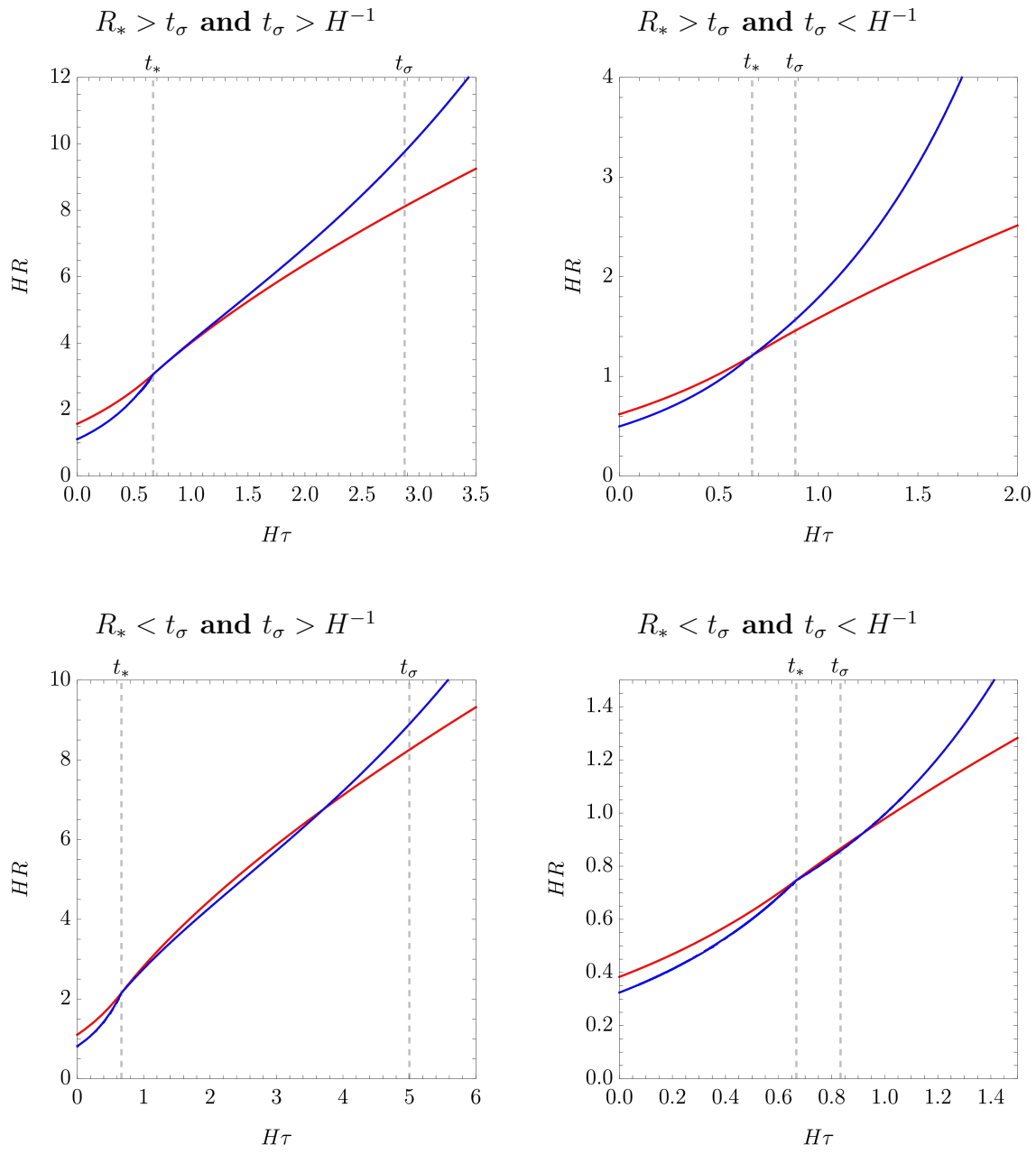

Figure 2.3: Here we show diffent the proper radius evolution of a supercritical domain wall with the choice of different parameters R_* and t_σ. The transition from dS to Schwarzshild occurs at time t_*, which is showed as a gray dashed line. We also show the time t_σ as a dashed line. In solid blue, we draw the radius of the domain wall, while in red we draw the radius of the empty cavity.

spacetime, since it will be necessary for the calculations of the stress-energy tensor in Chapter 3.

2.3.1 Propagation of light rays from dS to FLRW

After the domain wall is nucleated in de Sitter space, this is separated in two parts, which we refer as to exterior and interior of the wall. We match the interior and exterior regions with the dust FLRW universes at t_*[3] by imposing continuity of the metric and continuity of the Hubble parameters at the t_* surface.Conitnuity of the Hubble parameters requires that at t_* , $H_{\rm dS} = H_{\rm FRW}$. For a matter-dominated universe $a = (t/t_*)^{2/3}$, therfore it implies

$$t_* = \frac{2}{3} H^{-1} \tag{2.4}$$

In the other hand, continuity of the metric implies a relation between the time and radial coordinates, thus the same type of relation holds for null trajectories.

2.3.2 Propagation of light rays between FLRW and Schwarzschild

In this section we will calculate how the continuation of light rays from a dust FLRW to a Schwarzschild.

Recall that the metric for the FLRW cosmology is given by

$$\mathrm{d}s^2 = -a(\eta)^2 \left(\mathrm{d}\eta^2 + \mathrm{d}r^2 + r^2 \mathrm{d}\Omega^2\right), \tag{2.5}$$

where η is the conformal time[4], and $a(\eta)$ is the scale factor. For a dust FRW cosmology, the scale factor is given by $a(\eta) = (\eta/\eta_*)^2$, where η is the conformal time, and η_* is the conformal time at the matching surface between dS and the dust universe. Note that by using Eq. (2.4) we can write $\eta_* = 2H^{-1}$.

A dust particle at the edge of the empty cavity follows the comoving geodesic, $r = r_*$. As seen from the Schwarzschild side, this corresponds to a timelike geodesic following the edge of the empty cavity. Continuity of the metric across the geodesic implies that the proper radius of the cavity as seen as from both sides has to be the same. This, along with Friedmann equations[5] and evaluating at t_*, we obtain the relation

$$R_*^3 = \frac{2GM}{H^2} \tag{2.7}$$

[3] In the FLRW region, we normalize the scale factor at t_*, so $a_{\rm FRW}(t_*) = 1$

[4] This is related to the cosmic time t -and the proper time of comoving observers- by $a(\eta)\mathrm{d}\eta = \mathrm{d}t$, impliying $\eta \sim t^{1/3}$

[5] The Friemann equation are:

$$\left(\frac{1}{a^2}\frac{\mathrm{d}a}{\mathrm{d}\eta}\right)^2 = \frac{8\pi G}{3}\rho_m \tag{2.6}$$

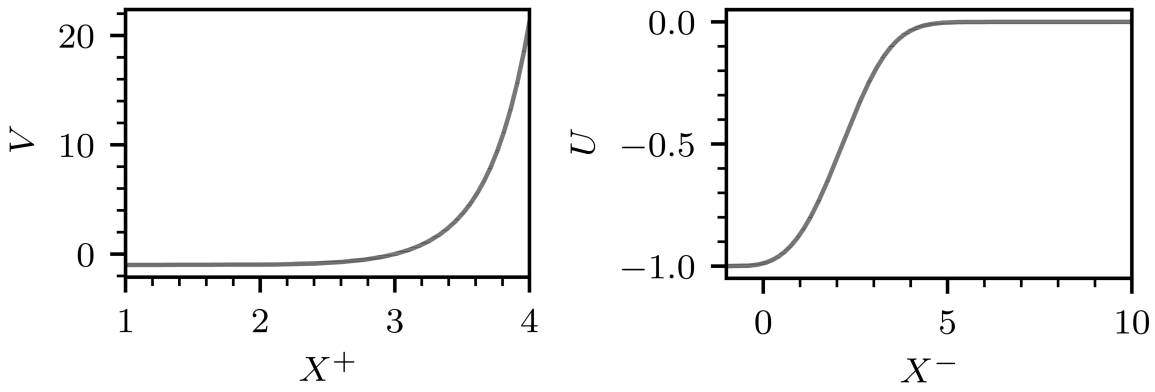

Figure 2.4: Here we show $V(X^+)$ and $U(X^-)$ solutions of Eqs. (2.11).

Note that according to Eq. (1.32), at this radius the relative velocity between comoving observers and the wall is the same. Also, the *large domain wall* condition Eq. (2.1), requires that three scales - the Schwarzschild radius of the black hole $2GM$, the inflationary rate H^{-1} and the expansion rate of the wall t_σ^{-1} - satisfy

$$\frac{2GM}{H^2 t_\sigma^3} > 1 \tag{2.8}$$

Now we are in position to obtain how light rays are propagated across the mathing surface r_*. In the FLRW, incoming and outgoing light rays can be describe by constant null coordinates

$$X^- \equiv \frac{\eta - r}{r_*}\,, \quad X^+ \equiv \frac{\eta + r}{r_*} \tag{2.9}$$

respectively. Note that in this coordinates, the empty cavity lies at $X^+ - X^- = 2$. On Schwarzschild spacetime, null geodesics can be described by constant Kruksal-Szekeres null coordinates (1.22), and the trajectory of the edge of the empty cavity is given by Eq. (1.28) (we pick the signs such that it moves to the right on the causal diagram Figure (1.4)). The matching of the two metrics implies that light rays must satisfy the following differential equations [6]

$$\frac{dU}{dX^-} = \frac{U}{8}\frac{(1+X_-)^3}{3+X_-}\,, \quad \frac{dV}{dX^+} = \frac{V}{8}\frac{(X^+-1)^3}{X^+-3} \tag{2.11}$$

[6] The solution to these equations results in

$$U(X^-) = -\frac{d_U^{-1}}{2}(X^-+3)\exp\left[P_3(-X^-)\right]\,, \quad V(X^+) = +\frac{d_V}{2}(X^+-3)\exp\left[P_3(X^+)\right] \tag{2.10}$$

where we have defined the polynomial $P_3(z) \equiv z^3/24 + 3z/8 - 5/12$ and d_i are the constants of integration. Note that, these transformations are only valid in the range $X_*^\pm < X^\pm < \infty$, where $X_*^\pm$ are the null lines that intersect t_* with r_*. The constants of integration d_i are fixed such that at the lines $X_*^\pm$ the $R(U,V) = R_*$ and $T(U,V) = 0$.

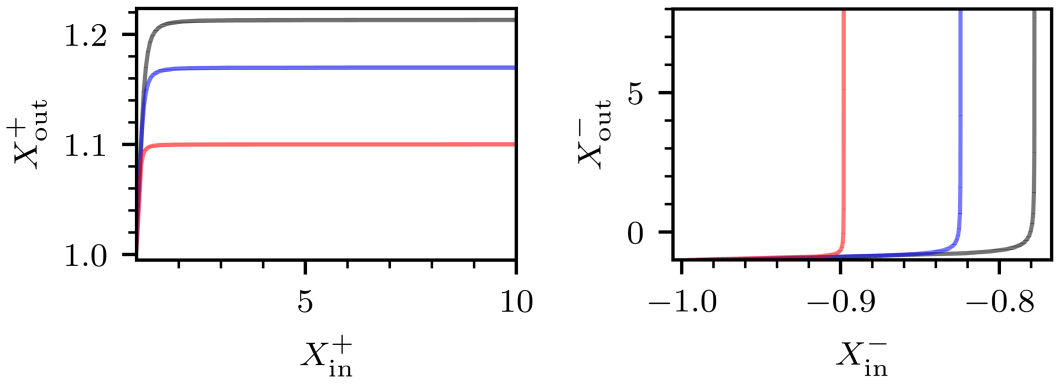

Figure 2.5: Here we show the solution of Eqs. (2.13) for different parameters of t_σ and R_*. The red line corresponds to $t_\sigma = 20H^{-1}$, $R_* = 60H^{-1}$, the blue line to $t_\sigma = 20H^{-1}$, $R_* = 35H^{-1}$ and the black line to $t_\sigma = 10H^{-1}$, $R_* = 21H^{-1}$.

In Figure 2.4 we show the solution of Eqs. (2.11).

2.3.3 Propagation of light rays across the domain wall

As shown in Section 1.5, the trajectory as seen from the inside is just a mirror image of the trajectory as seen from the interior (see Figure (1.4)). Denoting by a subscript "in" or "ext" the Kruskal coordinates in the interior or exterior regions respectively, this means that $U_{\rm in} = V_{\rm out}$ and $V_{\rm in} = U_{\rm out}$, evaluated at the wall trajectory Eq. (1.23). Therefore light rays are propagated according to

$$\frac{dU_{\rm in}}{dU_{\rm out}} = \frac{U_{\rm in}}{U_{\rm out}}\left(\frac{1-\theta(R,t_\sigma)}{1+\theta(R,t_\sigma)}\right), \quad \frac{dV_{\rm in}}{dV_{\rm out}} = \frac{V_{\rm in}}{V_{\rm out}}\left(\frac{1+\theta(R,t_\sigma)}{1-\theta(R,t_\sigma)}\right) \tag{2.12}$$

where R is the radius of the domain wall in terms of the coordinates $U_{\rm in}, U_{\rm out}$ (or $V_{\rm in}, V_{\rm out}$) by Eqs. (1.20).

2.3.4 Propagation of light rays from the interior to exterior FLRW universes

Finally, since it will used in the calculations of Chapter 3, we will show how light rays from the exterior FLRW region are propagated to the interior FLRW region.

In the following, we denote the null Friedmann coordinates defined in the interior and exterior FLRW regions by the "in" and "ext" subscripts. By applying the chain rule and combining Eqs. (1.23), (2.11) and (2.12), it can be shown that light rays need to satisfy

$$\frac{dX^\pm_{\rm out}}{dX^\pm_{\rm in}} = \frac{(X^\pm_{\rm in}\mp 1)^3}{(X^\pm_{\rm out}\mp 1)^3}\frac{X^\pm_{\rm out}\mp 3}{X^\pm_{\rm in}\mp 3}\left(\frac{1\mp\theta(R,t_\sigma)}{1\pm\theta(R,t_\sigma)}\right) \tag{2.13}$$

where R is defined at the trajectory of the domain wall[7] and $\theta(R, t_\sigma)$ is defined in Eq. (1.24). The initial conditions for Eqs. (2.13) are fixed given that $X^{\pm}_{\rm in} = X^{\pm}_{\rm out}$ at t_*. In Figure 2.5

[7] In this case R is has to be seen as a function of $X^{\pm}_{\rm in/out}$ in the following sense. First R is given in terms of U or V implicitely by combining Eqs. (1.23) and (1.20). Then U and V can be expressed in terms of $X^{\pm}_{\rm in/out}$ by using Eqs. (2.10).

Chapter

3 Energy-momentum tensor in the collapse of a supercritcal domain wall

3.1 Energy-momentum tensor for quantum fields

In the cosmological setting described in the previous Chapter (and illustrated in Figure 2.1), a black hole forms which has two future event horizons, one facing the parent universe and the other the baby universe. Our next task is to study Hawking radiation, and more generally the expectation value of the energy momentum tensor of quantum fields $\langle T_{\mu\nu}\rangle$. In general, this is a difficult task, and we shall not attempt it in 3+1 dimensions. Instead, we will consider the 1+1 dimensionally reduced metric where the angular directions are ignored. In this case, the explicit form of $\langle T_{\mu\nu}\rangle$ can be found by using the expression of the trace anomaly, the conservation of energy and momentum, and suitable conditions on an initial Cauchy surface [50]. As mentioned in the introduction, we can think of the dimensionally reduced geometry as the 1+1 dimensional worldsheet of a test string of negligible tension at fixed angular coordinates. Zero modes along the string will carry energy flux away from the black hole to infinity, at a rate which is, on dimensional grounds, comparable to the rest of bulk fields.

By using suitable coordinates (X_0, X_1) any two dimensional metric can be written as a Weyl factor times the flat metric,

$$\mathrm{d}s^2 = \Omega^2(-dX_0^2 + dX_1^2) = -\Omega^2 \mathrm{d}X_+ \mathrm{d}X_-. \tag{3.1}$$

Here, we have introduced the advanced and retarded null coordinates $X_\pm = X_0 \pm X_1$, and $\Omega(X_+, X_-)$ is the conformal factor. Consider a massless field in 1+1 dimensions. Its classical action is invariant under conformal rescalings, which would result in a vanishing trace of the energy momentum tensor. Renormalization of the quantum effective action, however, leads to a non-vanisihing anomalous trace (see e.g. [51, 52])

$$\langle T^\alpha_\alpha \rangle = \frac{\mathcal{R}}{24\pi} \tag{3.2}$$

where $\mathcal{R} = 8\Omega^{-2}\partial_+\partial_- \log\Omega$ is the Ricci scalar of the metric (3.1). Note that the trace is independent of the quantum state of the scalar field, and it is given solely from

geometric invariants. The tensor $\langle T_{\mu\nu}\rangle$ is also convariantly conserved,

$$\nabla^{\mu}\langle T_{\mu\nu}\rangle = 0, \tag{3.3}$$

which follows from diffeomorphism invariance.

From (3.2) and (3.3), the components of the expectation value of $T_{\mu\nu}$ in null coordinates can be expressed as [50]

$$\begin{aligned} T_{--} &= -\frac{1}{12\pi}\Omega\partial_{-}^{2}\Omega^{-1} + F(X_{-}), \\ T_{++} &= -\frac{1}{12\pi}\Omega\partial_{+}^{2}\Omega^{-1} + G(X_{+}), \\ T_{+-} &= -\frac{\Omega^{2}}{4}T = -\frac{1}{12\pi}\partial_{+}\partial_{-}\log\Omega. \end{aligned} \tag{3.4}$$

Here, and in what follows, we drop the $\langle\ \ \rangle$ symbol to express expectation values. For completeness, the relations (3.4) are rederived in Appendix C. The funcions $F(X_{-})$ and $G(X_{+})$ are independent of Ω, and they appear when integrating (3.3). Physically, they will be determined by imposing boundary conditions on an initial a Cauchy surface, and they encode the freedom in choosing the quantum state in which we are computing the expectation value.

Our strategy will be the following. First, we will determine the functions F and G in the inflating region. After that, we will propagate the energy-momentum tensor to the post-inflationary epoch. Note that the different regions in Figure 2.1 have different coordinate systems adapted to their symmetries. As we cross from one region to the next, we must relate the components of the stress tensor in one coordinate system to the components in another coordinate system, accross the boundaries. Consider, for definiteness, a change of coordinates $\{X_{+}, X_{-}\} \to \{Y_{+}, Y_{-}\}$. Since $T_{\mu\nu}$ transforms covariantly, we have

$$T^{Y}_{\pm\pm} = \left(\frac{\mathrm{d}X_{\pm}}{\mathrm{d}Y_{\pm}}\right)^{2} T^{X}_{\pm\pm}, \quad T^{Y}_{+-} = \left(\frac{\mathrm{d}X_{+}}{\mathrm{d}Y_{+}}\right)\left(\frac{\mathrm{d}X_{-}}{\mathrm{d}Y_{-}}\right) T^{X}_{+-}, \tag{3.5}$$

where the X and Y superindices refer to which set of coordinates we are using. The metric is also a tensor, and so the conformal factor changes as

$$\Omega^{2}(X_{\pm}) \to \Omega^{2}(Y_{\pm}) = \left(\frac{\mathrm{d}X_{+}}{\mathrm{d}Y_{+}}\right)\left(\frac{\mathrm{d}X_{-}}{\mathrm{d}Y_{-}}\right)\Omega^{2}(X_{\pm}). \tag{3.6}$$

Hence, the functions $F(X_{-})$ and $G(X_{+})$ themselves transform to (see Appendix C for details)

$$\begin{aligned} F(Y_{-}) &= \left(\frac{\mathrm{d}Y_{-}}{\mathrm{d}X_{-}}\right)^{-2}\left[F(X_{-}) + \frac{1}{24\pi}\{Y_{-}, X_{-}\}\right], \\ G(Y_{+}) &= \left(\frac{\mathrm{d}Y_{+}}{\mathrm{d}X_{+}}\right)^{-2}\left[G(X_{+}) + \frac{1}{24\pi}\{Y_{+}, X_{+}\}\right], \end{aligned} \tag{3.7}$$

where $\{A, B\}$ is the Schwarzian derivative, defined as

$$\{A, B\} = \left(\frac{\mathrm{d}A}{\mathrm{d}B}\right)^{-1}\left(\frac{\mathrm{d}^3A}{\mathrm{d}B^3}\right) - \frac{3}{2}\left(\frac{\mathrm{d}A}{\mathrm{d}B}\right)^{-2}\left(\frac{\mathrm{d}^2A}{\mathrm{d}B^2}\right)^2 \tag{3.8}$$

In the Appendix D we enumerate some properties of the Schwarzian derivative that will be useful for the calculations in the next section.

3.2 Energy-momentum tensor in a gravitational collapse caused by a domain wall

In this Section we compute the $T_{\mu\nu}$ in the geometry described in Chapter 2. Before proceding, let us introduce some notation. In order to use Eqs. (3.4) we need to use null coordinates, that are the suited ones to describe light rays. In the two patches of Schwarzschild spacetime we will use the Kruskal-Szekeres null coordinates, $\{U, V\}$ introduced in Eq. (1.22). In the FLRW regions, we will use $\{X^-, X^+\}$ defined in Eq. (2.9). Finally, in the dS region, we can define analogous coodrinates as Eq. (2.9) in the flat chart, denoted by $\{x^-, x^+\}$, with $x^\pm = H(\eta \pm r)$[1]. To distinguish between interior and exterior regions of the wall, we will use the subscript "in" and "out". For the arbritary functions F and G in the stress-energy tensor we will use a subscript to denote the regions at which they are computed.

Moreover, we define $X^-_{\mathrm{out},*}$, the outgoing null surface intersecting the surfaces $t = t_*$ and $r = r_*$ in the FRW dust expanding universe, which has the value of R_*. For the inside region of the wall, we define $X^+_{\mathrm{in},*}$ and $X^-_{\mathrm{in},*}$ to be the ingoing and outgoing null surfaces intersecting $t = t_*$ and $r = r_*$ in the ball of expanding dust. Also, we define $X^-_{\mathrm{in},\circ}$ as the continuation of the null $X^+_{\mathrm{in},*}$ when it reflects to $r = 0$, and by $U_{\mathrm{in},\circ}$ its continuation through the dust particle trajectory at $r = r_*$. Finally, we denote by $X^-_{\mathrm{in},0}$ the outgoing null surface that intersects t_* and $r = 0$. Note that $X^-_{\mathrm{in},*} = X^-_{\mathrm{out},*}$. Also, it can be checked that for both interior and exterior regions $X^\pm_{\mathrm{in/out},*} = \pm 1 + 2(HR_*)^{-1}$.

A detailed diagram of the spacetime, ommiting the inflationary epoch, is depicted in Figure 3.1. In the next subsections we compute the stress-energy tensor in each one of the regions.

[1] With this coordinates, the dS metric in the flat chart reads

$$\mathrm{d}s^2 = -\frac{4}{H^2(x^+ + x^-)^2}dx^-dx^+ \tag{3.9}$$

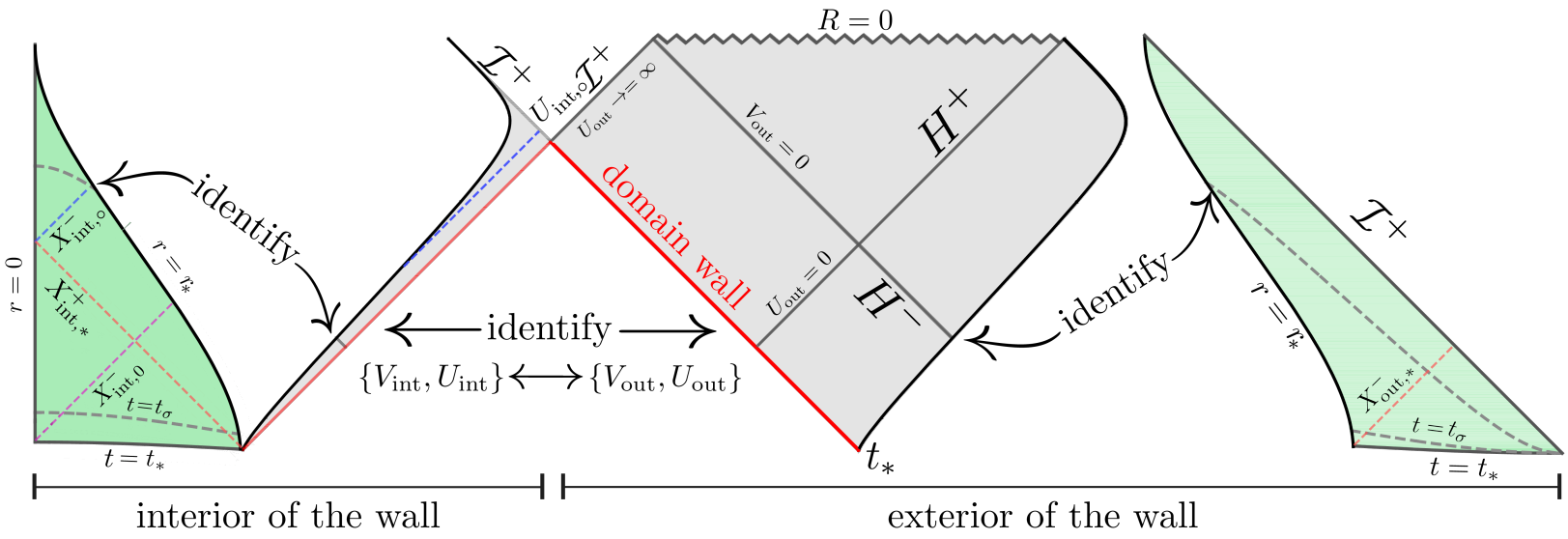

Figure 3.1: A more detailed diagram of the spacetime resulting from the collapse of a supercritical domain wall. We define $X^-_{\text{out},*}$, the outgoing null surface intersecting the surfaces $t=t_*$ and $r=r_*$ in the FLRW dust expanding universe. For the inside region of the wall, we define $X^+_{\text{in},*}$ and $X^-_{\text{in},*}$ to be the ingoing and outgoing null surfaces intersecting the surfaces $t=t_*$ and $r=r_*$ in the ball of expanding dust, and by $X^-_{\text{in},0}$ the outgoing null surface that intersects t_* and $r=0$. Also, we denote by $X^-_{\text{in},\circ}$ the continuation of the null $X^+_{\text{in},*}$ when it reflects to $r=0$, and by $U_{\text{in},\circ}$ its continuation through the dust particle trajectory at $r=r_*$. On the diagram, $X^-_{\text{in},*}$ is not drawn but has the same value as $X^-_{\text{out},*}$.

3.2.1 Energy-momentum tensor in de Sitter and initial conditions

The energy-momentum tensor of a scalar field in the de Sitter vaccum is given by [53]

$$T^{\mathrm{dS}}_{\mu\nu} = \frac{1}{48\pi}\mathcal{R}g_{\mu\nu} \tag{3.10}$$

where $\mathcal{R} = 2H^2$, which in $x^{\pm}$ coordinates its components read

$$T^{\mathrm{dS}}_{++} = T^{\mathrm{dS}}_{--} = 0\,, \quad T^{\mathrm{dS}}_{+-} = +\frac{1}{12\pi\,(x^+ + x^-)^2}\,. \tag{3.11}$$

Using the terminology from the previous section, it can be stated that the de Sitter vacuum is characterized by setting the functions $F_{\mathrm{dS}}(x^-)$ and $G_{\mathrm{dS}}(x^+)$ to be zero.

It turns out that in the presence of a domain wall, the stress-energy tensor is still the same[2]. This can be argued as follows. Suppose a ray comming from a time surface, $\tilde{t} < t_{\mathrm{nuc}}$ before the nucleation of the wall. At that time, the stress-energy tensor is given by Eq. (3.10). When the domain wall nucleates, the spacetime splits into two regions, the interior and the exterior of the wall, and the ray will be in one of these regions. The functions F and G change only at the transition from one region to the other, since this is when a change in coordinates occurs.

It can be shown that null interior and exterior coordinates are related by [3]

$$x^-_{\mathrm{int}} = \frac{x^-_{\mathrm{out}} - \beta_0}{1 - x^-_{\mathrm{out}}\beta_0}\,, \quad x^+_{\mathrm{int}} = \frac{x^+_{\mathrm{out}} - \beta_0}{1 - x^+_{\mathrm{out}}\beta_0} \tag{3.12}$$

Since these are Möbius transformations, it's Schwarzian derivative is zero (see Eq. (D.1)) so the F_{dS} and G_{dS} remain unchanged and are still zero at any time after the nucleation.

Moreover, we can observe that the transition to the post-inflationary epoch preserves

[2] This is not the case in general. In the four dimensional case, the stress-energy tensor changes after the nucleation of the wall.

[3] This can be obtained as follows: from the continuity equation Eq. (1.14), we can solve a second degree equation for $\eta_{\pm} = -H^{-1}e^{-Ht_{\pm}}$, leading to

$$\eta_+ = (\eta_-^{-1} - 2\beta_2)^{-1}\,.$$

Moreover, since $r_{\pm} = \sqrt{1 \mp 2\beta_0\eta_{\pm} + \eta_{\pm}^2}$, we can combine it with the previous equation and get the relation

$$r_- = \frac{r_+}{1 - 2\beta_0\eta_+}\,.$$

From here and using the definition for x^-_{int} and x^-_{out} we get the Möbius relation. A similar reasoning can be done for x^+.

the values of the functions $F_{\rm dS}(x^-)$ and $G_{\rm dS}(x^-)$. As described in 2.3, the relation between coordinates during the transition is linear, resulting in a vanishing Schwarzian derivative. Consequently, we can set to zero the functions $F_{\rm FRW}(X^-)$ and $G_{\rm FRW}(X^+)$ for all rays originating directly from the t_* surface.

3.2.2 Energy-momentum tensor in the parent universe

We now compute the stress-energy tensor for the parent universe (PU). In this region, the conformal factor is given by $\Omega^2 = (GM)^2/64\,(X^+ + X^-)^4$. Therefore, according to Eqs. (3.4), the stress-energy tensor in null coordinates (2.9) reads

$$\begin{aligned} T^{\rm PU}_{--} &= -\frac{1}{2\pi(X^+_{\rm out}+X^-_{\rm out})^2} + F_{\rm PU}(X^-_{\rm out}) \\ T^{\rm PU}_{++} &= -\frac{1}{2\pi(X^+_{\rm out}+X^-_{\rm out})^2} + G_{\rm PU}(X^+_{\rm out}) \\ T^{\rm PU}_{+-} &= \frac{1}{6\pi(X^+_{\rm out}+X^-_{\rm out})^2} \end{aligned} \tag{3.13}$$

The calculation of $F_{\rm PU}(X^-_{\rm out})$ can be done by tracking the outgoing rays. Note that those with $X^-_{\rm out} < X^-_{{\rm out},*}$ originate at the surface t_* in the parent universe, so we can impose initial conditions there. This implies that

$$F_{\rm PU}(X^-_{\rm out}) = 0\,, \qquad \text{for } X^-_{\rm out} < X^-_{{\rm out},*} \tag{3.14}$$

For the outgoing rays with $X^-_{\rm out} > X^-_{{\rm out},*}$, the situation is more complex. When we trace back these rays, we need to cross the domain wall. Some of them hit the t_* surface directly inside the baby universe, while others reflect first at $r = 0$. For the later, it may be tempting to consider a ray coming from the parent universe that enters the baby universe, reflects at $r = 0$, and then returns to the parent universe. However, this situation cannot occur. The earliest ray that reflects at $r = 0$ and can be traced back to the parent universe is at $X^-_{\rm in} = X^-_{\rm in,}$, and its continuation to the vacuum interior region is the line $U_{\rm in} = U_{\rm in,\circ}$. Defining $U_{\rm in,\infty}$ as the null surface at which the domain wall hits $\mathcal{I}^+$ as seen from the inside, it can be checked that for supercritical walls, $U_{\rm in,\infty} < U_{\rm in,*}$, thus proving that all outgoing rays with $X^-_{\rm out} > X^-_{{\rm out},*}$ come from the t_* surface in the baby universe. Therefore, by using Eq. (3.7) we can write

$$F_{\rm PU}(X^-_{\rm out}) = -\frac{1}{24\pi}\{X^-_{\rm in}, X^-_{\rm out}\}\,, \qquad \text{for } X^-_{\rm out} > X^-_{{\rm out},*} \tag{3.15}$$

where we have used the property Eq. (D.2) and simplified by putting $F_{\rm BU}(X^-_{\rm in}) = 0$. The remaining Schwarzian derivative can be evaluated through multiple applications of the chain rule (D.3). The analytical form of $F_{\rm PU}(X^-_{\rm out})$ is long and somewhat cumbersome so we leave the full expression in Eq. (E.4) of Appendix E.1.

The function $F_{\rm PU}(X^-_{\rm out})$ is not continuous through the line $X^-_{\rm out} = X^-_{\rm out,*}$, with in terms of R_* can be written as $X^-_{\rm out,*} = -1 + 2(HR_*)^{-1}$. In the case where $t_\sigma \gg H^{-1}$ and $R^* \gg H^{-1}$, the jump is

$$\Delta F_{\rm PU}(X^-_{\rm out,*}) \approx \frac{1}{4\pi}\frac{HR_*^2}{t_\sigma} \tag{3.16}$$

The full expression for $\Delta F_{\rm PU}(X^-_{\rm out,*})$ is written in Eq. (E.5) in the Appendix E.1. Note that by the condition Eq. (2.8), the magnitude of the jump $\Delta F_{\rm PU}$ is large. This discontinuity is a direct contribution from the formation of the wormhole, and it will have important consequences on the observed fluxes and energy densities. For large $X^-_{\rm out}$, the function grows as $F_{\rm PU}(X^-_{\rm out}) \sim -\left(X^-_{\rm out}\right)^4/3072\pi$.

The calculation of $G_{\rm PU}(X^+_{\rm out})$ is straightforward. All incoming rays come from the t_* surface in the parent universe itself, so there is no mixing between "in" and "out" coordinates. Therefore

$$G_{\rm PU}(X^+_{\rm out}) = 0 \tag{3.17}$$

for all $X^+_{\rm out}$.

3.2.3 Energy-momentum tensor in the baby universe

Here we compute the $T_{\mu\nu}$ in the baby universe (BU). The conformal factor is the same as in the parent universe, with just a relabeling of the coordinates. Therefore, the stress energy tensor is given by the same expressions as in Eqs. (3.13) but now the functions F and G are different. For the calculation of the function $G_{\rm BU}(X^+_{\rm in})$ we need to trace back the incoming rays. Light rays with $X^+_{\rm in} < X^+_{\rm in,*}$ proceed from the t_* surface inside the baby universe, so

$$G_{\rm BU}(X^+_{\rm in}) = 0\,, \quad \text{for } X^+_{\rm in} < X^+_{\rm in,*}\,, \tag{3.18}$$

On the other hand, rays with $X^+_{\rm in} > X^+_{\rm in,*}$ proceed from the t_* in the parent universe, so $G_{\rm BU}(X^+_{\rm in})$ has to be computed using Eqs. (3.7). Since $G_{\rm PU}(X^+_{\rm out}) = 0$, we use Eqs. (3.7) to write

$$G_{\rm BU}(X^+_{\rm in}) = -\frac{1}{24\pi}\left\{X^+_{\rm out}, X^+_{\rm in}\right\}\,, \quad \text{for } X^+_{\rm in} > X^+_{\rm in,*}\,. \tag{3.19}$$

The full expression for $G_{\rm BU}(X^+_{\rm in})$ can be found in Eq. (E.8) of the Appendix E.2, where we have applied the chain rule Eq. (D.3) to expand the Schwarzian derivative in terms of simpler Schwarzian derivatives that can be computed explicitely.

For large $X^+_{\rm in}$ it can be checked that it decays to zero quadratically, $G_{\rm BU}(X^+_{\rm in}) \sim 1/6\pi\left(X^+_{\rm in}\right)^2$. At the line $X^+_{\rm in,*}$, the function $G_{\rm BU}(X^+_{\rm in,*})$ has also a discontinuity, and it coincides with the same value as in the case of $F_{\rm PU}(X^-_{\rm out})$, which for $t_\sigma \gg H^{-1}$ and $R_* \gg H^{-1}$ is just

$$\Delta G_{\rm BU}(X^+_{\rm in,*}) \approx \frac{1}{4\pi}\frac{HR_*^2}{t_\sigma} \tag{3.20}$$

In order to compute $F_{\rm BU}(X^-_{\rm in})$ we trace back the outgoing rays. All light rays with $X^-_{\rm in} < X^-_{\rm in,\circ}$ proceed directly from the t_* surface in the baby universe (rays with $X^-_{\rm in,0} < X^-_{\rm in} < X^-_{\rm in,\circ}$ reflect at $r = 0$ first). Therefore,

$$F_{\rm BU}(X^-_{\rm in}) = 0\,, \qquad \text{for } X^-_{\rm in,*} < X^-_{\rm in} < X^-_{\rm in,\circ}\,. \tag{3.21}$$

The case of light rays with $X^-_{\rm in} > X^-_{\rm in,\circ}$ needs more care. These reflect at $r = 0$, cross the domain wall and eventually hit the t_* surface in the parent universe. After the reflection, the rays need to be treated as incoming rays, so

$$F_{\rm BU}(X^-_{\rm in}) = G_{\rm BU}(X^+_{\rm in} \to X^-_{\rm in})\,, \qquad \text{for } X^-_{\rm int} > X^-_{\rm int,\circ}. \tag{3.22}$$

with $G_{\rm BU}(X^+_{\rm in})$ given by Eq. (3.19). This also implies a discontinuity at the line $X^-_{\rm int,*}$.

3.2.4 Energy-momentum tensor in the exterior vacuum

Here we compute the $T_{\mu\nu}$ in the the exterior vacuum (EV) region of the domain wall. The conformal factor in this Schwarzschild region is given by $\Omega^2 = 32(GM)^2 e^{-\frac{R}{2GM}}/R$, so the $T_{\mu\nu}$ reads

$$\begin{aligned} T^{\rm EV}_{--} &= \frac{w(R)}{48\pi U^2_{\rm out}} + F_{\rm EV}(U_{\rm out}) \\ T^{\rm EV}_{++} &= \frac{w(R)}{48\pi V^2_{\rm out}} + G_{\rm EV}(V_{\rm out}) \\ T^{\rm EV}_{+-} &= -\frac{4(GM)^4 e^{-\frac{R}{2GM}}}{3\pi R^4} \end{aligned} \tag{3.23}$$

where we have defined the funcion $w(R) = 1 - 4(2GM/R)^3 + 3(2GM/R)^4$ and R is given in terms of the Kruskal coordinates by Eq. (1.20).

To compute the function $G_{\rm EV}(V_{\rm out})$, we need to trace back the incoming light rays. From the diagram in Figure (3.1), it can be seen that all incoming rays come from the t^*-surface in the exterior universe. Since $G_{\rm PU}(X^+_{\rm out}) = 0$, by using Eq. (3.7) we have

$$G_{\rm EV}(V_{\rm out}) = \frac{1}{24\pi}\left(\frac{dV_{\rm out}}{dX^+_{\rm out}}\right)^{-2}\left\{V_{\rm out}, X^+_{\rm out}\right\} \tag{3.24}$$

for all $V_{\rm out}$. The full expression is given in Eq. E.10 of the Appendix E.3.

To calculate $F_{\rm EV}(U_{\rm out})$, we can note that all the outgoing rays entering the vacuum region originate from the baby universe. Incoming rays born at the parent universe that cross the wall, enter the baby universe and reflect at $r = 0$, ultimately reach $\mathcal{I}+$ in the interior vacuum region and do not cross the wall again. Since $F_{\rm BU}(X^-_{\rm int}) = 0$, the expression for $F_{\rm EV}(U_{\rm out})$ simplifies to

$$F_{\rm EV}(U_{\rm out}) = \frac{1}{24\pi}\left(\frac{dU_{\rm out}}{dX^-_{\rm int}}\right)^{-2}\left\{U_{\rm out}, X^-_{\rm int}\right\} \tag{3.25}$$

The remaining calculations can be done by applying the chain rule for the Schwarzian derivative Eq. (D.3). The full expression for $F_{\rm EV}(U_{\rm out})$ is written in Eq. (E.12) in the Appendix E.4. Note that $F_{\rm EV}(U_{\rm out})$ is regular at the past horizon H^{-1}, corresponding to $U_{\rm out}=0$. Moreover, for large $U_{\rm out}$, it decays to zero as $F_{\rm EV}(U_{\rm out})\sim -1/48\pi U_{\rm out}^2$.

3.2.5 Stress tensor in the interior vacuum

Here we compute the $T_{\mu\nu}$ for the interior vacuum region (IV), inside the domain wall. The conformal factor is the same as the one in the exterior vacuum, so the stress-energy tensor is given by Eqs. (3.23) with just a relabeling of the coordinates. The funcion $G_{\rm IV}(V_{\rm int})$ can be calculated by tracing the incoming rays. Observe in the diagram of Figure 3.1 that all incoming rays, $V_{\rm int}=$ constant, come from the t_*-surface in the parent universe. Therefore, by Eqs. (3.7) we have

$$G_{\rm IV}(V_{\rm int})=\frac{1}{24\pi}\left(\frac{dV_{\rm int}}{dX^+_{\rm out}}\right)^{-2}\left\{V_{\rm int},X^+_{\rm out}\right\} \tag{3.26}$$

where we have used the fact that $G_{\rm PU}(X^+_{\rm out})=0$. The evaluation of the Schwarzian derivative can be done by expanding it in simpler derivtives by using the chain rule. The resulting expression for $G_{\rm IV}(V_{\rm int})$ is long and it can be found in Eq. (E.14) the Appendix E.5.

The computation of the function $F_{\rm IV}(U_{\rm in})$ is a bit more involved than the one for $G_{\rm IV}(V_{\rm in})$ and has some subtleties. Note that there are three types of outgoing rays that will enter the interior vacuum region. The first ones start at the t_*-surface in the baby universe and go outwards directly. These have $X^-_{\rm int,*}<X^-_{\rm int}<X^-_{\rm int,0}$, that in the interior vaccum region translate to the condition $U_{\rm int}<U_{\rm int,\circ}$. The second ones are the ones that have $X^-_{\rm int,0}<X^-_{\rm int}<X^-_{\rm int,\circ}$, and start at the t_*-surface being incoming rays $X^+_{\rm int}=$ constant, reflect at $r=0$ and become outgoing rays with some $X^-_{\rm int}=$ constant. Finally, outgoing rays with $X^-_{\rm int}>X^-_{\rm int,\circ}$, or equivalently $U_{\rm int}>U_{\rm int,\circ}$, will start at the t_*-surface in the parent universe as an ingoing ray, enter to the baby universe, reflect at $r=0$ and turn into an outgoing ray. In general, the expression for $F_{\rm IV}(U_{\rm int})$ is given by Eq. (3.7),

$$F_{\rm IV}(U_{\rm int})=\left(\frac{dU_{\rm int}}{dX^-_{\rm int}}\right)^{-2}\left(F_{\rm BU}(X^-_{\rm int})+\frac{1}{24\pi}\left\{U_{\rm int},X^-_{\rm int}\right\}\right)\,. \tag{3.27}$$

The rays of first and second type cross only the FLRW-Schwarzschild boundary, and Eq. (3.27) can be simplified by setting $F_{\rm BU}(X^-_{\rm int})=0$. For the third type of rays we need to take more care. The form of $F_{\rm IV}(U_{\rm int})$ remains the same as Eq. (3.27), but since the rays proceed from the parent univers, $F_{\rm BU}(X^-_{\rm int})$ is not zero. An outgoing light ray with $X^-_{\rm int}$ constant, becomes an incoming ray $X^+_{\rm int}$ with the same constant when it reflects at $r=0$, therefore $F_{\rm BU}(X^-_{\rm int})$ has the same functional form as $G_{\rm BU}(X^+_{\rm int})$ with the replacement $X^+_{\rm int}\to X^-_{\rm int}$. A full expression for $F_{\rm IV}(U_{\rm int})$ can be found in Eqs.

(E.15) and (E.16) of the Appendix E.6.

In Figure 3.2 we show a heatmap for the fluxes, energy density and pressure measured by Friedmann comoving observers (within the FLRW regions) and by Kruskal observers (whithin the Schwarzschild regions). A deeper study on these measured quantities is done in Chapter 4.

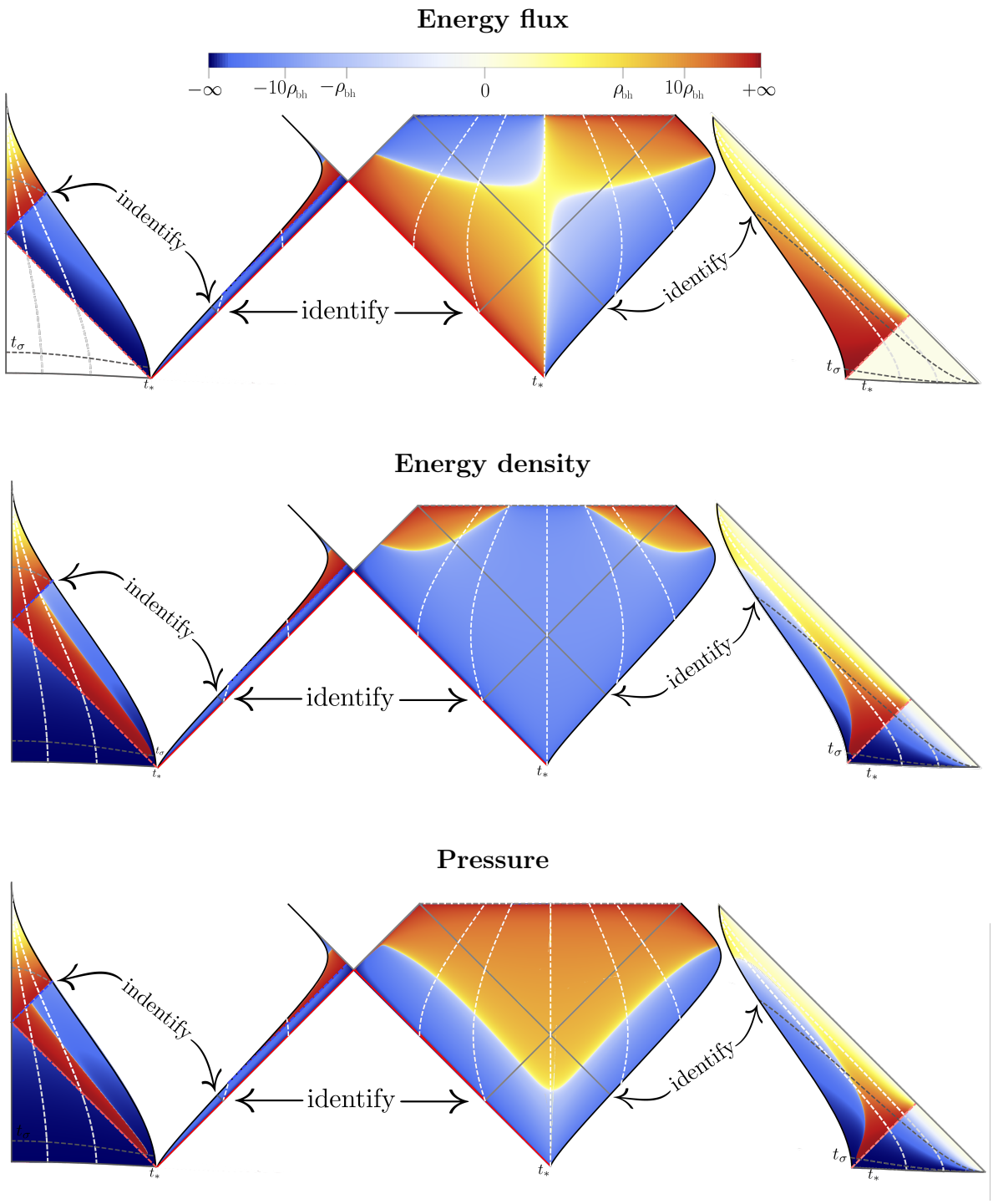

Figure 3.2: A heatmap of the fluxes, energy density and pressure measured by Friedmann and Kruskal observers, defined as $X^+ - X^- =$ constant and $V - U =$ constant respectively. Friedmann observers are defined in the FLRW regions, while Kruskal observers are defined in the Schwarzschild regions. The flux for such observers is defined as $\Phi = \Omega^{-2}\left(T_{--} - T_{++}\right)$, where Ω is the conformal factor of the region it is calculated.The energy density is given by $\rho = \Omega^{-2}\left(T_{--} + T_{++} + 2T_{+-}\right)$. Finally, the pressure reads $p = \Omega^{-2}\left(T_{--} + T_{++} - 2T_{+-}\right)$.

Chapter

4 Energy density, pressure and fluxes

In the preceding chapter, we calculated the stress-energy tensor $T_{\mu\nu}$ of a massless scalar field as it propagates through the spacetime resulting from the collapse of a supercritical domain wall. In this Chapter, we examine the history of different types of observers moving through the spacetime by computing their mesured energy density, flux and pressure, all of which can be extracted from the stress-energy tensor.

Consider an observer with trajectory $x^\mu(\tau)$ parametrized by its proper time τ, and let us denote its 4-velocity by $u^\mu(\tau)$. Additionally, we introduce the normal vector to the trajectory, denoted as n^μ, which satisfies $n^\mu u_\mu = 0$ and $n^\mu n_\mu = 1$. For such observer, we define the measured energy density $\rho = T_{\mu\nu}u^\mu u^\nu$, the pressure $p = T_{\mu\nu}n^\mu n^\nu$, and flux density of energy $\Phi = -T_{\mu\nu}u^\mu n^\nu$. In order to make use of the results of Chapter **??**, we consider 1+1 trajectories defined in terms of null coordinates $A_\pm$. In this case, the 4-velocity and normal vector are given by $u^\mu(\tau) = (\dot{A}_+, \dot{A}_-)$ and $n^\mu(\tau) = (\dot{A}_-, \dot{A}_+)$ respectively. Therefore we can write

$$\begin{aligned} \rho &= T_{++}\dot{A}_+^2 + T_{--}\dot{A}_-^2 + 2T_{+-}\dot{A}_-\dot{A}_+ \\ p &= T_{++}\dot{A}_+^2 + T_{--}\dot{A}_-^2 - 2T_{+-}\dot{A}_-\dot{A}_+ \\ \Phi &= T_{--}\dot{A}_-^2 - T_{++}\dot{A}_+^2 \end{aligned} \tag{4.1}$$

Let us recall for the sake of comparison that the energy density of a scalar field at the Hawking temperature in a 1+1 spacetime is given by [1]

$$\rho_{\rm bh} = \frac{1}{768\pi(GM)^2}\,.$$

Additionally, in a de Sitter space, since $T^{\rm dS}_{\mu\nu} \propto g_{\mu\nu}$, the energy density measured by any observer is

$$\rho_{\rm dS} = -\frac{H^2}{24\pi}\,,$$

[1] This can be easily obtained by recalling that the energy density of a two-dimenisonal bosonic gas at temperature T is

$$\rho = \frac{1}{2\pi}\int_0^\infty \frac{\omega}{e^{\omega/T}-1}\mathrm{d}\omega = \frac{\pi}{12}T^2$$

and for a Schwarschild black hole, the Hawking temperature is $T = (8\pi M)^{-1}$.

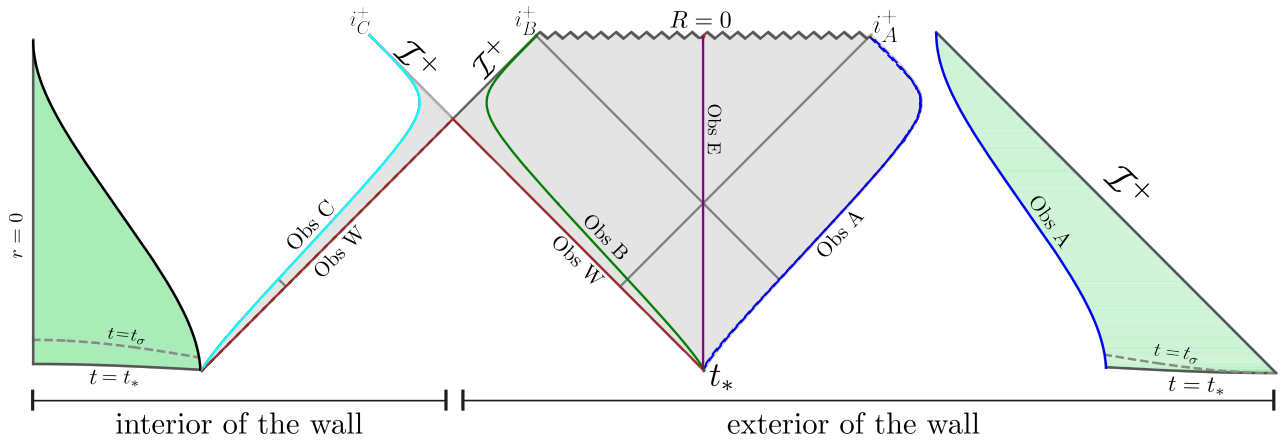

Figure 4.1: Depicted are the trajectories of the observers described in Section 4.1.

the pressure has the same magnitude but with opposite sign and no fluxes are observed.

4.1 Comparing observations along different geodesics

In this section we compare the experiences of five different observers whose wordlines are very similar during the inflationary epoch, but whose fate is different once inflation ends. This will give us an overall picture of the distribution of energy, pressure and fluxes in different regions of spacetime. Three of these observers move exactly at the escape velocity Unfortunately, the forth one does not (with severe consequences). The fifth observer rides along the wall into future null infinity. The trajectories of these observers are depicted in the causal diagram of Figure 4.1.

Observer A (The Parent)

This observer follows the edge of the empty cavity within the parent universe. In this sense, it represents FLRW observers which are in the vicinity of the PBH at the time of formation. Its trajectory is described in terms of the proper time τ by $x_A^\mu = (X_A^-(\tau), X_A^+(\tau))$, where $X_A^\pm(\tau) = (6\tau/GM)^{1/3} \pm 1$ for $\tau > t_*$. Its path is represented in Figure 4.1 as a dark blue line.

The flux measured by this observer will be

$$\Phi_A(\tau) = \frac{4}{(GM)^2}\left(\frac{GM}{6\tau}\right)^{4/3} F_{\rm PU}\left(X_A^-(\tau)\right) \tag{4.2}$$

where $F_{\rm PU}\left(X_A^-\right)$ is given in Eq. (E.4). Just after inflation, this observer measures an outgoing flux at $\tau = t_*$, due to the discontinuity of the function $F_{\rm PU}\left(X^-\right)$ in Eq. (3.16).

For large supercritcal domain walls with $R_* \gg H^{-1}$ and $t_\sigma \gg H^{-1}$, this flux has a magnitude of

$$\Phi_A(t_*) \approx \frac{1}{4\pi}\frac{H}{t_\sigma} + \mathcal{O}\left(t_\sigma^{-2}\right) \tag{4.3}$$

which depends only on the tension of the wall and H. The magnitude of such flux is smaller, about a factor $\sim 6(Ht_\sigma)^{-1}$, than the typical energy density it measures during inflation. However, it is much larger, about a factor $\sim (2GM)^2 H/t_\sigma$, than the Hawking radiation of a black hole of mass M. After crossing the past event horizon (the white hole horizon) the parent escapes towards i_A^+. At that time, it observes a constant flux $\Phi_A = \rho_{\rm bh}$ emanating from the future event horizon of the black hole, corresponding to Hawking radiation at the expected temperature.

As for the energy, note that it satisfies the relation

$$\rho_A(\tau) = \Phi_A(\tau) - \frac{1}{54\pi\tau^2}\,, \tag{4.4}$$

where the last term is just an effect of the expansion of the universe. This implies that when the parent reaches i_A^+, it measures an energy density with same value as the flux. A more interesting behaviour happens at $\tau = t_*$. For large supercritical walls, with $t_\sigma \gg H^{-1}$ and $R_* \gg H^{-1}$, the energy density is approximately

$$\rho_A(t_*) \approx \rho_{\rm dS} + \frac{H}{4\pi t_\sigma}\,, \tag{4.5}$$

where the last term corresponds to the effect of the domain wall. The pressure is related to the energy density by the equation of state

$$\rho_A(\tau) - p_A(\tau) = \frac{1}{54\pi\tau^2}\,. \tag{4.6}$$

The difference only depends on the trace of the energy-momentum tensor, which is proportional to the Ricci scalar. At i_A^+, the trace term vanishes and the pressure tends to equate the energy density as it in the case of radiation in 1+1 dimensions. At the moment just after the end of inflation, for $t_\sigma \gg H^{-1}$ and $R_* \gg H^{-1}$, the pressure goes like

$$p_A(t_*) \approx 2\rho_{\rm dS} + \frac{H}{4\pi t_\sigma} \tag{4.7}$$

In Figure 4.2 the measurements of the parent along its history are depicted as a dark blue line.

Observer B (The Explorer)

The second observer is a mirror version of the parent. This one ventures across the wormhole into the baby universe, while remaining this side of the domain wall. From

one side, the explorer is exposed to fluxes which may emanate from the future event horizon facing the baby universe, and from the opposite side it is exposed to the possible effect of the domain wall. The fate of this observer is to reach future infinity i_B^+, as it is depicted in Figure 4.1 by the green line. Its trajectory can be parametrized as $x_B^\mu = (U_B(\tau), V_B(\tau))$, where $U_B(\tau)$ and $V_B(\tau)$ are given by combining Eqs. (1.22) with Eqs. (1.30) and (1.29) (the T coordinate in this case is negative).
Similar to the parent, the explorer observes a constant flux $\Phi_B(\infty) = -\rho_{\rm bh}$ when it reaches i_B^+. This correponds to radiation coming from the future event horizon facing the baby universe, corresponding to Hawking radiation at the expected temperature. At the time $\tau = t_*$, this observers measures a different flux than the parent due to the asymmetry of the spacetime. In the limit where $R_* \gg H^{-1}$ and $t_\sigma \gg H^{-1}$ it approximately goes to the value

$$\Phi_B(t_*) \approx \frac{1}{4\pi}\frac{H}{t_\sigma} - \frac{1}{2\pi}\frac{H}{R_*} \tag{4.8}$$

If the domain wall is large, $R_* \gg t_\sigma$, then the parent and the explorer measure the same flux.

As for the energy density and pressure, the explorer measures the same as the parent. The evolution of these quantities are shown as a green curve in Figure 4.2.

Observer C (The Child)

Had the domain wall not pushed them appart, this observer would have remained close to observer A. Its trajectory tracks the dust particle, from the Schwarzschild side, moving along the edge of the expanding ball of dust in the baby universe. Its path is shown with a cyan line in Figure 4.1, ending at a different future infinity i_C^+.

At the time $\tau = t_*$, the child measures a flux towards the expanding ball of dust with the same magnitude as the one measured by the parent. They are unaware that their experience in the future will be completely different. Actually, the communication between the child and the parent turns out to be very difficult because of the small window of time the child has to send signals to the parent.

Just after the horizon crossing, $\tau \approx \tau_d + \mathcal{O}(R_*^{-1}H^{-2})$ with $\tau_d = 4GM/3$[2], it measures a transient outgoing flux which is a remnant of the one expelled at t_* towards the expanding ball of dust. When the child reaches i_C^+, unlike the previous observers, does not measure any flux at all.

As for the energy and pressure, before the horizon crossing the observer measures the same energy and pressure as the parent and the explorer. Just after the horizon

[2]This corresponds to the intersection between the null geodesic $X^-_{\text{int},\circ}$ and the child's trajectory.

crossing, a discontinuity appears for both pressure and energy. Ultimately, they decay to zero as the child approaches i_C^+.

We show in Figure 4.2 the evolution of the flux, energy density and pressure measured by the child observer.

Observer E (The Forth One)

The forth observer does not move with escape velocity and at a finite time it enters the black hole region. Eventually, it hits the singularity. It corresponds to an observer moving with zero Kruskal radial coordinate. More precisely, its trajectory is characterized by $x_E^\mu = (U_E(\tau), V_E(\tau))$,where $U_E(\tau) = V_E(\tau) = T_K(\tau)$, T_K is the Kruskal time coordinate. The expression for $T_K(\tau)$ is given implicity by[3]

$$\frac{\tau}{2GM} = \text{sign}(T_K)\left(\sqrt{\frac{R_E}{2GM}\left(1-\frac{R_E}{2GM}\right)} + \sin^{-1}\left(\sqrt{1-\frac{R_E}{2GM}}\right)\right) + \frac{\pi}{2} \tag{4.10}$$

with $R_E = 2GM\,(1 + W(-T_K^2/e))$. The forth observer enters the black hole at a time $\tau_{\rm k} = \pi GM$ and reaches the singularity at $\tau_{\rm s} = 2\pi GM$.

As shown in Figure 4.2, before the observer enters the black hole, the measured flux, energy density and pressure are quite similar to the ones measured by the parent and the explorer observers. Once in the black hole, the flux decays to zero at a higher rate.

As for the energy density and pressure, they satisfy the equation of state

$$\rho_E(\tau) - p_E(\tau) = -\frac{GM}{6\pi R_E^3}\,. \tag{4.11}$$

where the last term is the trace of the energy-momentum tensor, which is proportional to the Ricci scalar. As the forth observer approaches the singularity at $R = 0$, both energy density and pressure diverge. This is because their evolution is dominated by the curvature term, which scales as $R_E(\tau)^{-3} \sim (2\pi GM - \tau)^{-2}$.

Observer W (The Wall)

The last observer is the one who rides the wall. In this sense, it describes the same trajectory as the domain wall Eq. (1.23), represented in Figure 3.1 by the brown line. Unlike the rest of observers, this one ends up at null infinity $\mathcal{I}^+$.

[3] It follows from solving the differential equation

$$\frac{dT_K}{d\tau} = \frac{e^{\frac{R_E}{2GM}}\sqrt{\frac{R_E}{2GM}}}{4GM}\,. \tag{4.9}$$

As it can be seen in Figure 4.2, the flux, energy density and pressure meaured by this observer decay at much faster rate than the ones measured by the rest of observers. After the time $\tau = t_\sigma$, the decay rate is exponentially fast. This decay is dominated by the Ricci scalar of the Schwarzschild spacetime, which as written in Eq. (4.11), scales like R^{-3}, with R given by the solution of Eq. (1.18a). For times larger than t_σ, $R(\tau) \sim e^{\tau/t_\sigma}$, so the flux, energy density and pressure vanish exponentially fast with rate t_σ^{-1}.

The wall observer crosses the horizon at a time[4] of

$$\tau_{\rm w} \approx \frac{2}{3} t_\sigma \log\left(\frac{4GM}{t_\sigma}\right) . \tag{4.12}$$

After the horizon crossing, the observer practically does not detect anything. It just moves towards null infinity, leaving everything behind.

[4] In this case we can use the approximate solution Eq. (1.26). The constant C is set to $(Ht_\sigma)^{-1} - \operatorname{arcsinh}\left((Ht_\sigma)^{-1}\right)$ so that $R(t_*) = R_*$. Also, the expression in Eq. (4.12) assumes $R_* \gg t_\sigma$.

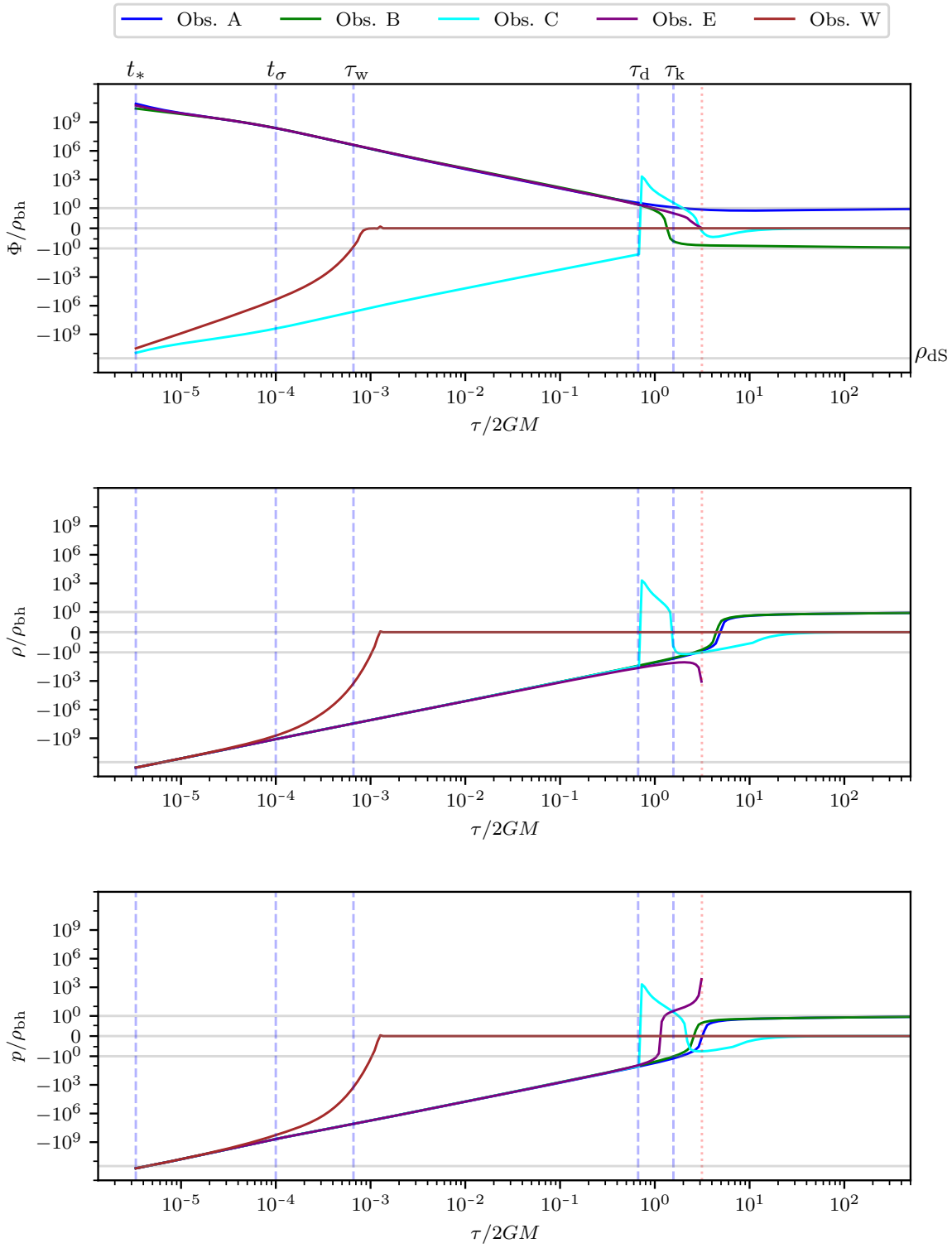

Figure 4.2: From top to bottom: we show the flux $\Phi(\tau)$, energy density $\rho(\tau)$ and pressure $p(\tau)$ in units of $\rho_{\rm bh}$, measured by several types of observers as a function of proper time τ. The lines $\tau_{\rm w}, \tau_{\rm d}$ and $\tau_{\rm k}$ respresent the moment when observers W, A to C and E cross the horizon, respectively. The red dotted line correspond to the time when observer E hits the singularity. The horizontal light gray lines correspond to $\pm\rho_{\rm bh}$ and $\rho_{\rm dS}$.

Part II

Primordial black holes and gravitational waves

Chapter

5 Primordial black holes

Fifty years ago, it was proposed that rare curvature perturbations in the early Universe could lead to the formation of primordial black holes (PBH) during the radiation era [54, 55]. With the recent detection of gravitational waves (GWs) from merging black hole binary systems, there is growing interest in the possibility that PBHs could be a viable component of Dark Matter (DM).

Various mechanisms have been proposed for the formation of PBHs, either as a result of large inhomogeneities in the aftermath of phase transitons, or as the result of primordial perturbations of inflationary origin. One possible scenario is based on an enhancement of the curvature perturbations at the lengthscale corresponding to the PBH horizon. This can be caused by a specific feature in the inflationary potential, such as an inflection point or a small barrier on the slope of the potential, that results in a transient departure from slow roll, which leads to the required enhancement at that scale. Another mechansim is the collapse of relic topological defects, such as false vacuum bubbles or domain walls produced by the breaking of a discrete symmetry.

Understanding the formation mechanisms of PBHs not only enables us to make accurate predictions about their statistical properties but also has important observational consequences. A precise estimate the merger rate of PBH binaries provides valuable insights into the abundance and dynamics of PBH populations, allowing us to constrain the formation scenarios. Moreover, the indirect detection of gravitational waves from PBH mergers provides another method for probing their existence. While the direct detection of individual PBHs remains challenging, a stochastic background of gravitational waves (SBGW) emmited by numerous mergers may be detectable. This background carries valuable information about the population of PBH binaries, including their mass distribution, merger rates, and formation mechanisms.

The structure of this chapter is the following. In Sections 5.1 and 5.2 we provide a brief overview of the formation of PBH binaries and the subsequent merging process. In Section 5.3 we delve into the calculation of the stochastic background of gravitational waves resulting from the merger events of PBH binaries. This will serve as a groundwork

for Chapter 6. In this chapter and the subsequent one, we will adopt the use of natural units where $G = c = 1$.

5.1 Formation of PBH binaries

In this section, we consdier the formation of PBH binaries [56, 57]. Our focus is on two randomly picked black holes that have been formed in deep in the radiation era. Let us denote their respective masses as M_1 and M_2, and consider the comoving distance x between them.

A binary will form when the two black hole system decouples from the Hubble flow. The time of decoupling (i.e the formation time of the binary), denoted by $t_{\rm dec}$, is related to the comoving distance between the black holes by the following argument. The two-body system of physical size $a(t)x$ will decouple when the energy density created by a binary at such distance becomes larger than the background energy density, that is

$$\frac{M_T}{\left(a\left(t_{\rm dec}\right)x\right)^3} \gtrsim \rho_{\rm back}(t_{\rm dec})\,. \tag{5.1}$$

where $M_T = M_1 + M_2$ is the total mass of the system. In order for this to be satisfied, the decoupling has to happen in radiation dominated era, since $\rho_{\rm back} \approx \rho_{\rm eq}/(2a^4(t))$[1]. This implies that[2]

$$x \lesssim \left(\frac{M_T}{2\rho_{\rm eq}}\right)^{\frac{1}{3}} a^{\frac{1}{3}}(t_{\rm dec})\,, \tag{5.2}$$

The saturation of Eq. (5.2) implicitly defines the decoupling time $t_{\rm dec}$ by means of the comoving distance x. Also, the relation (5.2) inherits an important consideration, and has to do with the maximum size of a binary that participates in mergers at $t_{\rm obs}$, which will be denoted by $x_{\rm max}$. One can see that this maximum size will be given by the latest time a binary can decouple. Once Eq. (5.2) is satisfied, a binary will form.

This new system can be described basically by four parameters: the masses of the black holes[3], the initial size of the binary corresponding to the physical distance $r_x = a(t_{\rm dec})x$ between the black holes at the moment of decoupling. Alternative we can use the comoving distance which, using condition Eq. (5.2) is related to r_x by

$$r_x \simeq x^4\left(\frac{2\rho_{\rm eq}}{M_T}\right) \tag{5.3}$$

[1] Here we choose the scale factor $a(t) = 1$ at matter-radiation equality, which is a standard convention in this context.

[2] Note that if the mass distribution for the PBH distribution is not too broad, we may assume $M_T/2 \approx \overline{M}$, with $\overline{M}$ the mean mass of the black holes.

[3] The evolution and dynamcs of the binary is determined not by the masses individualy but by a combination of them. More specifically, on the total mass $M_T = M_1 + M_2$, and on the so-=-called reduced mass ratio $\mu = M_1M_2/M_T$.

Finally, since the binary is immersed in a local tidal field, created by other PBHs and density perturbations, this will exert a torque on the binary providing it with some orbital angular momentum, This orbital angular momentum will prevent the head-on collision of the PBHs, and make the elliptical orbit have some excentricity. The excentricty e and the orbital angular momentum are related by $e = \sqrt{1-j^2}$ where $j = \ell/\sqrt{GMr_x}$, with ℓ the orbital angular momentum per unit reduced mass.

5.2 Merger rate of PBH binaries

In this section we shall derive an expression for the merger rate of PBHs binaries [57]. For simplicity, let us assume a monochromatic mass distribution of PBHs. Let us denote by $\mathrm{d}N_{\rm two}(x,j)$ the comoving number density of configuration of binaries with comoving size within $(x, x+\mathrm{d}x)$ and angular momentum within $(j, j+\mathrm{d}j)$. Only a fraction of such binaries will merge at the present epoch. First, the number of binaries that will be produced are the configurations satifying Eq. (5.2). Also, if we want these binaries to merge at some time $t_{\rm obs}$ we need to impose a constraint on x and j such that the merging time $t_{\rm m}$ coicides with this observation time. Therefore the number of binaries merged per observed time and per comoving volume is just

$$\frac{\mathrm{d}R(t_{\rm obs})}{\mathrm{d}t_{\rm obs}} = \int\int \mathrm{d}N_{\rm two}(x,j)\delta(t_{\rm obs}-t_{\rm m}(j,x))\Theta\left(x_{\rm max}-x\right) \tag{5.4}$$

This defines the merger rate per comoving time at time $t_{\rm obs}$. We can further write $\mathrm{d}N_{\rm two}(x,j)$ as

$$\mathrm{d}N_{\rm two}(x,j) = \left(\frac{n_{\rm PBH}}{2}\right)\ \mathrm{d}x\mathrm{d}jP_J(j,x) \tag{5.5}$$

with $n_{\rm PBH}/2$ is the number density of binaries (the two avoids double counting). We also introduce the probability density $P_J(j,x)\mathrm{d}x\mathrm{d}j$ to find two randomly selected PBHs with j and x. Inserting Eq. (5.5) in Eq. (5.4) we find

$$\mathrm{d}R(t_{\rm obs}) = \frac{n_{\rm PBH}}{2}\int \mathrm{d}x\mathrm{d}j\ P_J(j,x)\delta(t_{\rm obs}-t_{\rm m}(j,x))\Theta\left(x-x_{\rm max}\right)\ . \tag{5.6}$$

Obtaining an expression for the density distribution $P_J(j,x)$ is not easy, since as we shall see in the next section, it depends fully on the PBHs spatial distribution. In general, the angular momentum induced to binary will come from the tidal field created by cosmological perturbations and its neighbouring black holes $\vec{j} = \vec{j}_{\rm CP} + \vec{j}_{\rm PBH}$[4]. We

[4]The expression for $\vec{j}_{\rm PBH}$ is given by

$$\vec{j}_{\rm PBH} = \sum_{p=2}^{N}\vec{j}_p\,, \quad \vec{j}_{=}\frac{3}{2}\frac{x^3}{x_p^3}(\hat{x}\cdot\hat{x}_p)(\hat{x}\times\hat{x}_p) \tag{5.7}$$

with $\vec{x}$ is the vector size of the binary, $\vec{y}_p$ is the distance to the p-neighbour and the hat means unitary vector.

will neglect the cosmological perturbations and concentrate only on the effect of the neighbouring PBHs [31, 58]. Since $\vec{j}_{\rm PBH}$ is a function of all the distances between black holes, we can write the distribution $P_J(j,x)$ as a function of the so-called N-neighbour distribution which we denote by $Q_N(x_1,\ldots,x_N;x_0)$

$$P_J(j,x) = \int {\rm d}x_2 \ldots {\rm d}x_N Q_N(x,x_2,\ldots,x_N)\delta(j - j(x,x_2,\ldots,x_N)) \tag{5.8}$$

The distribution $Q_N(x_1,\ldots,x_N;x_0)$ tells us the probability of, given a PBH at position x_0, which by homogeneity we can choose it to be the origin, having the first negihbour at distance x_1, the second one at x_2, etc. This quantity only depends on the (comoving) spatial distribution of the PBHs and is specified by the mechanism of formation. The computation of Eq. (5.8) is unfeasible in general, and only in some cases can be computed analytically, for instance if the case where the PBHs are spatially uncorrelated. Inserting Eq. (5.8) into Eq. (5.6), we write the merger rate density as

$${\rm d}R(t_{\rm obs}) = \frac{n_{\rm PBH}}{2}\int {\rm d}x\ {\rm d}\vec{x}_i\ Q_N(x,\vec{y})\delta(t_{\rm obs} - t_{\rm m}(j(x,\vec{y}),x))\Theta\left(x_{\rm max}-x\right) \tag{5.9}$$

with $\vec{y} = (y_2,\ldots,y_N)$. The computation of Eq. (5.9) can be simplified a bit if we assume that the main contribution to the torque comes from the nearest PBH to the binary, and so $j(x,y) \approx (x/y_2)^3$. In this case, the delta function in Eq. (5.9) eliminates one integral and together with the condition $x < x_{\rm max}$, introduces a minimum comoving distance participating in a merger at time $t_{\rm obs}$, $x_{\rm min}(t_{\rm obs})$. Thus, Eq. (5.9) reduces to

$${\rm d}R(t_{\rm obs}) = \frac{n_{\rm PBH}}{2}\int_{x_{\rm min}}^{x_{\rm max}} {\rm d}x\ Q_2(x,\tilde{y}(x,t_{\rm obs}))\left|\frac{d\tilde{y}(x,t_{\rm obs})}{dt_{\rm obs}}\right| \tag{5.10}$$

where $\tilde{y}(x,t_{\rm obs})$ is given by $t_{\rm obs} = t_{\rm m}(x,y)$

5.2.1 The coalesence time of a binary

The only ingredient left n the calculation of Eq. (5.9) is the coalesence time of the binary as a function of the size of the binary and its angular momentum.

There are two effects that might play an important role in the case of early time mergers, in particular for those happening before matter radiation equality. The first one has to do with with the fact that the so-called Peters time does not provide an accurate description for very eccentric mergers. This approximations tells us that the time to collapse from the moment of decoupling is given by [59]

$$t_{\rm p}(j,r_x) = \frac{3}{85}\frac{r_x^4}{\eta M_T^3}j^7\ , \tag{5.11}$$

where $\eta = M_1M_2/M_T^2 = \mu/M_T$, is the so-called symmetric mass ratio. While this is a good description for binaries with small eccentricities, it fails for very eccentric orbits. A

binary that decouples at time $t_{\rm dec}$ and has a very large eccentricity might merge in 'no time' according to Peters formula. Of course this is incorrect, since the time of merger is at least equal to the free falling time, $t_{\rm ff}$, which is given by

$$t_{\rm ff}(r_x) = \left(\frac{r_x^3}{M_T}\right)^{\frac{1}{2}} . \tag{5.12}$$

Therefore, Peters approximation will fail for configurations having $t_{\rm p} < t_{\rm ff}$. Taking into account this consideration we can write the merging time $t_{\rm m}$ in which a binary merges

$$t_{\rm m}(j, r_x) - t_{\rm dec}(r_x) = t_{\rm p}(j, r_x) + t_{\rm ff}(r_x) . \tag{5.13}$$

As we will see in the next subsection, the addition of this *free falling* time will have relevant consequences for early mergers.

The merger rate for a Poissonian distribution

Here we show the merger rate for a Poissionan distributed population of PBHs. We assume that the angular momentum is only induced by the closest black hole to the binary, so we can use calculate the merger rate as in Eq. (5.10). In this case,

$$Q_2(x, y) = 16\pi^2 n^2 x^2 y^2 \exp(-\frac{4\pi n}{3} y^3)\Theta(y - x) , \tag{5.14}$$

The limit $x_{\rm max}$ in Eq. (5.10) is determined as follows. Since binaries can only decouple in radiation dominated era, for systems merging at $t_{\rm obs} > t_{\rm eq} + t_{\rm ff}$, the maximum size a binary can have is a constant given by

$$x_{\rm max} = \left(\frac{M_T}{2\rho_{\rm eq}}\right)^{\frac{1}{3}} \ , \ t_{\rm obs} > t_{\rm eq} + t_{\rm ff} \tag{5.15}$$

For mergers happening before that time, the latest time it can decouple and merge at time $t_{\rm obs}$ is $t_{\rm dec}^{\rm max} = t_{\rm obs} - t_{\rm ff}$. After some calculations it can be found that

$$x_{\rm max}(t_{\rm obs}) \approx \left(\frac{M_T}{2\rho_{\rm eq}}\right)^{\frac{1}{3}} \left[{t_{\rm obs}}^2 \rho_{\rm eq}\right]^{1/12} \ , \ t_{\rm obs} < t_{\rm eq} + t_{\rm ff} \tag{5.16}$$

which is explicitly time dependent.

The last piece that we need to determine is $x_{\rm min}$, the minimum comoving distance participating in a merger at time $t_{\rm obs}$. This is given by the distance such that a circular merger (the configuration having the largest merging time) with such semi-axis merges at time $t_{\rm obs}$. This implies that all binaries separated by a distance $x < x_{\rm min}$ would have merged in a time $t < t_{\rm obs}$, for all the possible eccentricities. From inverting Eq. (5.13) and using $x < x_{\rm max}$, this is approximately given by

$$x_{\rm min}(t_{\rm obs}) = \left(\frac{85 M_T^3 t_{\rm obs}}{12 x_{\rm max}^4}\right)^{1/16} x_{\rm max} , \tag{5.17}$$

with here $x_{\rm max}$ given as in Eq. (5.15). We can then perform the integral (5.10), considering $x_{\rm min}$ as given in Eq. (5.17) and $x_{\rm max}$ as given by either (5.15) or (5.16) depending on whether the observed time is after o before matter radiation equality. The function $\tilde{y}(x, t_{\rm obs})$ in Eq. (5.10) is given by inverting Eq. (5.13) [60]

$$\tilde{y}(x, t_{\rm obs}) = \left(\frac{12}{85 M_T^3 (f^{\frac{1}{3}}\bar{x})^{12}}\right)^{1/21} \frac{x^{37/21}}{\left(t_{\rm obs} - t_{\rm dec}(x) - t_{\rm ff}(x)\right)^{1/21}} \tag{5.18}$$

Note that this function diverges at $x^* = x_{\rm min}(t_{\rm obs})$, which defines the *free falling* configuration $(x, y) = (x^*, \infty)$. Let us now consider, for a fixed observation time $t_{\rm obs}$, binaries of sizes up to $x' = \lambda x^*(t_{\rm obs})$, for some $\lambda \lesssim 1$. This takes into account configurations with finite y, so we avoid the *free fall* configuration. The extremal configuration $(x', y(x'))$ gives us, for the Peters, free fall and decoupling time

$$t_{\rm p} = (1 - \lambda^6) t_{\rm obs}\,, \quad t_{\rm ff} + t_{\rm dec} \approx \lambda^6 t_{\rm obs} \tag{5.19}$$

So, for $\lambda > 0.9$, the mergers will be dominated by the free fall time. In Fig. 5.1 we show the resulting merger rate. Before matter-radiation equality, the merger rate follows the typical scaling of the Poissonian case, with $R(z) \propto (1+z)^{1.4}$. However, after matter-radiation equality, at high redshifts, the merger rate increases as $R(z) \propto 1 + z$, mainly due to the contribution of the *free falling* orbits. When considering only the contribution of mergers involving binaries with a torque, such as those within a size range up to $0.9x^*$, the merger rate drops as $R(z) \propto (1+z)^{-1/2}$ as a result the shrinking maximum comoving distance allowed for mergers, Eq. (5.16). As shown in Figure 5.1, even when considering binaries within the range of sizes from $0.9x$ to x^*, the merger rate still exhibits a decreasing trend with redshift, although it becomes more apparent at larger redshifts.

5.3 Stochastic background of gravitational waves

The most recent catalog from the LIGO/Virgo experiment has reported direct detections of binary black hole mergers up to a redshift of approximately $z \simeq 1$. However, these detectors are not only capable of detecting these mergers directly but also have the potential to indirectly observe merger events that occurred at much larger redshifts through their sensitivity to the stochastic gravitational wave background generated by past mergers.

The typical merger process for such a configuration consists of three stages: the inspiral phase, the merger phase, and the ringdown phase. The inspiral phase begins shortly after the formation of the binary. If the initial size of the binary is large enough, the two black holes will start moving toward each other in an elliptical orbit, gradually losing energy during this phase. The post-Newtonian formalism is employed

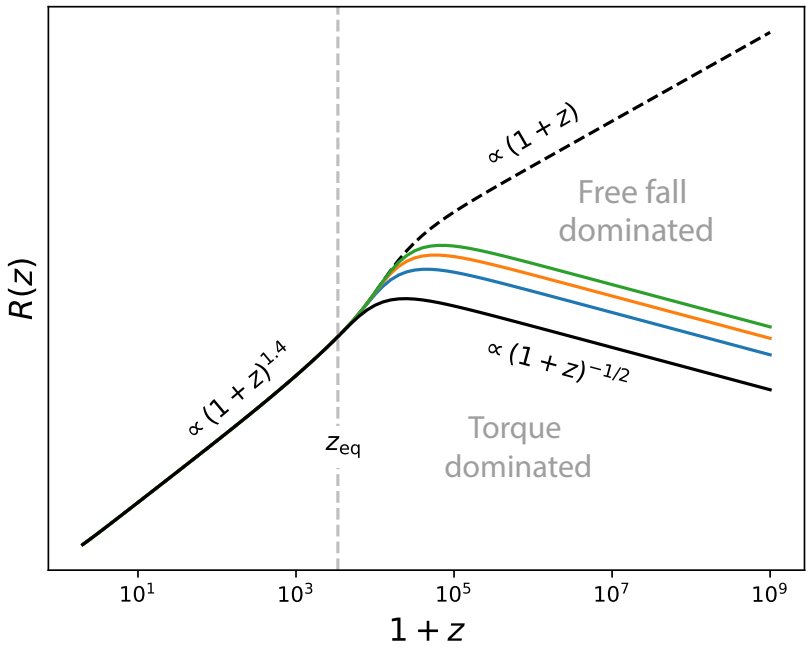

Figure 5.1: Merger rate for a Poissonian initial distribution. Before $z = z_{\rm eq}$, the rate follows the typical scaling $\propto (1+z)^{1.4}$. After $z = z_{\rm eq}$, the merger rate increases because of the contribution of the free falling orbits. However, if most of the mergers are dominated by $t_{\rm p}$, the merger rate drops because of the shrinking of $x_{\rm max}$. The dashed black line corresponds to the merger rate accounting for binaries of all sizes. The solid lines correspond to merger rates accounting for binaries of size up to λx^*, for $\lambda = 0.9, 0.99, 0.999$ and 0.9999 corresponding to the black, blue, orange and green colors.

to model this phase, with the requirement that the distance between the black holes is large enough[5]. For closer distances, where the gravitational field becomes stronger and relativistic effects become significant, the solution requires the use of Numerical Relativity or an effective one-body (EOB) approach. This stage encompasses the actual merger of the binary. The ringdown phase occurs after the merger has occurred. The computation of the ringdown phase can be performed by using numerical relativity simulations, perturbation theory, or EOB models. In Figure 5.2, we show ther typical strain of GWs.

During the process of merger, a significant amount of energy is released in the form of gravitational waves. The collective sum of these signals results in a stochastic background of gravitational waves. The magnitude of such stochastic background $\Omega_{\rm GW}(\nu_{\rm obs})$ is reported in terms of its energy density per logarithmic frequency interval

[5]To apply the post-Newtonian formalism we require the distance between the PBH to be $r \geq 10GM_T$, when the velocity of the rotating system $v^2 \sim GM_T/r$ is not relativistic and the post-Newtonian expansion doesn't fall apart. At closer distances, the gravitational field gets stronger and we need Numerical Relativity to solve it

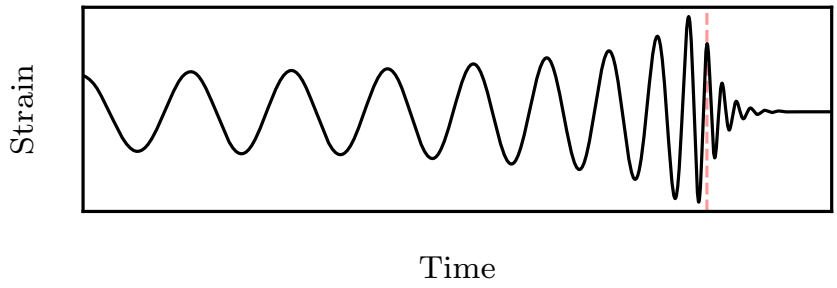

Figure 5.2: Typical waveform of the GW spectrum released by a PBH binary. The red dashed line shows the moment when the binary has size $\sim 2GM_T$

$\rho_{\rm GW}(\nu_{\rm obs})$ with respect to the critical density of the universe today,

$$\Omega_{\rm GW}(\nu_{\rm obs}) \equiv \frac{1}{\rho_c}\frac{{\rm d}\rho_{\rm GW}}{{\rm d}\log\nu_{\rm obs}}\,, \quad \rho_c = \frac{3H_0^2}{8\pi G} \tag{5.20}$$

where $H_0 \approx 67.7$ km s^{-1} Mpc^{-1} is the Hubble constant today, and $\nu_{\rm obs}$ is the frequency of the gravitational waves observed today. The total energy of gravitational radiation will be given by the sum of all energy released by the mergers at all redshifts. It can be checked that the contribution coming from early formed binaries can be expressed as (see e.g. [29])

$$\Omega_{\rm GW}(\nu) = \frac{\nu_{\rm obs}}{\rho_c H_0}\int_0^{z_{\rm max}} {\rm d}z \frac{R(z)}{(1+z)E(z)}\frac{dE_{\rm GW}}{d\nu_{\rm s}}(\nu_{\rm s}) \tag{5.21}$$

Here ${\rm d}E_{\rm GW}/{\rm d}\nu_s$ is the energy emmitted in gravitational waves during a single merger event, and ν_s is the frequency in the source frame, related to the observed frequency as $\nu_{\rm s} = (1+z)\nu_{\rm obs}$. The function $R_{\rm PBH}(z)$ is the merger rate in Eq. (5.9) with $t_{\rm obs} = t_{\rm obs}(z)$, and $E(z) \equiv H(z)/H_0 = [\Omega_r(1+z)^4 + \Omega_m(1+z)^3 + \Omega_\Lambda]^{1/2}$. Finally, the upper limit $z_{\rm max}$ corresponds to the maximum redshift at which we include mergers in our analysis. In principle, we should consider all possible mergers, including those at extremely high redshifts. For example, in the case of black holes with masses around $10^2\,M_\odot$, the maximum redshift could reach approximately $z \sim 10^{12}$, corresponding to the time when these black holes were formed. However, in practice, the inclusion of such high-redshift mergers is often limited by observational constraints and the capabilities of the detectors. We will discuss this further in the next chapter.

The energy released as GWs ${\rm d}E_{\rm GW}/{\rm d}\nu_s$ can be deduced from the waveforms. This has been modeled for the inspiral, merger, and ringdown phases, and fitted through numerical simulations [61, 62]. For non-precessing binaries, as it is the case for solar

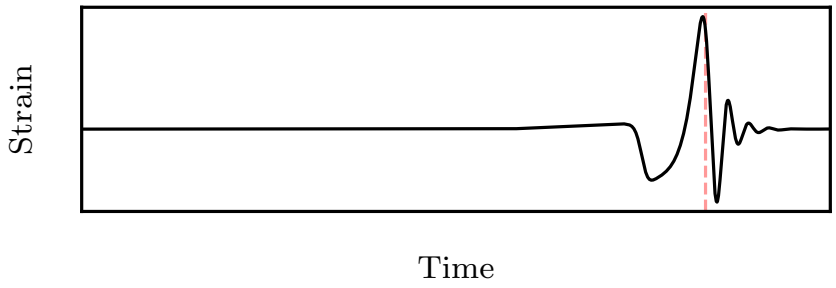

Figure 5.3: Typical waveform of the GW spectrum released by a merger of highly excentric binary. The red dashed line shows the moment at which the binary has size $\sim 2GM$. We thank Tomás Andrade for providing us this plot.

mass PBHs [63–65], it takes the following form (see also [66, 67])

$$\frac{dE_{\rm GW}}{d\nu_s}(\nu_s) = \frac{\pi^{2/3} M_c^{5/3}}{3} \begin{cases} \nu_s^{-1/3} & \text{for } \nu_s < \nu_1 \\ \omega_1 \nu_s^{2/3} & \text{for } \nu_1 \leq \nu_s < \nu_2 \\ \omega_2 \frac{\sigma^4 \nu_s^2}{\left(\sigma^2 + 4(\nu_s - \nu_2)^2\right)^2} & \text{for } \nu_2 \leq \nu_s < \nu_3 \\ 0 & \text{for } \nu_3 \leq \nu_s \end{cases} \tag{5.22}$$

where $\nu_i \equiv (\nu_1, \nu_2, \sigma, \nu_3) = (a_i \eta^2 + b_i \eta + c_i)/(\pi M)$, $M = m_1 + m_2$ is the total mass, M_c is the chirp mass ($M_c^{5/3} = m_1 m_2 M^{-1/3}$), and $\eta = m_1 m_2 M^{-2}$ is the symmetric mass ratio. The parameters a_i, b_i and c_i can be found in [61], and (ω_1, ω_2) are chosen such that the spectrum is continuous. In (5.22) the three regimes corresponds, towards larger frequencies, to the inspiral, merging and ringdown phases, and for $30\,M_\odot$ they correspond to $\nu_i = (135, 271, 79, 387)$ Hz.

The derivation of Eq. (5.22) assumed that the black holes started from an infinite distance and underwent an elliptical orbit, beginning with the inspiral phase. However, in the case of early mergers, the black holes start much closer than a period and are likely to collide in an almost head-on manner. In Figure 5.3 we show the typical waveform of GW for an almost head on merger. In these scenarios, one could argue that there is no significant inspiral phase, and since most of the energy is released during this phase, the spectrum of the stochastic gravitational wave background might be negligible. Nevertheless, due to the large number of mergers occurring during early epochs, it is possible that these events still contribute significantly, or at least non-negligibly, to the overall spectrum of the stochastic gravitational wave background. This will be studied in the future, since further numerical simulations are required to confirm these assumptions.

Chapter

6 Constraining the merger rate history of PBH binaries

In this chapter we shall discuss how current and future experiments can constrain the merger history of PBH binaries. The direct detection of 63 binary black hole (BBH) mergers from redshifts $z \simeq 0.1$ up to $z \simeq 0.8$ in the GWTC-3 catalog of LIGO/Virgo [24] provides valuable information for constraining the merger rate density of black hole binaries as a function of redshift. In particular, for a merger following a power law distribution

$$\frac{dN_{\rm merg}}{dtdV} \equiv R(z) = R_0(1+z)^{\alpha}, \tag{6.1}$$

the factor α is found to be $2.7^{+1.8}_{-1.9}$ [24] for a present merger rate $R_0 = 9-35$ Gpc^{-3}yr^{-1}. These constraints are evidently only sensitive up to the largest redshift at which the merger of a certain binary might be detectable. This is the so-called horizon distance, and for BBH of $\sim 30M_{\odot}$, $z_{\rm hor} \simeq 1$ for LIGO/Virgo. The law distribution in Eq. (6.1) agrees with a population of Poissionian distributed PBHs. This disribution can emerge when the underlying field producing the black holes follows a Gaussian dstribution with a peaky power spectrum at the scale of the size of the PBH. However, non-Poissonian distributions can also lead to that power law at least for small redshift but change the scaling at large and until now unobserved redshifts.

Additionally, the detection of a stochastic background of gravitational waves sourced from past mergers provides a way to indirectly infer information about the merger rate at redshifts beyond the $z_{\rm hor}$. Although the stochastic background has not been detected yet, its absence has been used to constrain the abundance of BBHs [26–36]. Here, we will focus on using this lack of observation of the stochastic background to contrain the merger rate.

In general, it is assumed that the merger rate histories of PBH binaries has either the form of a power law as in Eq. (6.1) with a positive exponent, or by a power law up to a certain redshift and later decay. These two families of models roughly correspond to primordial and stellar black holes respectively. Either way, even assuming the form in Eq. (6.1), the determination exponent α is highly model depent. For instance, in the

case of PBH originating from an initial Poissonian distribution[1], it becomes possible to determine α of the merger in Eq. (6.1). For low abundances ($f_{\rm PBH} \lesssim 0.01$) and small redshifts ($z < 1$), the exponent is found to be $\alpha = 1.1$. However, for higher redshifts, α takes a value of $\alpha = 1.4$. For large abundances, the behaviour of the merger rate with redshift remains uncertain, since N-body effects need to be taken into account[2] [32, 37].

Despite these dificulties, some interesting results have been obtained in determining the merger rate for some families of clustered distributions, with the use of numerical simulations [38, 39]. For example, black hole binaries merging inside globular clusters can exhibit $\alpha = 2.3^{+1.3}_{-1.0}$ [39]. Other studies focusing on non-Gaussian initial distributions of PBHs -but having neglected the effects of N-body disruption of binaries- have shown that the merger rate of PBH binaries can have a very complex dependence on redshift, in particular, with an interpolation of various slopes at intermediate redshifts [3]. These results are a clear motivation for exploring a larger set of BBHs merger histories. Given that there is still a large uncertainty in the class of allowed merger histories, we adopt a phenomenological approach and consider the consequences of a change in the slope of the merger rate at some particular redshift.

The structure of the chapter is as follows. In Section 6.1, we discuss the merger rate in clustered distributions of black holes, highlighting the diverse range of binary merger histories that can arise. This serves as a motivation to adopt a phenomenological model for the rate. The resulting stochastic background generated by this model is examined in Section 6.2. Finally, in Section 6.3 we present the constraints derived from the non-observation of the SBGW and calculate the minimum SNR ratio required for future experiments to detect it.

6.1 The model

As discussed in the introduction, there are reasons to explore a wide range of merger rate histories. Here, we present some examples of merger stories that may arise from different formation mechanisms, serving as motivation for the specific template we will use in the following sections. In particular, we will discuss the case of a clustered distribution of PBHs, as investigated in Ref. [3].

In Chapter 5, we discussed the merger rate for isolated black hole binaries, where the dominant torque contribution comes from the nearest black hole. To compute the rate Eq. (5.10), it is necessay to calculate the probability density $Q_2(x, y)$ of finding the first and second nearest neighbors at comoving distances x and y, respectively, given the presence of a black hole at the origin. This probability density, in principle, depends

[1] This distribution is the one resulting from seeds of curvature fluctuations that follow a Gaussian distribution with a peaked power spectrum at the scale of black holes [68–70]

[2] N-body effects may also play an important role for low abundances [58]

on the N-point correlation functions that dictate the probability of finding N PBHs. This is because when we aim to find only two black holes (or any number) within a specific volume, we must account for the probability of not finding $N-2$ black holes within that volume. Consequently, determining this probability in a general setting becomes more challenging. However, there are at least two simple cases where it can be easily determined, which are the Poissonian and the so-called "separable" case[3]. In such cases, the probability $Q_2(x,y)$ takes the form

$$Q_2(x,y) = 16\pi^2 x^2 y^2 n(x) n(y) \exp\left[-4\pi \int_{R_{\rm BH}}^{y} n(z) z^2 \mathrm{d}z\right] \Theta(y-x) \ . \tag{6.4}$$

where $n(r)$ is the local comoving number density of PBHs, given by

$$n(r) = \bar{n}(1 + g_2(r)) \tag{6.5}$$

where $\bar{n}$ is the mean comoving number density of PBHs. Usually the correlation function $g_2(r)$ decays to zero at large distances, so the comoving number densitiy inside an infinite volume coincides with $\bar{n}$. The case of a Poissonian distribution corresponds to $g_2(r) = 0$. The form of $g_2(r)$ is determined by the underlying physical mechanism governing the distribution of the black holes. To demonstrate its impact on the merger rate, we will examine a simple functional form where the correlation is approximately constant up to a scale k_L and then decays to zero for larger scales. In particular, we consider the following expression:

$$g_2(r, g_0, \alpha, k_L) = g_0 \frac{e^{\Theta(r,k_L,\alpha)} - 1}{e-1} \quad \text{with} \quad \Theta(r, k_L, \alpha) = \frac{1}{1 + e^{2\alpha \log(k_L^{-1} r)}} \ . \tag{6.6}$$

The correlation $g_2(r)$ is nearly constant with amplitude g_0 up to the scale $L = k_L^{-1}$, and then decays to zero with a slope determined by α.

In the left panel of Figure 6.1 we show the correlation function in Eq. (6.6), while in the right panel we see its resulting merger rate history. Note that if the correlation function varies around the scales $x_{\rm min}$ and $x_{\rm max}$, then we get important changes on the slope of the history, which in the examples presented, happen around redshifts 2 to 4. For completeness, in Figure 6.1 we also show the case of a Poissonian distribution.

[3] This is the particular case when the n-particle correlation functions g_N, defined as

$$g_n(r_1, .., r_{n-1}) \equiv \frac{P_n(r_1, .., r_{n-1})}{P_1^n} - 1 \tag{6.2}$$

follow the simple law [70, 71],

$$1 + g_n(r_1, .., r_{N-1}) = \prod_{i=1}^{n-1} (1 + g_2(r_i)) \ , \tag{6.3}$$

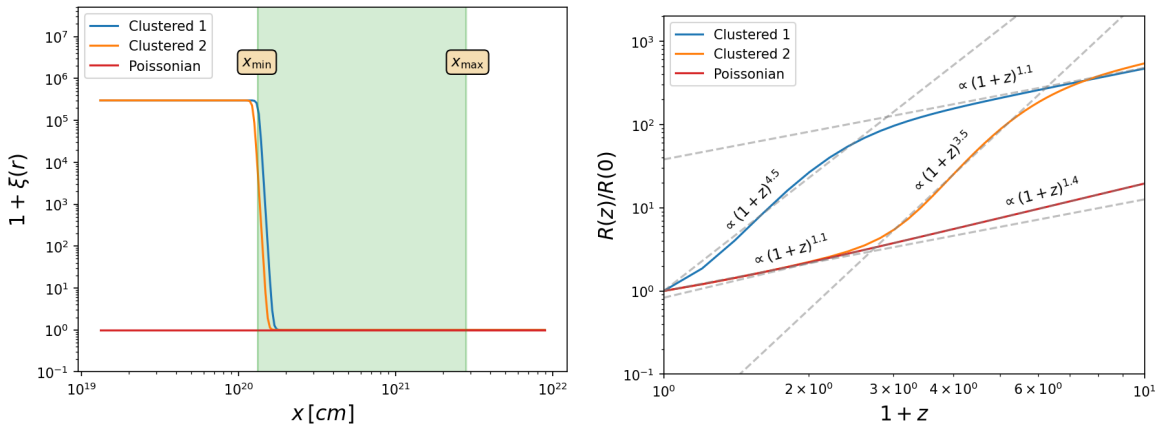

Figure 6.1: Left: Three different two-point correlation functions, as a function of comoving distance x, resulting in different merger rate histories. In blue and orange we show correlation functions given by Eq. (6.6), with parameters (g_0, α, k_L) given by $(3\times10^5, 30, 0.00887\,k_s)$ and $(3\times10^5, 30, 0.00959\,k_s)$ respectively. In red, we show the correlation function for a Poissonian distribution, where $g_2(r) = 0$. Here $1/k_s$ is the size of 30 solar mass PBHs. The comoving scales $x_{\rm min}$ and $x_{\rm max}$ are evaluated at $t = t_0$. **Right:** Normalized merger rates for the correlations shown in the left pannel.

The examples shown in the previous section serve as a motivation for consider a merger rate given by a broken power law model,

$$R(z) = \begin{cases} R_0(1+z)^\alpha & \text{for } z \le z_* \\ \mathcal{C}(1+z)^\beta & \text{for } z_* \le z \le z_{\rm max} \\ 0 & \text{for } z \ge z_{\rm max} \end{cases}, \tag{6.7}$$

where $\mathcal{C}$ is a constant chosen so that the merger rate is a continuous function. This template introduces several novel aspects compared to previous works. First, it allows positive values for both α and β, which, as demonstrated in the previous section, is feasible within a population of PBHs, and could also serve as a template for modeling the merger of astrophysical black hole binaries.

The parameter R_0 represents the number of mergers observed today, so according to the events dected by LIGO/Virgo, we will fix it to be around $9-35$ events/(Gpc^3 yr) [24]. Additionaly we will assume a monochromatic distribution of PBHs with mass around $M = 30M_\odot$.

Additionaly we will fix the parameter $z_{\rm max}$ to be $z_{\rm max} = z_{\rm eq}$, where $z_{\rm eq}$ is the redshift of matter-radiation equality. This specific cutoff is selected because we will consider only mergers that involve a circularly inspiraling phase at some point during their evolution. As shown in section 5.2.1 in the previous chapter, mergers that take place before

$z_{\rm eq}$ tend to be highly eccentric, and their contribution to the stochastic background may differ from what we will consider in our analysis (see section **??**). It should be noted that observable quantities relevant to frequencies within the range detectable by LIGO/Virgo are primarily sensitive to redshifts around $z \sim 10$. Therefore, the predictions made in this context should remain robust against any variations in the merger rate occurring at higher redshifts.

With R_0 and $z_{\rm max}$ set, the model is characterized by three parameters (α, β, z_*). In the following sections, we comment on additional constraints (section 6.3.1) and priors (section 6.3.2) on these parameters.

6.2 The stochastic background of past mergers

In this section, we describe the resulting stochastic background of gravitational waves resulting form the merger history defined in Eq. (6.7). As introduced in Chapter 5, given a merger rate history $R(z)$, the magnitude of the stochastic background $\Omega_{\rm GW}(\nu)$ is given in Eq. (5.21). Here, we will take the upper limit of the integral in Eq.(5.21) to be frequency dependent. In particular, we take $z_{\rm sup} = \min(z_{\rm max}, \nu_3/\nu - 1)$, where ν_3 is the cutoff frequency of the energy spectrum in Eq. (5.22). This way, for $z \geq z_{\rm sup}$, either the merger rate or the energy spectrum are zero.

Depicted in Figure 6.2 is the gravitational wave signal associated with the merger rate described by Eq. (6.7) across a range of parameter values (α, β, z_*). Additionally, it is shown the corresponding Ω_{GW} behavior derived from a Poissonian distribution of initial PBHs. In the Poissonian case, we observe the familiar $\nu^{2/3}$ scaling at lower frequencies followed by a posterior decay at higher frequencies. However, when considering other sets of parameters, the family of possible spectra expands.

In general, α and β set the overall amplitude at large and small frequencies respectively, and the frequency of the transition, ν_*, is controlled by z_* (more precisely $\nu_* = \nu_3/(1+z_*)$). For $\nu \geq \nu_*$, the only contribution to $\Omega_{\rm GW}$ comes from redshifts up to z_*. Therefore, the exponent α alone dictates the behaviour of $\Omega_{\rm GW}$ for this frequency range. On the other hand, for $\nu \leq \nu_*$, all redshifts $z \leq z_{\rm sup}$ contribute. For very small frequencies the main contribution comes from redshifts $z \geq z_*$, so it is the exponent β that governs the behaviour of $\Omega_{\rm GW}$. In principle, the infrared (IR) tail of the signal follows the scaling

$$\Omega^{\rm IR}_{\rm GW}(\nu, z_{\rm max} \to \infty) \sim \begin{cases} \nu^{2/3}, & \beta < \frac{7}{3} \\ \nu^{3-\beta}, & \beta \geq \frac{7}{3} \end{cases} \tag{6.8}$$

where the value $\beta_{\rm th} = 7/3$ comes from the fact that the integral in Eq.(5.21) does not converge at large redshifts for $\beta > \beta_{\rm th}$. However, in our model we do not see this scaling, due to the cutoff of the merger rate at $z_{\rm max} = z_{\rm eq}$. Since the signal is however tending to

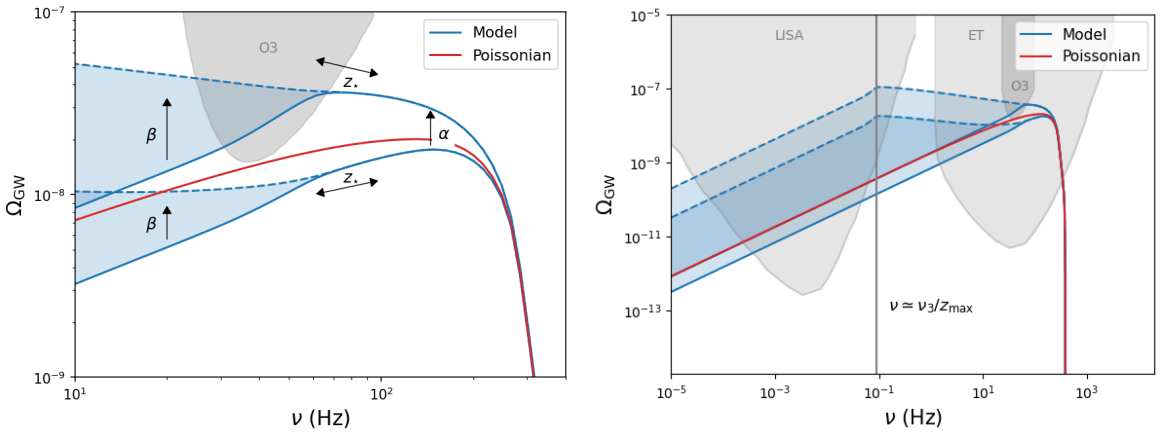

Figure 6.2: Left: Gravitational wave background for the merger rate as given by the broken power law model, for BHs of $30M_\odot$, and varying parameters (α, β, z_*). Here we show the LIGO/Virgo range of frequencies. The parameters for these curves are $R_0 = 9$, $\alpha \in (0.8, 3)$, $\beta \in (-5, 2.7)$, and $z_* = 3.5$. The arrows indicates the effect of varying these parameters. The red curve has $\alpha = 1.1$, $\beta = 1.4$ and $z_* = 1$, and describes the case of an initial Poisson distribution of BHs with no binary disruption. **Right:** Gravitational wave background with the same parameters, expanded to include the LISA frequency range. For the values of z_* under consideration, the signal in the LISA region follows the $\nu^{2/3}$ scaling with an amplitude depending on (α, β, z_*). Let us note that at LISA scales there might be additional contributions to the stochastic background coming from extremely eccentric orbits (where the merger time is given by the free-fall time) that we do not consider here.

this limit, there is an intermediate region not necessarily given by the well known $\nu^{2/3}$ scaling of the IR. Moreover, even when the $\nu^{2/3}$ scaling is achieved, the amplitude of the signal in this region is dependent on β. The strong dependence of the SGWB on the parameters describing the merger rate shows that these might be strongly constrained.

6.3 The signal-to-noise ratio and the abundance criterion

To determine the detectability of the gravitational wave signal, the commonly used criterion relies on the signal-to-noise ratio (SNR) generated in a detector. The SNR quantifies the ratio between the measured signal magnitude and the inherent noise originating from the detector itself, which primarily depends on its construction and technical details. The SNR can be expressed in terms of the frequency-dependent $\Omega_{\rm GW}(\nu)$ as

$$\mathrm{SNR} = \sqrt{T_{\rm obs} \int_{\nu_{\rm min}}^{\nu_{\rm max}} d\nu \left(\gamma(\nu)^2 \frac{\Omega_{\rm GW}(\nu)}{\Omega_{\rm exp}(\nu)} \right)^2}, \tag{6.9}$$

where $T_{\rm obs}$ represents the observation time, $\gamma(\nu)$ denotes the overlap reduction function between two detectors[4], and $\Omega_{\rm exp}(\nu)$ is the noise energy density. This is given in terms of he critical density by [73]

$$\Omega_{\rm exp}(\nu) = \frac{2\pi^2\nu^3 S_n(\nu)}{3H_0^2}, \tag{6.10}$$

where $S_n(\nu)$ is the experimental strain expressed in units of strain/Hz. It is related to the effective amplitude spectral density $h^{1,2}_{\rm eff}(\nu)$ of detectors 1 and 2 through the equation $h^1_{\rm eff}(\nu)h^2_{\rm eff}(\nu) = S_n(\nu)$.

For our analysis, we consider the amplitude spectral density data of Hanford and Livingston detectors from the third run of LIGO/Virgo (O3) [74]. Also, we use the fact that no stochastic background was detected during a time interval of 205.4 days of coincident observations between the Hanford and Livingston detectors [75]. For the analysis on the constraints for future experiments, we use the Advanced LIGO (aLIGO) design configuration, the Einstein Telescope (ET), LISA, and SKA. The amplitude spectral density data for these experiments, except for LISA and SKA, are obtained from [74]. The data for SKA is obtained from [76], while for LISA we follow the procedure outlined in [77]. In the case of LISA, the noise energy density $\Omega_{\rm exp}(\nu)$ is given by:

$$\Omega_{\rm exp}(\nu) = \Omega_{\rm I}(\nu)\frac{4\pi^2\nu^3}{3H_0^2}, \text{ with } \Omega_{\rm I}(\nu) = \sqrt{2}\frac{20}{3}\left[\frac{f_1(\nu)}{(2\pi\nu)^4} + f_2(\nu)\right]\left[1 + \left(\frac{\nu}{4\nu^\star/3}\right)^2\right], \tag{6.11}$$

with $\nu^\star = c/2\pi L$ and $L = 2.5 \times 10^6$ km. The functions $f_1(\nu)$ and $f_2(\nu)$ are given by $f_1(\nu) = 5.76 \times 10^{-48}\left(1 + \left(\frac{\bar{\nu}}{\nu}\right)^2\right)$ Hz^3 and $f_2(\nu) = 3.6 \times 10^{-41}$Hz^{-1}, where $\bar{\nu} = 0.4$ mHz, and the effective observation time is set to $T_{\rm obs} = 3$ years.

With all these considerations in mind, we can determine the SNR for the aforementioned experiments[5]. In our analysis, we set the detection threshold at SNR $= 2$ and initially use the absence of a signal detection in LIGO/Virgo O3 to constrain the triplets (α, β, z_*) that would yield an $SNR > 2$.

6.3.1 The abundance constraint

Additionally to the SNR constraint, another one arises from the observation that the total energy density of PBHs must not exceed the total energy density of dark matter.

[4] In order to detect a stochastic background, it is necessary to utilize two separate detectors to overcome the noise present. The overlap function can be found in Ref. [72]

[5] It is important to note that there are expected to be numerous sources of gravitational waves acting as foregrounds to this signal, thus a more detailed estimation of the SNR should also consider the ability to separate these components [78, 79].

By analyzing the merger rate history $R(z)$, we can determine the total number of black holes in binary form. Let $f_{\rm b}$ represent the fraction of black holes in binaries and $f_{\rm bh}$ denote the total amount of dark matter in the form of black holes. Then the number density of black holes in binaries is given by

$$\int_0^{z_{\rm max}} \frac{R(z)}{H_0(1+z)E(z)} dz = f_{\rm b} f_{\rm BH} \frac{n_{\rm DM}}{2}. \tag{6.12}$$

where $n_{\rm DM}$ represents the number density of dark matter. Typically, the fraction of black holes in binaries, $f_{\rm b}$, is expected to be quite small. Simulations of black hole clusters have shown values on the order of $f_{\rm b} \simeq \mathcal{O}(10^{-3})$ [38]. Assuming this as a fiducial value and because $f_{\rm BH} \leq 1$, we can establish that

$$\int_0^{z_{\rm max}} \frac{R(z)}{H_0(1+z)E(z)} dz \leq 0.001\, n_{\rm DM}\,, \tag{6.13}$$

This equation allows us to constrain the possible values of (α, β, z_*).

6.3.2 Priors for the model parameters

Exploring the entire parameter space is computationally extensive, so we will focus on a restricted parameter range of interest.

We will only consider values for the transition redshift $z_* \geq 0.8$. This ensures that the change in the merger rate slope occurs at redshifts higher than the most distant directly observed binary merger, maintaining the validity of the current constraints on α from direct observations. As for the range of α, we will choose the interval $(0, 5)$, keeping in mind that values below $\alpha < 0.8$ lie outside the 90% confidence level obtained from the analysis of direct observations [24]. Since our focus is to explore new merger histories for PBHs, we will allow $\beta > 0$. For positive β values, the abundance criteria given by Eq. (6.13) leads to the restriction $\beta \lesssim 2.3$, roughly independent of α and z_* (for $z_* \ll z_{\rm max}$). We will also consider case with $\beta < 0$, since it describes well the merger history astrophysical black hole binaries [80]. With these considerations, we will set $-5 < \beta < 5$.

Taking a conservative position, we will finaly set R_0 as the minimum allowed by direct detection, specifically $R_0 = 9$. Therefore, the constraints presented here serve as a lower bound on the SNR within this model. By choosing R_0 consistent with the current merger rate, we implicitly assume that the sum of all black holes (astrophysical and primordial) follows such a power law. Consequently, the change in the slope at z_* could also represent a transition in the binary population, such as a shift from astrophysical to primordial binaries.

6.4 Results

In this section we present contours of the SNR as a function of the parameters α, β and z_*. Note that since the shape of the signal (and not just the overall amplitude or scale) changes with the varying parameters, it is probably not very accurate to compare our model with a single integrated sensitivity curve (which is constructed assuming a signal with a single power law), as can be done e.g. in [81, 82]. For the baseline cosmological model we use the results of the Planck satellite [83].

6.4.1 LIGO/Virgo - O3 run - Present Constraints

In Figure 6.3 we show the SNR for the LIGO/Virgo O3 run. The region in grey corresponds to sections of the parameter space where SNR$>$ 2, and thus can be considered ruled out by the non-observation of a stochastic background. The green dashed line shows the equality of the abundance constraint Eq. (6.13), so all the parameters above that line are also ruled out.

From these results we can see that LIGO/Virgo O3 is sensitive to the changes in the stochastic background coming from the evolution of the merger rate at large redshift ($4 > z > 0.8$). On the other hand, the SGWB is not very sensitive to changes in the merger rate happening at redshift $z_* > 4$. This shows that using the stochastic background we can constrain the merger rate at redshifts larger than the horizon redshift for the detection of individual mergers, $z_{\rm hor} \simeq 1$.

In general, we find that the non detection of a stochastic background largely restricts the allowed parameter space. We find that for any β and for $z_* > 0.8$, $\alpha < 3.7$. The maximum allowed value for α decreases as the redshift of transition increases. For $z_* > 4$, we found $\alpha < 1.3$, which combined with the direct observation constraint implies that α lies in the small range $0.8 < \alpha < 1.3$. As for β, we found that it is also greatly constrained. For transitions happening at redshift $z_* < 1.6$, we find $\beta < 2.3$ from the non-detection of a SGWB. For transitions happening at larger redshifts, larger values of β are allowed from the perspective of the SGWB, but then either the abundance constraint or the direct detection constraint on α is not satisfied.

6.4.2 The Poissonian PBH case

An interesting case is when the merger rate is given by a population of PBHs following an initial Poissonian distribution. The simplest way to constrain this scenario is with the total number of events. For $R_0 = 9 - 35$ Gpc^{-3}yr^{-1}, this implies that $0.001 < f_{\rm PBH} < 0.001 - 0.003$ (considering R_0 as the maximum possible number of PBH binary mergers)[6]. Interestingly however, the stochastic background provides a

[6] In this case, an analytical expression for the merger rate can also be obtained [8, 31].

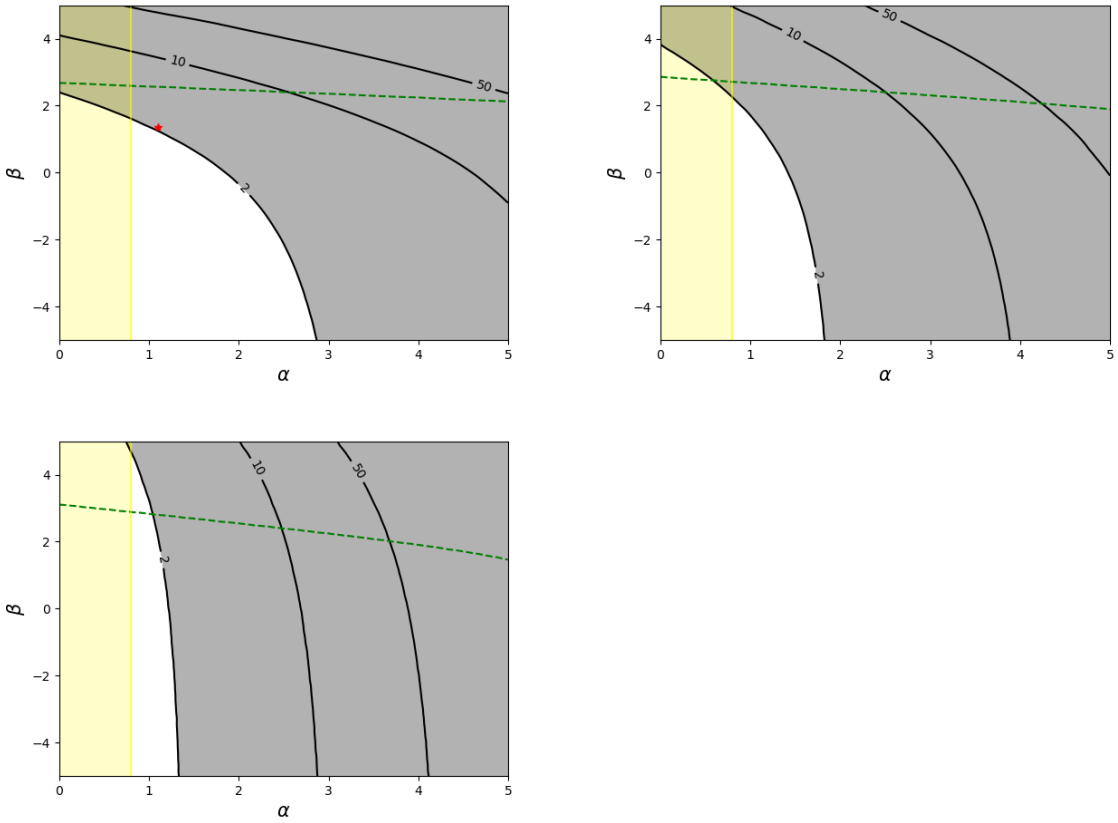

Figure 6.3: SNR for LIGO/Virgo O3 run and for our model. At the top left $z_* = 1$ (where we highlight in red the Poissonian case, $\alpha = 1.1$ and $\beta = 1.4$), while at the top right $z_* = 2$ and at the bottom $z_* = 4$. The SNR becomes independent of β when the transition z_* happens for $z > 4$. For $z_* < 4$, the constraints on the high redshift evolution (β) are similar to the low redshift evolution (α). The green line is the equality of the abundance criterion, given in Eq. (**??**) and with $z_{\rm max} = z_{\rm eq}$ (practicaly the same bound is found for $z_{\rm max} > z_{\rm eq}$) and the yellow band is the exclusion of α coming from direct measurements.

competitive constraint on the abundance (see [29] for a previous analysis along these lines). In this case, $\alpha = 1.1$, $\beta = 1.4$ and $z_* = 1$ (shown in red in Figure 6.2 for $R_0 = 9$ Gpc^{-3}yr^{-1}). For these parameters SNR < 2 implies $R_0 < 8$, which from the expression above implies $f_{\rm PBH} < 0.001$. This shows that the constraints coming from the stochastic background are of the same order, or even stronger, than the constraint coming from direct observations.

6.4.3 Future constraints in LIGO/Virgo and LISA band.

While the O3 constraints still leave some part of the parameter space viable, future runs of LIGO/Virgo/Kagra and future GW experiments operating at frequencies larger

that 10^{-4} Hz should be able to detect a signal for this family of merger rates. In Figure 6.4 (left pannel, black curve) we show the smallest SGWB background from this model that is allowed by O3 (i.e $\alpha = 0.8, \beta = -5, R_0 = 9, z_* = 1$)[7].

For any allowed parameter, the signal should thus be visible by future runs of LIGO/Virgo, and also by LISA, which operates at smaller frequencies than LIGO/Virgo, around $(10^{-4}, 10^{-1})$ Hz. This interplay between observations in LIGO/Virgo and LISA bands has already been discussed for PBHs [30, 84–86].

Even though at intermediate frequencies, $\nu \in (0.1, 10)$ Hz, the slope of the SGWB shows large deviations with respect to the canonical $\nu^{2/3}$ scaling, in the LISA frequency range this scaling is recovered. The amplitude at these scales however depends on the parameters (α, β).

These considerations imply that if we only consider observations in the LISA band there might be a degeneracy between (α, β) and the mass of the binary system, since BBHS with larger masses results in spectra radiating at smaller frequencies. This degeneracy is however broken by comparing the signal at both LIGO/Virgo and LISA bands.

Naturally, experiments planned at frequencies between LISA and LIGO/Virgo, as Einstein Telescope [40], DECIGO [87] and TianQin [88] will also contribute in a similar direction. These experiments have the advantage of being sensitive in the range of frequencies where the signal deviates from the $\nu^{2/3}$ scaling.

6.4.4 Pulsar Timing Arrays

The infrared tail of the SGWB might be largely enhanced with respect to the Poissonian case and thus there might be consequences for observables at very small frequencies. In particular, it is interesting to compute the predictions at pulsar timing array scales, lying in a frequency interval $\nu \in (10^{-9}, 10^{-6})$ Hz.

The signal detected by the NANOGrav collaboration [42] has already been shown to be accommodated by the IR tail of the stochastic background coming from mergers of super (or "stupendously") massive BHs, either of astrophysical [89] or primordial origin [2]. We found however that for BBHS of $30M_\odot$ the enhancement is not so pronounced to neither explain the NANOGrav signal nor being detectable by SKA (and at the same time being consistent with LIGO current bounds and the abundance

[7] For small β, the SGWB becomes independent of β. In this sense $\beta = -5$ is very similar to considering a sharp cutoff ($\beta \to -\infty$).

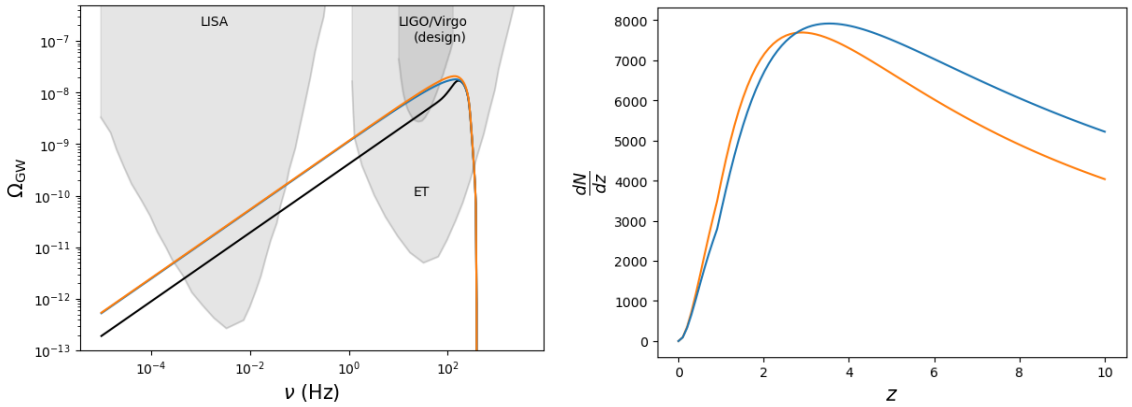

Figure 6.4: Left: SGWB for two different models generating a very similar stochastic background and characterized by the following parameters. Model 1 (blue): $\alpha = 0.5$, $\beta = 0.25$ and $z_{\max} = 0.8$ and Model 2 (orange): $\alpha = 0.25$, $\beta = 0.5$ and $z_{\max} = 0.8$. In black we show the smallest stochastic background generated by this class of models ($R_0 = 9$, $\alpha = 0.8$, $\beta = -5$ and $z_* = 0.8$). This means that the signal should be observed among other observatories, by LIGO/Virgo design configuration, ET and LISA. **Right:** Number of expected mergers, for the same value of the parameters. While the stochastic background are nearly degenerated, there are large differences in the expected number of events in the ET.

constraint) [8]. It might be possible however that for BBH of larger masses, the signal at these scales is large enough to be detectable.

6.4.5 A joint analysis with direct detection: Einstein Telescope

Here we discuss in more detail the prospects for making a joint observation of the stochastic background and individual sources. For mergers of this mass, the Einstein Telescope (ET) should detect individual mergers, up to redshifts $z \simeq 10$ [90].

In order to better assess its constraining power, lets take two sets of parameters having the same SNR in the stochastic background in the LIGO experiment, for example (α, β)=(0.7,0.2) and (α, β)=(0.2,0.7), with $z_* = 0.8$ in both cases. These two sets of parameters generate an almost identical stochastic background, as can be seen in Figure 6.4. However they could be distinguishable if the merger rate as a function of redshift can be inferred from direct observations. We can estimate the number of

[8] Note that since we are extrapolating to very small frequencies, the first thing is to determine the smallest possible frequency generated by a merger. In particular, for a spectrum of the form given by Eq.(5.22), it is assumed that the frequency spectrum has a tail $\nu^{-1/3}$ in the IR, without any additional cutoff. We should however consider that at any time there is a minimum frequency at which a binary can radiate, given by the maximum distance at which they could be separated. This in turn is given by the radius at which they decouple from the Hubble flow. This is found to be $\nu_{\min}(z) = (1+z)^{1/3} \left(\frac{M}{\rho_{\rm eq} a_{\rm eq}^4}\right)^{-1/3}$, which is smaller than PTA scales for the masses considered.

mergers observed by the ET by using the expression

$$N_{\rm obs}(z) = \int_0^z dz' \; R(z') \left(\frac{dV_c}{dz'}\right) \left(\frac{T_{\rm obs}}{1+z'}\right) P_{ET}(z') \; , \tag{6.14}$$

where we have denoted by V_c the comoving volume given by,

$$\left(\frac{dV_c}{dz}\right) = 4\pi \left(\frac{1}{H_0}\right)^3 \left(\int_0^z \frac{dz'}{E(z')}\right)^2 E(z)^{-1} \; , \tag{6.15}$$

and we take the probability of observation of these mergers to be $P_{ET}(z) \approx 1$ for $z < 10$. Finally, we take the observation time, $T_{\rm obs}$, to be 1 year.

Using the expressions above we can find the number of expected mergers as a function of redshift. In Figure 6.4 we show the number of sources that ET should detect, showing that both models generate large differences in the number count. This means that we can use this measurement to break the degeneracy between models whose signal to noise ratio for the stochastic background is the same.

Conclusions

In the first part of the thesis we studied in detail the dynamics of a domain wall nucleated during inflation and its post-inflationary evolution. We paid particular attention to the continuity of the metric and of the wall velocity at the surface where inflation ends and the decelerating phase starts, and to the jumps of the extrinsic curvature at matching hypersurfaces where appropriate. We then proceeded to calculate the energy momentum tensor of a conformally coupled scalar field in this background, starting from de Sitter invariant initial conditions. For simplicity, the calculation is done in a dimensionally reduced 1+1 version, ommiting angular coordinates.

We find that the energy momentum tensor remains finite everywhere during the evolution, diverging only as we approach the black hole singularity. The spacetime includes a segment of the maximally extended Schwarzschild solution, containing an Einstein-Rosen bridge. This is a transient wormhole connecting the parent universe with a baby universe. No pathologies occur on the past event horizons of the Schwarzschild segment, and Hawking radiation emanates from the two future event horizons facing the parent and the baby universe, at the expected temperature. The trace anomaly changes abruptly at the end of inflation, causing transient fluxes of radiation towards the FLRW regions on both sides of the wall. We have clarified the distribution of energy, pressure and fluxes by comparing the experiences of five different observers which, from a common origin, end up in diffferent disconnected subsets of the future boundary. We conclude that such quantum effects are small and therefore the dynamics of PBH formation is semiclassically stable, even when the PBH carries a baby universe.

In the second part of the thesis, we concentrated on constraining the merger rate history of PBH binaries from SBGW. Motivated by a clustered distribution of PBHs, which can have an increasing merger rate up to large redshifts, we have shown that if the rate exhibits changes in its slope, a wide range of possible stochastic backgrounds can be generated.

Typically, the magnitude of the SBGW is expected to have a $\nu^{2/3}$ scaling at $\nu \ll \nu_3/z_{\rm max}$ where $\nu_3 \approx 10^2$Hz for PBH of mass $M \sim 30\,M_\odot$ and $z_{\rm max}$ is the highest redshift at which binary mergers contribute. In particular, we have shown that in a mid-frequency range of the SBGW, between $\nu \in (\nu_3/z_{\rm max}, \nu_3)$, the spectra can exhibit slopes that are

different from $\nu^{2/3}$. At small frequencies, where the typical $\nu^{2/3}$ scaling is recovered, the amplitude turns out to be highly dependent on the slope of the merger rate. This dependence shows that the SBGW is a powerful probe of the merger history of BBHs.

We have thus analysed to which extent the current non-detection of a SBGW constrains the merger rate. We find that, indeed, this constrains the merger rate at redshift as high as $z \sim 4$, much larger than the maximum redshift at which binary mergers have been detected. We have also shown that future runs of LIGO/Virgo should be able to detect such SGWB and that the signal should be visible by LISA for any of the considered parameters of the model.

We have finally considered the prospects of Einstein Telescope for determining the merger rate through the observations of individual mergers. The expected number of BBHs is so large that the existing degeneracies in the stochastic background can be broken, meaning that the merger rate can be unambiguously determined.

APPENDICES

A Matching conditions

In this Appendix we review the matching conidtions that allows us to construct more complex spacetimes by patching together different solution of Einstein's equations so that resulting spacetime is also a solution. Such matching conditions are given by Darmois and Israel (see Refs. [91, 92]) for timelike (or spacelike) hypersurfaces. In the next lines, we introduce some notation and definitions, and formulate the matching conditions. Consider a 3-dimensional timelike or spacelike hypersurface Σ that divides the spacetime M in two regions $M^{\pm}$ with metrics $g^{\pm}_{\mu\nu}$. Let $N^{\pm}_{\mu}$ be the normal vector to Σ as seen from each side of the hypersurface. Then we can define the induced metric on Σ and the extrinsic curvature as

$$h_{\mu\nu} \equiv g_{\mu\nu} - \epsilon N_\mu N_\mu \,, \quad K_{\mu\nu} \equiv h^{\alpha}_{\mu} \nabla_\alpha N_\nu$$

where $\epsilon = +1(-1)$ if Σ is timelike (spacelike). Let us introduce the following notation for any quantity A

$$[A]^{\pm} \equiv A(M^+)|_\Sigma - A(M^-)|_\Sigma$$

Then, the Israel's matching conditions are formulated as

$$\text{First condition:} \quad [h_{\mu\nu}] = 0 \tag{A.1a}$$

$$\text{Second condition:} \quad S_{\mu\nu} = -\frac{\epsilon}{8\pi}\left([K_{\mu\nu}] - [K]\, h_{\mu\nu}\right) \tag{A.1b}$$

where S_{ab} is the stress-energy tensor of matter fields in Σ and $K = K_{ab}h^{ab}$. The first condition (A.1a) impose that the induced metric must be continuous through Σ. The second one (A.1b) relates the jump of the extrinsic curvature with the presence of some matter distribution on Σ.

A.1 Spherically symmetric spacetimes

Let us now consider spherically symmetric spacetimes

$$\mathrm{d}s^2 = -A(t,\chi)\mathrm{d}t^2 + B(t,\chi)\mathrm{d}\chi^2 + R(t,\chi)^2\mathrm{d}\Omega^2 \tag{A.2}$$

and spherically symmetrical hypersurfaces with 4-velocity

$$u^\mu = (\dot{t}(\tau), \dot{\chi}(\tau), 0, 0) \tag{A.3}$$

Then, the first junction condition (A.1a) gives us

$$\begin{aligned}\left[-A(t,\chi)\dot{t}^2(\tau)+B(t,\chi)\dot{\chi}^2(\tau)\right]^{\pm}&=0\\ \left[R(t,\chi)\right]^{\pm}&=0\end{aligned}\tag{A.4}$$

If we consider a purely energy matter field on Σ, with $S_{\mu\nu}=\sigma h_{\mu\nu}$, where σ is the surface energy density then, the (θ,θ)-component of the second junction condition Eq. (A.1b) gives

$$\left[N^{\mu}\partial_{\mu}\log R(t,\chi)\right]^{\pm}=-4\pi G\sigma\tag{A.5}$$

B Evolution of domain walls in Schwarzschild spacetime

Here we describe the construction of the solution presented in Section 1.5. By Birkhoff's theorem, each side of the domain wall has to be a Schwarzschild solution Eq. (**??**). The full solution is then contructed by gluing together both Schwarzschilds. Let us denote each side of the wall by $+$ and $-$. Also, we label the radial and temporal component of the trajectory of the wall as seen from each side by $R_{\pm}(\tau)$ and $T_{\pm}(\tau)$ parametrized by the proper time τ. Since it is a spherically symmetric domain wall, the 4-velocity of the trajectory is given by

$$U^{\mu}_{\pm}=(\dot{T}_{\pm},\dot{R}_{\pm},0,0)\tag{B.1}$$

which satisfy $U^{\mu}U_{\mu}=-1$. The first Israel matching condition Eq. (A.4) implies continuity of the radial trajectory, $R_{+}(\tau)=R_{-}(\tau)$ and also $\dot{T}_{+}(\tau)=\pm\dot{T}_{-}(\tau)$.

To apply the second condition, we need to compute the normal vector to the domain wall worldsheet. It has to point towards the same direction as seen from both sides. Moreover it needs to satisfy $N^{\mu}U_{\mu}=0$, $N^{\mu}N_{\mu}=1$. Therefore

$$N^{\mu}_{\pm}=\left(\left(1-\frac{2GM}{R}\right)^{-1}\dot{R},\left(1-\frac{2GM}{R}\right)\dot{T}_{\pm},0,0\right)\tag{B.2}$$

where we have denoted $R=R_{+}=R_{-}$. By denoting $t_{\sigma}=(8\pi G\sigma)^{-1}$, the second Israel's condition Eq. (A.5) implies

$$\frac{1}{R}\left(1-\frac{2GM}{R}\right)(\dot{T}_{+}-\dot{T}_{-})=-\frac{2}{t_{\sigma}}\tag{B.3}$$

Since σ is not zero, then $\dot{T}_{+}=-\dot{T}_{-}$. This implies

$$\dot{T}_{\pm}=\mp\left(1-\frac{2GM}{R}\right)^{-1}\frac{R}{t_{\sigma}}\tag{B.4}$$

From the normalization of the 4-velocity, we obtain

$$\dot{R}^2=\frac{2GM}{R}+\left(\frac{R}{t_{\sigma}}\right)^2-1\tag{B.5}$$

C Derivation of the stress-energy tensor equations

In this Appendix, we derive the equations (3.4) for the renormalized stress-energy tensor $T_{\mu\nu}$, using the conservation equations (3.3) and the quantum trace anomaly (3.2).
By defining the null coordinates $X_\pm = X_0 \pm X_1$, where X_0, X_1 are the time and spatial coordinates respectively, we can write any 1+1 metric as

$$\mathrm{d}s^2 = -\Omega^2 \mathrm{d}X_+ \mathrm{d}X_- \tag{C.1}$$

where $\Omega(X_+, X_-)$ is the conformal factor. There are only two non-zero Christoffel Symbols, which are $\Gamma^+_{++} = 2\partial_+ \log\Omega$ and $\Gamma^-_{--} = 2\partial_- \log\Omega$.
By using this, let us now compute the stress-energy tensor conservation equations

$$\nabla_A T^A_B = \partial_A T^A_B + \Gamma^A_{AC} T^C_B - \Gamma^C_{AB} T^A_C = 0$$

By putting $B = X_-$ we have

$$\partial_- T^-_- + \partial_\mp T^+_- + 2\left(\partial_+ \log\Omega\right) T^+_- = 0 \tag{C.2}$$

This equation can be written in a better and simpler way. First of all, one can observe that the following relations hold

$$\begin{gathered} \left(\partial_+ + 2\partial_+ \log\Omega\right) T^+_- = \Omega^{-2}\partial_+\left(\Omega^2 T^+_-\right), \quad T \equiv T^a_a = 2T^{-+} g_{+-} \\ T^-_- = T^{-+} g_{+-} = T/2, \quad T^+_- = -2\Omega^{-2} T_{--} \end{gathered} \tag{C.3}$$

where T denotes the trace of the stress-energy tensor. From that it follows

$$\partial_+ T_{--} = \frac{\Omega^2}{4}\partial_- T \tag{C.4}$$

Similary, for the X^+ equation, we have an expression for T_{++}

$$\partial_- T_{++} = \frac{\Omega^2}{4}\partial_+ T \tag{C.5}$$

The other components simply read

$$T_{+-} = T_{-+} = -\frac{\Omega^2}{4} T \tag{C.6}$$

Recall that the trace anomaly in 1+1 conformally invariant theory is

$$T = \frac{R}{24\pi} \tag{C.7}$$

with R the Ricci scalar of the metric. For a 1+1 conformally flat metric, the Ricci scalar can be written as

$$R = -2\Omega^{-2}\Box_\eta \log\Omega \tag{C.8}$$

with $\Box_\eta = (-\partial_0^2 + \partial_1^2) = -4\partial_-\partial_+$ is the d'Alambertian in flat space. Therefore, we can express the trace T as

$$T = \frac{1}{3\pi\Omega^2}\partial_-\partial_+ \log\Omega \tag{C.9}$$

By using this, we can write

$$\Omega^2\partial_\pm T = -\frac{1}{3\pi}\partial_\mp\left(\Omega\partial_\pm^2\Omega^{-1}\right) \tag{C.10}$$

Introducing Eqs. (C.10) into Eqs. (C.4) and (C.5) and integrating them, the components of the stress-energy tensor can be written as

$$\begin{aligned} T_{--} &= -\frac{1}{12\pi}\Omega\partial_-^2\Omega^{-1} + F(X_-) \\ T_{++} &= -\frac{1}{12\pi}\Omega\partial_+^2\Omega^{-1} + G(X_+) \\ T_{+-} &= -\frac{1}{12\pi}\partial_+\partial_- \log\Omega \end{aligned} \tag{C.11}$$

To show Eq. (**??**), let us consider two sets of coordinates $\{A, \bar{A}\}$ and $\{B, \bar{B}\}$. Considering the unbar coordinates to be the $\{X_-\}$ ones, we can write the T_{--} component of the stress energy tensor in two different ways

$$T_{AA} = -\frac{1}{12\pi}\Omega_A\partial_A^2\Omega_A^{-1} + F(A)\,, \quad T_{BB} = -\frac{1}{12\pi}\Omega_B\partial_B^2\Omega_B^{-1} + F(B) \tag{C.12}$$

with the conformal factors $\Omega_A(A, \bar{A})$ and $\Omega_B(B, \bar{B})$ related by

$$\Omega_B^2 = \frac{\mathrm{d}A}{\mathrm{d}B}\frac{\mathrm{d}\bar{A}}{\mathrm{d}\bar{B}}\Omega_A^2 \tag{C.13}$$

By using (C.13), we can write T_{BB} in terms of T_{AA}

$$T_{BB} = -\frac{1}{12\pi}\Omega_A\partial_A^2\Omega_A^{-1}\left(\frac{\mathrm{d}A}{\mathrm{d}B}\right)^2 + \frac{1}{24\pi}\left[\left(\frac{\mathrm{d}A}{\mathrm{d}B}\right)^{-1}\left(\frac{\mathrm{d}^3A}{\mathrm{d}B^3}\right) - \frac{3}{2}\left(\frac{\mathrm{d}A}{\mathrm{d}B}\right)^{-2}\left(\frac{\mathrm{d}^2A}{\mathrm{d}B^2}\right)^2\right] + F(B) \tag{C.14}$$

Also, since T_{BB} is a tensor, it transforms covariantly, then

$$T_{BB} = \left(\frac{\mathrm{d}A}{\mathrm{d}B}\right)^2 T_{AA} = \left(\frac{\mathrm{d}A}{\mathrm{d}B}\right)^2\left(-\frac{1}{12\pi}\Omega_A\partial_A^2\Omega_A^{-1} + F(A)\right) \tag{C.15}$$

By comparing (C.14) and (C.15) we conclude

$$F(A) = \left(\frac{\mathrm{d}A}{\mathrm{d}B}\right)^{-2}\left(F(B) + \frac{1}{24\pi}\{A, B\}\right) \tag{C.16}$$

where $\{A, B\}$ is the called Schwarzian derivative, defined as

$$\{A, B\} = \left(\frac{\mathrm{d}A}{\mathrm{d}B}\right)^{-1}\left(\frac{\mathrm{d}^3A}{\mathrm{d}B^3}\right) - \frac{3}{2}\left(\frac{\mathrm{d}A}{\mathrm{d}B}\right)^{-2}\left(\frac{\mathrm{d}^2A}{\mathrm{d}B^2}\right)^2 \tag{C.17}$$

A similar derivation can be done for $G(A)$.

D Some properties of the Schwarzian derivative

Here we enumerate some properties of the Schwarzian derivative that are used to derive the results in Section 3.1.

The first property is that if $A(B)$ are related by a Möbius transformation, that is

$$A(B) = \frac{aB+b}{cB+d}, \quad ad \neq bc \tag{D.1}$$

then the Schwarzian derivative is zero, $\{A(B), B\} = 0$, so the functions F and G transform covariantly.

The second useful property is the following: given a transformation $A(B)$, then the Schwarzian derivative of the inverse $B(A)$ is related by

$$\{A(B), B\} = -\left(\frac{dA}{dB}\right)^2 \{B(A), A\} \tag{D.2}$$

Finally, the last property is the "chain rule" for the Schwarzian derivative. Given two transformations $A(C)$ and $C(B)$, then

$$\{A, B\} = \left(\frac{dC}{dB}\right)^2 \{A, C\} + \{C, B\} \tag{D.3}$$

E Details of the calculation of $T_{\mu\nu}$

E.1 Calculation of $F_{\rm PU}(X^-_{\rm out})$

Here we show how to calculate Eq. (3.15). We expand the Schwarzian derivative as

$$\{X^-_{\rm in}, X^-_{\rm out}\} = \{U_{\rm out}, X^-_{\rm out}\} - \left(\frac{dX^-_{\rm in}}{dX^-_{\rm out}}\right)^2 \{U_{\rm in}, X^-_{\rm in}\} + \left(\frac{dU_{\rm out}}{dX^-_{\rm out}}\right)^2 \{U_{\rm in}, U_{\rm out}\} \tag{E.1}$$

The remaining Schwazian derivatives are easier to compute, since we have and explicit form:

$$\{U, X^-\} = -\frac{P_6(X^-)}{128(1+X^-)^2}, \quad \{U_{\rm in}, U_{\rm out}\} = \frac{1}{U^2_{\rm out}} \frac{2\theta(R, t_\sigma)}{(1+\theta(R,\epsilon))^2} w(R) \tag{E.2}$$

where $\theta(R, t_\sigma)$ is defined in Eq. (1.24), $w(R)$ is defined in the text, and

$$P_6(z) = z^6 + 2z^5 + 7z^4 - 4z^3 + 31z^2 - 94z + 825 \tag{E.3}$$

The remaining derivatives are given by Eqs. (2.11) and (2.13). Therefore the full expression for $F_{\rm PU}(X^-_{\rm out})$ reads

$$F_{\rm PU}(X^-_{\rm out}) = , \qquad \text{for } X^-_{\rm out} > X^-_{\rm out,*} \tag{E.4}$$

The discontinuity at at $X^-_{\rm out,*}$ is given by

$$\Delta F_{\rm PU}(X^-_{\rm out,*}) = \frac{H}{4\pi}\frac{R_*^2}{t_\sigma}\frac{\sqrt{1+(Ht_\sigma)^{-2}-(HR^*)^{-2}}}{\left((Ht_\sigma)^{-1}+\sqrt{1+(Ht_\sigma)^{-2}-(HR^*)^{-2}}\right)^2} \tag{E.5}$$

E.2 Calculation of $G_{\rm BU}(X^+_{\rm in})$

Here we calculate the full expression of Eq. (3.19). We can expand the Schwarzian derivative by applying the chain rule Eq. (D.3),

$$\left\{X^+_{\rm out}, X^+_{\rm in}\right\} = \left\{V_{\rm in}, X^+_{\rm in}\right\} - \left(\frac{dX^+_{\rm out}}{dX^+_{\rm in}}\right)^2 \left\{V_{\rm out}, X^+_{\rm out}\right\} + \left(\frac{dV_{\rm in}}{dX^+_{\rm in}}\right)^2 \left\{V_{\rm out}, V_{\rm in}\right\} \tag{E.6}$$

and the remaining Schwarzian derivatives read

$$\left\{V, X^+\right\} = -\frac{P_6(-X^+)}{128(X^+-1)^2}\,, \qquad \left\{V_{\rm out}, V_{\rm in}\right\} = \frac{1}{V_{\rm in}^2}\frac{2\theta(R,t_\sigma)}{(1+\theta(R,t_\sigma))^2}w(R) \tag{E.7}$$

Therefore,

$$\begin{aligned} G_{\rm BU}(X^+_{\rm in}) = &\frac{P_6(-X^+_{\rm in})}{3072\pi\left(X^+_{\rm in}-1\right)^2} - \frac{w(R)}{1536\pi}\frac{(X^+_{\rm in}-1)^6}{(X^+_{\rm in}-3)^2}\frac{2\theta(R,t_\sigma)}{(1+\theta(R,t_\sigma))^2} \\ &- \frac{P_6(-X^+_{\rm out})}{3072\pi\left(X^+_{\rm out}-1\right)^2}\frac{(X^+_{\rm in}-1)^6}{(X^+_{\rm out}-1)^6}\frac{(X^+_{\rm out}-3)^2}{(X^+_{\rm in}-3)^2}\left(\frac{1-\theta(R,t_\sigma)}{1+\theta(R,t_\sigma)}\right)^2 . \end{aligned} \tag{E.8}$$

Here $R = R(X^+_{\rm in})$, corresponds to the radius of the domain wall at the intersection of the light ray $X^+_{\rm in}$. Also $X^+_{\rm out} = X^+_{\rm out}(X^+_{\rm in})$, obtained from the solution of Eqs. (2.13), is the continuation of the light ray $X^+_{\rm in}$ in the exterior FLRW universe.

At $X^+_{\rm in,*}$, we have

$$G(X^+_{\rm in,*}) = \frac{1}{4\pi}\frac{\frac{HR_*^2}{t_\sigma}\sqrt{1+\frac{Ht_\sigma}{-2-(HR^*)^{-2}}}}{\left((Ht_\sigma)^{-1}+\sqrt{1+(Ht_\sigma)^{-2}-(HR^*)^{-2}}\right)^2} \tag{E.9}$$

E.3 Calculation of $G_{\rm EV}(V_{\rm out})$

Here we compute the full expression for $G(V_{\rm out})$ in Eq. (**??**). The remaining Schwarzian derivative was already computed in the Appendix E.1, so

$$G_{\rm EV}(V_{\rm out}) = -\frac{P_6(-X^+_{\rm out})}{48\pi}\frac{(X^+_{\rm out}-3)^2}{(X^+_{\rm out}-1)^8}\frac{1}{V^2_{\rm out}} \tag{E.10}$$

Here $X^+_{\rm out}(V_{\rm out})$ by solving Eq. (2.11).

E.4 Calculation of $F_{\rm EV}(U_{\rm out})$

Here we compute Eq. (3.25). Expanding the Schwarzian derivative we obtain

$$F_{\rm EV}(U_{\rm out}) = -\frac{1}{24\pi}\left\{U_{\rm int}, U_{\rm out}\right\} + \frac{1}{24\pi}\left(\frac{dU_{\rm out}}{dX^-_{\rm int}}\right)^{-2}\left\{U_{\rm int}, X^-_{\rm int}\right\} \tag{E.11}$$

The remaining quantites have already been computed. This leads to

$$F_{\rm EV}(U_{\rm out}) = -\frac{w(R)}{24\pi U^2_{\rm out}}\frac{2\theta(R,t_\sigma)}{(1+\theta(R,t_\sigma))^2} - \frac{P_6(X^-_{\rm int})}{48\pi U^2_{\rm out}}\left(\frac{1-\theta(R,t_\sigma)}{1+\theta(R,t_\sigma)}\right)^2\frac{(3+X^-_{\rm int})^2}{(1+X^-_{\rm int})^8} \tag{E.12}$$

Here $R = R(U_{\rm out})$ is the radius of the wall at the moment it intersects with the ray $U_{\rm out}$. Also $X^-_{\rm int} = X^-_{\rm int}(U_{\rm out})$ is the continuation of the light ray $U_{\rm out}$ at the FLRW region of the baby universe.

E.5 Calculation of $G_{\rm IV}(V_{\rm int})$

Here we compute Eq. (3.26) By expanding the Schwarzian derivative we get

$$\left\{V_{\rm int}, X^+_{\rm out}\right\} = \left(\frac{dV_{\rm out}}{dX^+_{\rm out}}\right)^2\left\{V_{\rm int}, V_{\rm out}\right\} + \left\{V_{\rm out}, X^+_{\rm out}\right\} \tag{E.13}$$

The remaining Schwarzian have been already computed. The end result is

$$G_{\rm IV}(V_{\rm int}) = -\frac{P_6\left(-X^+_{\rm out}\right)}{48\pi V^2_{\rm int}}\frac{(X^+_{\rm out}-3)^2}{(X^+_{\rm out}-1)^8}\left(\frac{1-\theta(R,t_\sigma)}{1+\theta(R,t_\sigma)}\right)^2 - \frac{w(R)}{24\pi V^2_{\rm int}}\frac{2\theta(R,t_\sigma)}{\left(1+\theta(R,t_\sigma)\right)^2} \tag{E.14}$$

with $R = R(V_{\rm in})$ is the radius of the wall at the moment it interects the light ray $V_{\rm in}$, $U_{\rm in}(V_{\rm in})$ is given by the trajectory of the domain wall, and $X^+_{\rm out} = X^+_{\rm out}\left(V_{\rm int}\right)$ is the continuation of the light ray $V_{\rm int}$ to the FLRW region of the parent universe.

E.6 Calculation of $F_{\mathrm{IV}}(U_{\mathrm{int}})$

Finally we show the full expression for Eq. (3.27) which is given by

$$F_{\mathrm{IV}}(U_{\mathrm{int}}) = -\frac{P_6(X_{\mathrm{int}}^-)}{48\pi U_{\mathrm{int}}^2}\frac{\left(3+X_{\mathrm{int}}^-\right)^2}{(1+X_{\mathrm{int}}^-)^8}\,, \qquad \text{for } U_{\mathrm{int}} < U_{\mathrm{int},\circ} \tag{E.15}$$

and

$$F_{\mathrm{IV}}(U_{\mathrm{int}}) = -\frac{P_6(X_{\mathrm{int}}^-)}{48\pi U_{\mathrm{int}}^2}\frac{\left(3+X_{\mathrm{int}}^-\right)^2}{(1+X_{\mathrm{int}}^-)^8} + \left(\frac{dU_{\mathrm{int}}}{dX_{\mathrm{int}}^-}\right)^{-2} G_{\mathrm{BU}}(X_{\mathrm{int}}^+ \to X_{\mathrm{int}}^-)\,, \qquad \text{for } U_{\mathrm{int}} < U_{\mathrm{int},\circ} \tag{E.16}$$

Bibliography

[1] Vicente Atal et al. "Constraining changes in the merger history of BH and PBH binaries with the stochastic gravitational wave background". In: *Phys. Rev. D* 105.12 (2022), p. 123522. DOI: 10.1103/PhysRevD.105.123522. arXiv: 2201.12218 [astro-ph.CO] *Cited on page ix.*

[2] Vicente Atal, Albert Sanglas, and Nikolaos Triantafyllou. "NANOGrav signal as mergers of Stupendously Large Primordial Black Holes". In: *JCAP* 06 (2021), p. 022. DOI: 10.1088/1475-7516/2021/06/022. arXiv: 2012.14721 [astro-ph.CO] *Cited on pages ix, 73.*

[3] Vicente Atal, Albert Sanglas, and Nikolaos Triantafyllou. "LIGO/Virgo black holes and dark matter: The effect of spatial clustering". In: *JCAP* 11 (2020), p. 036. DOI: 10.1088/1475-7516/2020/11/036. arXiv: 2007.07212 [astro-ph.CO] *Cited on pages ix, 3, 64.*

[4] Jaume Garriga and Albert Sanglas. "Evaporation of a supercritical primordial black hole". In: (in preparation for submission) *Cited on page ix.*

[5] Misao Sasaki et al. "Primordial Black Hole Scenario for the Gravitational-Wave Event GW150914". In: *Phys. Rev. Lett.* 117.6 (2016). [Erratum: Phys.Rev.Lett. 121, 059901 (2018)], p. 061101. DOI: 10.1103/PhysRevLett.117.061101. arXiv: 1603.08338 [astro-ph.CO] *Cited on page 1.*

[6] Simeon Bird et al. "Did LIGO detect dark matter?" In: *Phys. Rev. Lett.* 116.20 (2016), p. 201301. DOI: 10.1103/PhysRevLett.116.201301. arXiv: 1603.00464 [astro-ph.CO] *Cited on page 1.*

[7] Sebastien Clesse and Juan García-Bellido. "The clustering of massive Primordial Black Holes as Dark Matter: measuring their mass distribution with Advanced LIGO". In: *Phys. Dark Univ.* 15 (2017), pp. 142–147. DOI: 10.1016/j.dark.2016.10.002. arXiv: 1603.05234 [astro-ph.CO] *Cited on page 1.*

[8] Misao Sasaki et al. "Primordial black holes—perspectives in gravitational wave astronomy". In: *Class. Quant. Grav.* 35.6 (2018), p. 063001. DOI: 10.1088/1361-6382/aaa7b4. arXiv: 1801.05235 [astro-ph.CO] *Cited on pages 1, 71.*

[9] Anne M. Green and Bradley J. Kavanagh. "Primordial Black Holes as a dark matter candidate". In: *J. Phys. G* 48.4 (2021), p. 043001. DOI: 10.1088/1361-6471/abc534. arXiv: 2007.10722 [astro-ph.CO] *Cited on page 1.*

[10] B. P. Abbott et al. "Observation of Gravitational Waves from a Binary Black Hole Merger". In: *Phys. Rev. Lett.* 116.6 (2016), p. 061102. DOI: 10.1103/PhysRevLett.116.061102. arXiv: 1602.03837 [gr-qc] *Cited on page 1.*

[11] B. P. Abbott et al. "GW151226: Observation of Gravitational Waves from a 22-Solar-Mass Binary Black Hole Coalescence". In: *Phys. Rev. Lett.* 116.24 (2016), p. 241103. DOI: 10.1103/PhysRevLett.116.241103. arXiv: 1606.04855 [gr-qc] *Cited on page 1.*

[12] Benjamin P. Abbott et al. "GW170104: Observation of a 50-Solar-Mass Binary Black Hole Coalescence at Redshift 0.2". In: *Phys. Rev. Lett.* 118.22 (2017), p. 221101. DOI: 10.1103/PhysRevLett.118.221101. arXiv: 1706.01812 [gr-qc] *Cited on page 1.*

[13] Rama Basu, Alan H Guth, and Alexander Vilenkin. "Quantum creation of topological defects during inflation". In: *Physical Review D* 44.2 (1991), p. 340 *Cited on pages 1, 11, 12, 14.*

[14] Norihiro Tanahashi and Chul-Moon Yoo. "Spherical domain wall collapse in a dust universe". In: *Classical and Quantum Gravity* 32.15 (2015), p. 155003 *Cited on pages 1, 23.*

[15] Jaume Garriga, Alexander Vilenkin, and Jun Zhang. "Black holes and the multiverse". In: *J. Cosmol. Astropart. Phys.* 2 (2016), 064, front matter+37. DOI: 10.1088/1475-7516/2016/02/064 *Cited on pages 1, 16, 20, 21, 23, 24.*

[16] Heling Deng, Jaume Garriga, and Alexander Vilenkin. "Primordial black hole and wormhole formation by domain walls". In: *JCAP* 04 (2017), p. 050. DOI: 10.1088/1475-7516/2017/04/050. arXiv: 1612.03753 [gr-qc] *Cited on pages 1, 23.*

[17] Heling Deng and Alexander Vilenkin. "Primordial black hole formation by vacuum bubbles". In: *JCAP* 12 (2017), p. 044. DOI: 10.1088/1475-7516/2017/12/044. arXiv: 1710.02865 [gr-qc] *Cited on page 1.*

[18] Heling Deng, Alexander Vilenkin, and Masaki Yamada. "CMB spectral distortions from black holes formed by vacuum bubbles". In: *JCAP* 07 (2018), p. 059. DOI: 10.1088/1475-7516/2018/07/059. arXiv: 1804.10059 [gr-qc] *Cited on page 1.*

[19] Heling Deng. "Spiky CMB distortions from primordial bubbles". In: *JCAP* 05 (2020), p. 037. DOI: 10.1088/1475-7516/2020/05/037. arXiv: 2003.02485 [astro-ph.CO] *Cited on page 1.*

[20] Heling Deng. "Primordial black hole formation by vacuum bubbles. Part II". In: *JCAP* 09 (2020), p. 023. DOI: 10.1088/1475-7516/2020/09/023. arXiv: 2006.11907 [astro-ph.CO] *Cited on page 1.*

[21] Heling Deng. "μ-distortion around stupendously large primordial black holes". In: *JCAP* 11.11 (2021), p. 054. DOI: 10.1088/1475-7516/2021/11/054. arXiv: 2106.09817 [astro-ph.CO] *Cited on page 1.*

[22] Jibin He et al. "Implications of GWTC-3 on primordial black holes from vacuum bubbles". In: (Mar. 2023). arXiv: 2303.16810 [astro-ph.CO] *Cited on page 1.*

[23] Alexander Kusenko et al. "Exploring Primordial Black Holes from the Multiverse with Optical Telescopes". In: *Phys. Rev. Lett.* 125 (2020), p. 181304. DOI: 10.1103/PhysRevLett.125.181304. arXiv: 2001.09160 [astro-ph.CO] *Cited on page 1.*

[24] R. Abbott et al. "The population of merging compact binaries inferred using gravitational waves through GWTC-3". In: *arXiv: 2111.03634* (Nov. 2021) *Cited on pages 2, 63, 66, 70.*

[25] R. Abbott et al. "GWTC-3: Compact Binary Coalescences Observed by LIGO and Virgo During the Second Part of the Third Observing Run". In: (Nov. 2021). arXiv: 2111.03606 [gr-qc] *Cited on page 2.*

[26] Pablo A. Rosado. "Gravitational wave background from binary systems". In: *Phys. Rev. D* 84 (2011), p. 084004. DOI: 10.1103/PhysRevD.84.084004. arXiv: 1106.5795 [gr-qc] *Cited on pages 3, 63.*

[27] C. Wu, V. Mandic, and T. Regimbau. "Accessibility of the Gravitational-Wave Background due to Binary Coalescences to Second and Third Generation Gravitational-Wave Detectors". In: *Phys. Rev. D* 85 (2012), p. 104024. DOI: 10.1103/PhysRevD.85.104024. arXiv: 1112.1898 [gr-qc] *Cited on pages 3, 63.*

[28] Vuk Mandic, Simeon Bird, and Ilias Cholis. "Stochastic Gravitational-Wave Background due to Primordial Binary Black Hole Mergers". In: *Phys. Rev. Lett.* 117.20 (2016), p. 201102. DOI: 10.1103/PhysRevLett.117.201102. arXiv: 1608.06699 [astro-ph.CO] *Cited on pages 3, 63.*

[29] Sai Wang et al. "Constraints on the Primordial Black Hole Abundance from the First Advanced LIGO Observation Run Using the Stochastic Gravitational-Wave Background". In: *Phys. Rev. Lett.* 120.19 (2018), p. 191102. DOI: 10.1103/PhysRevLett.120.191102. arXiv: 1610.08725 [astro-ph.CO] *Cited on pages 3, 60, 63, 72.*

[30] Sebastien Clesse and Juan García-Bellido. "Detecting the gravitational wave background from primordial black hole dark matter". In: *Phys. Dark Univ.* 18 (2017), pp. 105–114. DOI: 10.1016/j.dark.2017.10.001. arXiv: 1610.08479 [astro-ph.CO] *Cited on pages 3, 63, 73.*

[31] Martti Raidal, Ville Vaskonen, and Hardi Veermäe. "Gravitational Waves from Primordial Black Hole Mergers". In: *JCAP* 09 (2017), p. 037. DOI: 10.1088/1475-7516/2017/09/037. arXiv: 1707.01480 [astro-ph.CO] *Cited on pages 3, 56, 63, 71.*

[32] Martti Raidal et al. "Formation and Evolution of Primordial Black Hole Binaries in the Early Universe". In: *JCAP* 02 (2019), p. 018. DOI: 10.1088/1475-7516/2019/02/018. arXiv: 1812.01930 [astro-ph.CO] *Cited on pages 3, 63, 64.*

[33] Suvodip Mukherjee and Joseph Silk. "Can we distinguish astrophysical from primordial black holes via the stochastic gravitational wave background?" In: *Mon. Not. Roy. Astron. Soc.* 506.3 (2021), pp. 3977–3985. DOI: 10.1093/mnras/stab1932. arXiv: 2105.11139 [gr-qc] *Cited on pages 3, 63.*

[34] Suvodip Mukherjee, Matthew S. P. Meinema, and Joseph Silk. "Prospects of discovering sub-solar primordial black holes using the stochastic gravitational wave background from third-generation detectors". In: *arXiv: 2107.02181* (July 2021) *Cited on pages 3, 63.*

[35] Thomas Callister et al. "Shouts and Murmurs: Combining Individual Gravitational-Wave Sources with the Stochastic Background to Measure the History of Binary Black Hole Mergers". In: *Astrophys. J. Lett.* 896.2 (2020), p. L32. DOI: 10.3847/2041-8213/ab9743. arXiv: 2003.12152 [astro-ph.HE] *Cited on pages 3, 63.*

[36] Kohei Inayoshi et al. "Gravitational Wave Backgrounds from Coalescing Black Hole Binaries at Cosmic Dawn: An Upper Bound". In: *Astrophys. J.* 919.1 (2021), p. 41. DOI: 10.3847/1538-4357/ac106d. arXiv: 2103.12755 [astro-ph.CO] *Cited on pages 3, 63.*

[37] Karsten Jedamzik. "Consistency of Primordial Black Hole Dark Matter with LIGO/Virgo Merger Rates". In: *Phys. Rev. Lett.* 126.5 (2021), p. 051302. DOI: 10.1103/PhysRevLett.126.051302. arXiv: 2007.03565 [astro-ph.CO] *Cited on pages 3, 64.*

[38] Manuel Trashorras, Juan García-Bellido, and Savvas Nesseris. "The clustering dynamics of primordial black boles in N-body simulations". In: *Universe* 7.1 (2021), p. 18. DOI: 10.3390/universe7010018. arXiv: 2006.15018 [astro-ph.CO] *Cited on pages 3, 64, 70.*

[39] Fabio Antonini and Mark Gieles. "Merger rate of black hole binaries from globular clusters: theoretical error bars and comparison to gravitational wave data from GWTC-2". In: *Phys. Rev. D* 102 (2020), p. 123016. DOI: 10.1103/PhysRevD.102.123016. arXiv: 2009.01861 [astro-ph.HE] *Cited on pages 3, 64.*

[40] M. Punturo et al. "The Einstein Telescope: A third-generation gravitational wave observatory". In: *Class. Quant. Grav.* 27 (2010). Ed. by Fulvio Ricci, p. 194002. DOI: 10.1088/0264-9381/27/19/194002 *Cited on pages 3, 73.*

[41] Pau Amaro-Seoane et al. "Laser Interferometer Space Antenna". In: *arXiv: 1702.00786* (Feb. 2017) *Cited on page 3.*

[42] Zaven Arzoumanian et al. "The NANOGrav 12.5 yr Data Set: Search for an Isotropic Stochastic Gravitational-wave Background". In: *Astrophys. J. Lett.* 905.2 (2020), p. L34. DOI: 10.3847/2041-8213/abd401. arXiv: 2009.04496 [astro-ph.HE] *Cited on pages 3, 73.*

[43] Gemma Janssen et al. "Gravitational wave astronomy with the SKA". In: *PoS* AASKA14 (2015). Ed. by Tyler L. Bourke et al., p. 037. DOI: 10.22323/1.215.0037. arXiv: 1501.00127 [astro-ph.IM] *Cited on page 3.*

[44] A. Vilenkin and E.P.S. Shellard. *Cosmic Strings and Other Topological Defects*. Cambridge Monographs on Mathematical Physics. Cambridge University Press, 1994. ISBN: 9780521654760 *Cited on pages 9, 11.*

[45] Rama Basu and Alexander Vilenkin. "Evolution of topological defects during inflation". In: *Phys. Rev. D* 50 (1994), pp. 7150–7153. DOI: 10.1103/PhysRevD.50.7150. arXiv: gr-qc/9402040 *Cited on page 11.*

[46] Andrei D. Linde and Dmitri A. Linde. "Topological defects as seeds for eternal inflation". In: *Phys. Rev. D* 50 (1994), pp. 2456–2468. DOI: 10.1103/PhysRevD.50.2456. arXiv: hep-th/9402115 *Cited on page 11.*

[47] P. Sikivie. "Of Axions, Domain Walls and the Early Universe". In: *Phys. Rev. Lett.* 48 (1982), pp. 1156–1159. DOI: 10.1103/PhysRevLett.48.1156 *Cited on page 11.*

[48] Sidney Coleman and Frank De Luccia. "Gravitational effects on and of vacuum decay". In: *Physical Review D* 21.12 (1980), p. 3305 *Cited on pages 11, 12, 21.*

[49] Steven K. Blau, E. I. Guendelman, and Alan H. Guth. "Dynamics of false-vacuum bubbles". In: *Phys. Rev. D* 35 (6 Mar. 1987), pp. 1747–1766. DOI: 10.1103/PhysRevD.35.1747 *Cited on page 16.*

[50] S. M. Christensen and S. A. Fulling. "Trace Anomalies and the Hawking Effect". In: *Phys. Rev.* D15 (1977), pp. 2088–2104. DOI: 10.1103/PhysRevD.15.2088 *Cited on pages 31, 32.*

[51] Nicholas David Birrell, Nicholas David Birrell, and Paul CW Davies. "Quantum fields in curved space". In: (1984) *Cited on page 31.*

[52] Bryce S. DeWitt. "Quantum Field Theory in Curved Space-Time". In: *Phys. Rept.* 19 (1975), pp. 295–357. DOI: 10.1016/0370-1573(75)90051-4 *Cited on page 31.*

[53] T. S. Bunch and P. C. W. Davies. "Quantum Field Theory in de Sitter Space: Renormalization by Point Splitting". In: *Proc. Roy. Soc. Lond. A* 360 (1978), pp. 117–134. DOI: 10.1098/rspa.1978.0060 *Cited on page 35.*

[54] Stephen Hawking. "Gravitationally collapsed objects of very low mass". In: 152 (Jan. 1971), p. 75. DOI: 10.1093/mnras/152.1.75 *Cited on page 53.*

[55] Bernard J Carr and Stephen W Hawking. "Black holes in the early Universe". In: *Monthly Notices of the Royal Astronomical Society* 168.2 (1974), pp. 399–415 *Cited on page 53.*

[56] Kunihito Ioka et al. "Black hole binary formation in the expanding universe: Three body problem approximation". In: *Physical Review D* 58.6 (1998), p. 063003 *Cited on page 54.*

[57] Takashi Nakamura et al. "Gravitational waves from coalescing black hole MACHO binaries". In: *Astrophys. J. Lett.* 487 (1997), pp. L139–L142. DOI: 10.1086/310886. arXiv: astro-ph/9708060 *Cited on pages 54, 55.*

[58] Jaume Garriga and Nikolaos Triantafyllou. "Enhanced cosmological perturbations and the merger rate of PBH binaries". In: *JCAP* 09 (2019), p. 043. DOI: 10.1088/1475-7516/2019/09/043. arXiv: 1907.01455 [astro-ph.CO] *Cited on pages 56, 64.*

[59] P. C. Peters. "Gravitational Radiation and the Motion of Two Point Masses". In: *Phys. Rev.* 136 (1964), B1224–B1232. DOI: 10.1103/PhysRev.136.B1224 *Cited on page 56.*

[60] Heling Deng. "Gravitational wave background from mergers of large primordial black holes". In: *arXiv: 2110.02460* (Oct. 2021) *Cited on page 58.*

[61] P. Ajith et al. "A Template bank for gravitational waveforms from coalescing binary black holes. I. Non-spinning binaries". In: *Phys. Rev. D* 77 (2008). [Erratum: Phys.Rev.D 79, 129901 (2009)], p. 104017. DOI: 10.1103/PhysRevD.77.104017. arXiv: 0710.2335 [gr-qc] *Cited on pages 60, 61.*

[62] P. Ajith et al. "Inspiral-merger-ringdown waveforms for black-hole binaries with non-precessing spins". In: *Phys. Rev. Lett.* 106 (2011), p. 241101. DOI: 10.1103/PhysRevLett.106.241101. arXiv: 0909.2867 [gr-qc] *Cited on page 60.*

[63] Mehrdad Mirbabayi, Andrei Gruzinov, and Jorge Noreña. "Spin of primordial black holes". In: *J. Cosmol. Astropart. Phys.* 3 (2020), pp. 017, 16. DOI: 10.1088/1475-7516/2020/03/017 *Cited on page 61.*

[64] V. De Luca et al. "The initial spin probability distribution of primordial black holes". In: *J. Cosmol. Astropart. Phys.* 5 (2019), pp. 018, 32. DOI: 10.1088/1475-7516/2019/05/018 *Cited on page 61.*

[65] V. De Luca et al. "The evolution of primordial black holes and their final observable spins". In: *J. Cosmol. Astropart. Phys.* 4 (2020), pp. 052, 33. DOI: 10.1088/1475-7516/2020/04/052 *Cited on page 61.*

[66] Xing-Jiang Zhu et al. "Stochastic Gravitational Wave Background from Coalescing Binary Black Holes". In: *Astrophysical Journal* 739 (Apr. 2011). DOI: 10.1088/0004-637X/739/2/86 *Cited on page 61.*

[67] Sai Wang, Takahiro Terada, and Kazunori Kohri. "Prospective constraints on the primordial black hole abundance from the stochastic gravitational-wave backgrounds produced by coalescing events and curvature perturbations". In: *Phys. Rev. D* 99.10 (2019), pp. 103531, 11. ISSN: 2470-0010. DOI: 10.1103/physrevd.99.103531 *Cited on page 61.*

[68] Yacine Ali-Haimoud. "Correlation Function of High-Threshold Regions and Application to the Initial Small-Scale Clustering of Primordial Black Holes". In: *Phys. Rev. Lett.* 121.8 (2018), p. 081304. DOI: 10.1103/PhysRevLett.121.081304. arXiv: 1805.05912 [astro-ph.CO] *Cited on page 64.*

[69] Vincent Desjacques and Antonio Riotto. "Spatial clustering of primordial black holes". In: *Phys. Rev. D* 98.12 (2018), p. 123533. DOI: 10.1103/PhysRevD.98.123533. arXiv: 1806.10414 [astro-ph.CO] *Cited on page 64.*

[70] Guillermo Ballesteros, Pasquale D. Serpico, and Marco Taoso. "On the merger rate of primordial black holes: effects of nearest neighbours distribution and clustering". In: *JCAP* 10 (2018), p. 043. DOI: 10.1088/1475-7516/2018/10/043. arXiv: 1807.02084 [astro-ph.CO] *Cited on pages 64, 65.*

[71] L. G. Jensen and A. S. Szalay. "N-Point Correlations for Biased Galaxy Formation". In: *ApJL* 305 (June 1986), p. L5. DOI: 10.1086/184673 *Cited on page 65.*

[72] Eanna E. Flanagan. "The Sensitivity of the laser interferometer gravitational wave observatory (LIGO) to a stochastic background, and its dependence on the detector orientations". In: *Phys. Rev. D* 48 (1993), pp. 2389–2407. DOI: 10.1103/PhysRevD.48.2389. arXiv: astro-ph/9305029 *Cited on page 69.*

[73] Joseph D. Romano and Neil J. Cornish. "Detection methods for stochastic gravitational-wave backgrounds: a unified treatment". In: *Living Rev. Rel.* 20.1 (2017), p. 2. DOI: 10.1007/s41114-017-0004-1. arXiv: 1608.06889 [gr-qc] *Cited on page 69.*

[74] URL: https://dcc.ligo.org/LIGO-T1500293/public *Cited on page 69.*

[75] R. Abbott et al. "Upper limits on the isotropic gravitational-wave background from Advanced LIGO and Advanced Virgo's third observing run". In: *Phys. Rev. D* 104.2 (2021), p. 022004. DOI: 10.1103/PhysRevD.104.022004. arXiv: 2101.12130 [gr-qc] *Cited on page 69.*

[76] C. J. Moore, R. H. Cole, and C. P. L. Berry. "Gravitational-wave sensitivity curves". In: *Class. Quant. Grav.* 32.1 (2015), p. 015014. DOI: 10.1088/0264-9381/32/1/015014. arXiv: 1408.0740 [gr-qc] *Cited on page 69.*

[77] Tristan L. Smith and Robert Caldwell. "LISA for Cosmologists: Calculating the Signal-to-Noise Ratio for Stochastic and Deterministic Sources". In: *Phys. Rev. D* 100.10 (2019), p. 104055. DOI: 10.1103/PhysRevD.100.104055. arXiv: 1908.00546 [astro-ph.CO] *Cited on page 69.*

[78] Christopher J. Moore, Davide Gerosa, and Antoine Klein. "Are stellar-mass black-hole binaries too quiet for LISA?" In: *Mon. Not. Roy. Astron. Soc.* 488.1 (2019), pp. L94–L98. DOI: 10.1093/mnrasl/slz104. arXiv: 1905.11998 [astro-ph.HE] *Cited on page 69.*

[79] Nikolaos Karnesis et al. "Characterization of the stochastic signal originating from compact binary populations as measured by LISA". In: *Phys. Rev. D* 104.4 (2021), p. 043019. DOI: 10.1103/PhysRevD.104.043019. arXiv: 2103.14598 [astro-ph.IM] *Cited on page 69.*

[80] Piero Madau and Mark Dickinson. "Cosmic Star Formation History". In: *Ann. Rev. Astron. Astrophys.* 52 (2014), pp. 415–486. DOI: 10.1146/annurev-astro-081811-125615. arXiv: 1403.0007 [astro-ph.CO] *Cited on page 70.*

[81] Eric Thrane and Joseph D. Romano. "Sensitivity curves for searches for gravitational-wave backgrounds". In: *Phys. Rev. D* 88.12 (2013), p. 124032. DOI: 10.1103/PhysRevD.88.124032. arXiv: 1310.5300 [astro-ph.IM] *Cited on page 71.*

[82] Kai Schmitz. "New Sensitivity Curves for Gravitational-Wave Signals from Cosmological Phase Transitions". In: *JHEP* 01 (2021), p. 097. DOI: 10.1007/JHEP01(2021)097. arXiv: 2002.04615 [hep-ph] *Cited on page 71.*

[83] N. Aghanim et al. "Planck 2018 results. VI. Cosmological parameters". In: *Astron. Astrophys.* 641 (2020). [Erratum: Astron.Astrophys. 652, C4 (2021)], A6. DOI: 10.1051/0004-6361/201833910. arXiv: 1807.06209 [astro-ph.CO] *Cited on page 71.*

[84] Zu-Cheng Chen, Fan Huang, and Qing-Guo Huang. "Stochastic Gravitational-wave Background from Binary Black Holes and Binary Neutron Stars and Implications for LISA". In: *Astrophys. J.* 871.1 (2019), p. 97. DOI: 10.3847/1538-4357/aaf581. arXiv: 1809.10360 [gr-qc] *Cited on page 73.*

[85] Yi-Fan Wang et al. "Searching for primordial black holes with stochastic gravitational-wave background in the space-based detector frequency band". In: *Phys. Rev. D* 101.6 (2020), p. 063019. DOI: 10.1103/PhysRevD.101.063019. arXiv: 1910.07397 [astro-ph.CO] *Cited on page 73.*

[86] Zu-Cheng Chen, Chen Yuan, and Qing-Guo Huang. "Confronting the primordial black hole scenario with the gravitational-wave events detected by LIGO-Virgo". In: *arXiv: 2108.11740* (Aug. 2021) *Cited on page 73.*

[87] S. Kawamura et al. "The Japanese space gravitational wave antenna DECIGO". In: *Class. Quant. Grav.* 23 (2006). Ed. by N. Mio, S125–S132. DOI: 10.1088/0264-9381/23/8/S17 *Cited on page 73.*

[88] Jun Luo et al. "TianQin: a space-borne gravitational wave detector". In: *Class. Quant. Grav.* 33.3 (2016), p. 035010. DOI: 10.1088/0264-9381/33/3/035010. arXiv: 1512.02076 [astro-ph.IM] *Cited on page 73.*

[89] H. Middleton et al. "Massive black hole binary systems and the NANOGrav 12.5 yr results". In: *Mon. Not. Roy. Astron. Soc.* 502.1 (2021), pp. L99–L103. DOI: 10.1093/mnrasl/slab008. arXiv: 2011.01246 [astro-ph.HE] *Cited on page 73.*

[90] Michele Maggiore et al. "Science Case for the Einstein Telescope". In: *JCAP* 03 (2020), p. 050. DOI: 10.1088/1475-7516/2020/03/050. arXiv: 1912.02622 [astro-ph.CO] *Cited on page 74.*

[91] Georges Darmois. *Les équations de la gravitation einsteinienne*. Gauthier-Villars, 1927 *Cited on page 79.*

[92] W. Israel. "Singular hypersurfaces and thin shells in general relativity". In: *Nuovo Cim.* B44S10 (1966). [Nuovo Cim.B44,1(1966)], p. 1. DOI: 10.1007/BF02710419, 10.1007/BF02712210 *Cited on page 79.*